Application and development of semiempirical quantum chemical methods for the investigation of the dynamics of electronically excited states

Inaugural-Dissertation

zur Erlangung des Doktorgrades der

Mathematisch-Naturwissenschaftlichen Fakultät der

Heinrich-Heine-Universität Düsseldorf

vorgelegt von Lasse Spörkel

aus Henstedt-Ulzburg

Mülheim an der Ruhr, Oktober 2016

Ich versichere an Eides Statt, dass die Dissertation von mir selbständig und ohne unzulässige fremde Hilfe unter Beachtung der „Grundsätze zur Sicherung guter wissenschaftlicher Praxis an der Heinrich-Heine Universität Düsseldorf" erstellt worden ist. Die Dissertation wurde in der vorgelegten oder in ähnlicher Form noch bei keiner Institution eingereicht. Ich habe keine erfolglosen Promotionsversuche unternommen.

Mülheim an der Ruhr, den 16. Januar 2017

(Lasse Spörkel)

Abstract

In this work I present excited state molecular dynamics (MD) calculations and improvements to the existing simulation procedures. The method employed is trajectory surface hopping (TSH) in conjunction with the semiempirical OM2/MRCI Hamiltonian. It has been applied to three molecules of recent scientific interest.

In TSH simulations a set of samples is generated in the ground state. For each sample an excited state MD simulation is run with the possibility to hop between electronic states during the relaxation to the ground state. The statistical analysis of all trajectories gives insight into competing deactivation processes, deactivation times, quantum yields, and product distributions. Such simulations require many trajectories that run independently of each other (typically several hundred) with many single-point energy and gradient evaluations per trajectory (typically several thousand). This vast number of calculations renders high-level *ab initio* methods impractical for medium-sized organic molecules. Therefore, we employed the semiempirical OM2/MRCI method which delivers realistic energies and structures for ground and excited states at greatly reduced computational costs.

We first investigated salicylideneaniline, which is a typical representative of aromatic Schiff bases that exhibit photochromic behavior. Our TSH simulations shed light on the competing deactivation channels, the time scale of the processes involved, and the product responsible for photochromism. In a second study we addressed non-equilibrium isotope effects on ultrafast excited state intramolecular proton transfer (ESIPT) by performing TSH simulations for 7-(2-pyridyl)indole and its deuterated isotopologue. We were able to reproduce the experimental results on isotope shifts and show that the ESIPT is an essentially barrierless process.
In a third application we investigated the full photocycle of salicylidene methylamine, a possible photoswitching agent. We ran two sets of excited state dynamics simulations starting from the two relevant conformers. We characterized the main channels for photoswitching and quantified the efficiency of the targeted pathways. Additionally, we identified a photoinactive isomer that breaks the photocycle.
In the course of this work I encountered problems in the existing methods and procedures arising from changes in the active configuration interaction space during the simulations. These problems were addressed and largely overcome in our latest publication, in which we introduced an adaptive time step in the dynamics code, in order to improve the precision and stability of the simulations in numerically difficult areas of configuration space.

This thesis showed the significance and usefulness of TSH simulations despite their simple underlying model. It clarified the photocycles of three molecules of current scientific interest and enabled us to suggest a molecule for the application as a photoswitch. The use of adaptive time steps will help to improve TSH simulations in combination with incomplete active space configuration interaction methods.

Zusammenfassung

In der vorliegenden Arbeit stelle ich sowohl Molekulardynamik(MD)-Rechnungen an angeregten Zuständen als auch Verbesserungen an den existierenden Algorithmen und Programmen vor. Als Methode wird Trajectory Surface Hopping (TSH) in Kombination mit dem semiempirischen OM2/-MRCI-Verfahren verwendet. Im Anwendungsteil wurden drei Moleküle von aktuellem wissenschaftlichem Interesse untersucht.

Für die TSH-Simulationen wird zunächst ein Satz von Startkonfigurationen generiert. Für jede Konfiguration wird eine MD-Simulation im angeregten Zustand gestartet mit der impliziten Möglichkeit, zwischen den Zuständen zu springen, um schlussendlich zum Grundzustand zurückzugelangen. Anhand der statistischen Auswertung aller Trajektorien lassen sich Schlüsse über konkurrierende Deaktivierungswege, Deaktivierungszeitskalen, Quantenausbeuten und Produktverteilungen ziehen. Für diese Art von Rechnungen ist es nötig, viele unabhängige Trajektorien (im Bereich mehrerer Hundert) mit vielen einzelnen Energie- und Gradientberechnungen pro Trajektorie (im Bereich mehrerer Tausend) zu simulieren. Durch diese enorme Anzahl an Berechnungen ist die Verwendung von hochgenauen *ab-initio*-Methoden nicht praktikabel für mittelgroße organische Moleküle. Aus diesem Grund nutzen wir die OM2/MRCI-Methode, welche realistische Energien und Strukturen für Grund- und angeregte Zustände liefert, aber nur einen Bruchteil an Rechenleistung benötigt.

Das erste der untersuchten Moleküle ist Salicylidenanilin, ein typischer Repräsentant von aromatischen Schiffbasen mit photochromischen Eigenschaften. Mit unserer Studie konnten wir Aufschluss über die konkurrierenden Deaktivierungswege, die Zeitskalen der involvierten Prozesse und das für den Photochromismus verantwortliche Konformer geben.

Im zweiten Beispiel haben wir uns mit Isotopeneffekten auf den ultraschnellen intramolekularen Protonentransfer im angeregten Zustand befasst, unter Verwendung von TSH-Simulationen an 7-(2-Pyridyl)indol und dessen deuteriertem Isotopologen. Wir konnten die experimentellen Ergebnisse gut reproduzieren und zeigen, dass der Protonentransfer in diesem Fall nahezu barrierelos stattfindet.

Das dritte Beispiel beschäftigt sich mit dem kompletten Photokreislauf von Salicylidenmethylamin, einem möglichen Kandidaten als Photoschalter. Wir haben zwei Sätze von TSH-Trajektorien simuliert, mit den beiden wichtigsten Konformeren als Startpunkt. Wir konnten die Hauptwege zur Photoschaltung charakterisieren und die Effizienz der jeweiligen Pfade quantifizieren. Außerdem haben wir ein photoinaktives Konformer gefunden, welches den Photokreislauf unterbricht.

Im Laufe dieser Arbeit konnte ich Probleme in den existierenden Methoden und Vorgehensweisen identifizieren. Mit diesen habe ich mich in unserer letzten Publikation befasst, in der ein adaptiver Zeitschritt in die Dynamikrechnungen eingeführt wurde, um die Präzision und Stabilität in numerisch anspruchsvollen Regionen zu verbessern.

Meine Dissertation zeigt, dass TSH-Simulationen trotz des zugrunde liegenden einfachen Modells signifikante und nützliche Ergebnisse produzieren können. Mit ihrer Hilfe konnten die Photokreisläufe von drei Molekülen von aktuellem wissenschaftlichem Interesse aufgeklärt und ein Kandidat als möglicher Photoschalter vorgeschlagen werden. Der Einsatz von adaptiven Zeitschritten wird dabei helfen, TSH-Simulationen unter Verwendung von MRCI-Rechnungen mit unvollständigen aktiven Räumen zu verbessern.

Acknowledgements

This doctoral thesis is a publication-based thesis. The work presented in this thesis has been published in international peer-reviewed scientific journals. A short summary of the published papers as well as a description of my contribution to each piece of work is given. The four published papers are included as attachments to this thesis.

Tell your son to stop trying to fill your head with science - for to fill your heart with love is enough!

Richard P. Feynman

List of publications

1   Photodynamics of Schiff Base Salicylideneaniline: Trajectory Surface-Hopping Simulations

Lasse Spörkel, Ganglong Cui and Walter Thiel

The Journal of Physical Chemistry A, **2013**, 117, 4574–4483.

2   Nonequilibrium H/D Isotope Effects from Trajectory-Based Nonadiabatic Dynamics

Lasse Spörkel, Ganglong Cui, Axel Koslowski and Walter Thiel

The Journal of Physical Chemistry A, **2014**, 118, 152–157.

3   Photoswitching of Salicylidene Methylamine: A Theoretical Photodynamics Study

Lasse Spörkel, Joanna Jankowska and Walter Thiel

The Journal of Physical Chemistry B, **2015**, 119, 2702–2710.

4   Adaptive Time Steps in Trajectory Surface Hopping Simulations

Lasse Spörkel and Walter Thiel

The Journal of Chemical Physics, **2016**, 144, 194108.

Other publications not submitted as part of this thesis

5 Semiempirical Quantum-Chemical Orthogonalization-Corrected Methods: Theory, Implementation, and Parameters

Pavlo O. Dral, Xin Wu, **Lasse Spörkel**, Axel Koslowski, Wolfgang Weber, Rainer Steiger, Mirjam Scholten and Walter Thiel

Journal of Chemical Theory and Computation, **2016**, 12, 1082–1096.

6 Semiempirical Quantum-Chemical Orthogonalization-Corrected Methods: Benchmarks for Ground-State Properties

Pavlo O. Dral, Xin Wu, **Lasse Spörkel**, Axel Koslowski and Walter Thiel

Journal of Chemical Theory and Computation, **2016**, 12, 1097–1120.

Contents

1. Introduction

The interaction between photons and molecules can lead to various photoinduced processes. A molecule can absorb the energy of a photon and excite an electron to a higher energy level. Starting from this electronically excited state there are several possible deactivation mechanisms. To minimize the energy while staying in the same electronic state, the molecule can relax vibrationally by collisions with nearby molecules to the lowest vibrational level.

The transition to other electronic states can occur either radiatively or in a radiationless manner. If a photon is emitted and the multiplicity stays the same, the process is called *fluorescence*. A direct change of states without emission can occur through so-called conical intersections between states of the same multiplicity, by a process named *internal conversion.*

A radiationless transition to a state of different multiplicity is called *intersystem crossing*. After this process a photon can be emitted. The corresponding radiative decay between states of different multiplicity is called *phosphorescence* and occurs on longer timescales.

The previously mentioned conical intersections are of crucial importance for excited state deactivation processes.[1] While it was assumed in the past that these are rare phenomena, it is now known that they are ubiquitous and important for many excited state deactivation processes.[2–9] A conical intersection marks a point of energetic degeneracy of two or more potential energy surfaces. In the vicinity of these points the Born-Oppenheimer approximation breaks down and the nonadiabatic coupling between the involved states diverges to infinity.

The shape of a conical intersection is defined by two nuclear-displacement vectors that lift the degeneracy and are called branching-space vectors. The vector **g** points in the direction of maximum difference between the energy gradients of the two states, while the vector **h** points in the direction of maximum coupling between the states. Figure 1.1 shows an idealized picture of the two-dimensional branching space of a conical intersection. The remaining $3N - 8$ degrees of freedom do not lift the degeneracy and form the so-called intersection seam.

Many recent fields of research involve deactivation processes of excited states. A few examples are biological markers, molecular switches, optical storage materials or solar cells. In
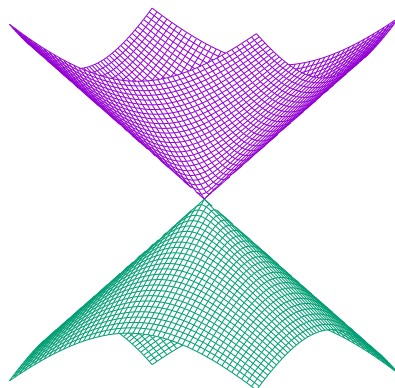
Figure 1.1.: Structural representation of the two-dimensional branching space of a conical intersection

order to describe these processes, it is necessary to investigate the dynamics of the system. Different techniques exist that vary in accuracy and computational cost and range from coarse methods like Monte Carlo approaches to very accurate methods like full-dimensional quantum dynamics.

It is generally quite difficult to properly describe the electronic structure of electronically excited states. While ground-state calculations can almost be considered routine, the setup and interpretation of excited-state calculations involves much expertise and individual involvement of the researcher.

There exist high-level quantum-chemical methods that give a fairly accurate description of excited states in small to medium sized molecules. Widely used are the complete-active-space self-consistent field (CASSCF)[10] method combined with complete-active-space second-order perturbation theory (CASPT2),[11–13] time-dependent density functional theory (TD-DFT)[14, 15] and a hybrid approach of DFT and multi-reference configuration interaction (DFT/MRCI).[16–18] It is also possible to compute excited states by coupled cluster methods. This is mostly done either via equation of motion (EOM)[19] or via a linear response (LR) ansatz, and there is a hierarchy of methods with increasing accuracy and computational effort (CCS, CC2, CCSD, CC3 etc.)[20–24] Our group published benchmarks of the TD-DFT and DFT/MRCI methods[25] and of the CASPT2 and LR-CC methods.[26] However, when the systems of interest become larger, or dynamic properties are investigated, these high-level methods are usually computationally too demanding and thus not applicable. It is noteworthy to mention that some recent works could successfully apply *ab initio* methods to systems of the size of vitamin D.[27–29]

One way to reduce the computational cost could be to focus on only a few degrees of

freedom, but important features might get overlooked in such model systems using high-level calculations. A great reduction in computation time can be achieved by using semiempirical quantum-chemical methods. Many defects caused by the underlying approximations can be compensated by thorough and careful parametrization. The combination with configuration interaction[30,31] allows the semiempirical calculation of electronically excited states. In such treatments static correlation is included by use of multi-reference configuration interaction (MR-CI), while dynamic correlation effects are approximately taken into account through the parametrization.

Many different semiempirical methods exist that differ strongly in terms of accuracy, designated field of usage, and diversity of applications. Prominent examples are the AM1[32] and PM3[33,34] methods that are both based on the modified neglect of diatomic overlap (MNDO) approximation.[35,36] The formalism has been later expanded to an *spd* basis, which is used in the PM6[37] and PM7[38] methods that can handle elements from the whole periodic table. In order to improve the basic approximations in MNDO-type methods, orthogonalization corrections were introduced in the OMx methods.[39–43] The available OM1, OM2 and OM3 variants differ in the extent of these corrections. The OMx corrections provide an explicit representation of Pauli exchange repulsion that leads to a much better description of ground and excited state properties. This was documented in recent comprehensive benchmarks for ground[44] and excited states,[45] which often gave accuracies close to standard TD-DFT results. Up to now, OMx parameters are available only for the elements H, C, N, O and F, described by an *sp* basis. Work is in progress to extend the code to an *spd* basis and to parametrize further elements.

Although semiempirical methods are usually parametrized for a wide range of molecules and properties, it can not be guaranteed that they will work for the system under investigation. Therefore, in any intended application, one needs to perform a careful specific validation, by comparing the results from semiempirical test calculations with those from high-level accurate quantum-chemical methods or with experimental findings.

When dynamic properties of photochemical processes are to be examined, the mixed quantum-classical trajectory surface hopping (TSH) method offers a good compromise between simplicity and accuracy.[46,47] TSH simulations require a set of trajectories, each of which is propagated along a single adiabatic surface at each time step. Hops between the different states are allowed via statistical probabilities, such that the quantum amplitudes of the full propagation of the time-dependent Schrödinger equation are reproduced. The hopping probabilities are calculated using the fewest switches (FS) algorithm that tries to reduce the number of hops to a minimum while maintaining populations that correspond to the ones predicted by the Schrödinger equation.[46,48]

A single trajectory only represents one particular path on the potential energy surface and the hopping between different surfaces is a statistical process. In order to sample the complete potential energy space and maintain the distribution of hopping events, it is important to calculate many trajectories. A set of initial configurations has to be generated at the beginning, which is commonly done by two ways: either the configurations are picked from a ground-state MD run or they are sampled from the ground-state normal modes, which is called Wigner sampling.[47, 49, 50]

A severe drawback of the TSH method is overcoherence, which is caused by the fact that the electronic wavefunction is only propagated along one particular nuclear trajectory without the possibility to decohere along multiple electronic surfaces.[51] There are some approximate methods to correct for this defect, for example the one-parameter correction scheme from Granucci et al.[52] and the parameterless correction from Shenvi et al.[53, 54] Despite its simplicity and the overcoherence issue, the TSH method was successfully applied in our group to many systems, which greatly improved the understanding of the underlying photoinduced processes.[55–70]

When the OM2/MRCI method is used in TSH simulations, a set of active orbitals needs to be selected beforehand. A typical strategy is to select a fixed number of frontier orbitals, that is the x highest occupied molecular orbitals (HOMOs) and y lowest unoccupied molecular orbitals (LUMOs). This procedure should guarantee that the most important orbitals are in the active space, because orbitals that are far away from the HOMO-LUMO gap tend to contribute less to the CI treatment of low-lying excited states. However, in certain applications it may be more appropriate to select the active orbitals by their character,[71] for example by including all π-orbitals and the highest occupied n-orbital in the calculation of states with $\pi\pi^*$ and $n\pi^*$ character.

Since the geometries will change along a dynamics trajectory, it is very likely that the ordering and relative energies of orbitals will also change. In these cases one needs to decide whether the orbitals should be tracked along the trajectory or whether the active space selection should be applied in each step.[71, 72] In the latter case, the active space might change between two steps, which will cause sudden potential energy jumps and inconsistencies along the trajectory. Hence we recommend to track the orbitals. This tracking may become ambiguous in some situations when the character of orbitals changes strongly. One may then arrive at configurations where the character of orbitals does not correspond any longer to the initially selected ones. In such cases it is helpful to reduce the time step between two simulation steps to very small values, in order to have much smaller changes in the molecular orbitals and hence a more reliable tracking along the trajectory.

The use of finite active spaces in CI methods also becomes problematic when neighboring

active and inactive orbitals come very close to each other in energy and start mixing.[71] The chance of this happening is higher when the active space is sparse, that is when active and inactive orbitals alternate in the ordering. This mixing between active and inactive orbitals causes local spikes in the potential energy surface, which in turn have a strong impact on gradients and force constants; a detailed analysis has been reported in a recent benchmark study.[45] When such problems occur in a TSH simulation, the artificial overestimation of the gradients will cause an overestimation of the velocities after integration and thus of the kinetic energy of the system. This leads to a non-constant total energy and breaks NVE dynamics simulations. The problem becomes more serious with increasing time step for integration of the equations of motion.

To cope with these issues, we propose an adaptive time step that can iteratively be decreased when either the tracking of MOs becomes uncertain or when the total energy shows a non-negligible change from a constant value. Our implementation of the adaptive algorithm uses a reduced time step only in critical regions and adopts the larger default time step again after passing through this region. Therefore, simulations can be run essentially as long as before, but avoid failures without losing precision or efficiency.

Apart from these methodological developments, I mainly focused on the TSH applications to aromatic Schiff bases[73] and related systems that can undergo an excited state intramolecular proton transfer (ESIPT) upon photoexcitation.[74–77] These systems have been studied extensively in the past decades, and they are among the most popular photochromic compounds. The ESIPT process has some unique characteristics, which makes it interesting for applications in photoswitches, molecular memory materials or optical data processing.[78–85] After photoexcitation a proton gets transferred from the nitrogen atom of the Schiff base to neighboring acceptor sites like nitrogen or oxygen, with a very small or non-existent barrier. This rearrangement enables photochemical isomerizations that are usually not feasible in the original molecule. The system can end up in stable ground-state isomers that have a strong shift in their spectra compared to the global minimum structure (photochromism). A molecule can be used as a photoswitch, if it has at least two stable photochromic ground-state forms that have non-overlapping absorption spectra in the relevant excitation regions and that can be accessed via radiationless decay paths from the excited state.

Because of the many competing deactivation pathways in these systems, it is desirable to derive a complete mechanistic scenario from full-dimensional dynamics simulations. Purely static calculations or quantum dynamics with only a few degrees of freedom may give valuable insights, but will generally not provide a complete picture of all processes.

2. Theoretical Background

2.1. Methodology

This chapter outlines the basic theory behind the applied methods. It should provide a short overview of quantum chemistry and especially of semiempirical methods, rather than a thorough derivation. For more details, the reader is advised to refer to the original publications or to general quantum chemistry textbooks.[86–88]

The aim of most theoretical and computational chemistry methods is to solve the time-independent Schrödinger equation as exactly as possible.

$$\mathscr{H}\Psi = E\Psi \tag{2.1}$$

(with $\mathscr{H}$: Hamilton operator; Ψ: wavefunction of the system; E: associated eigenvalues).

This equation is analytically solvable only for model or one-electron systems (e.g. particle in a box, H atom, He$^+$ atom, Li^{2+} atom etc.), which calls for approximations. The most basic approximation is the separation of the movement of the nuclei and the electrons, which can be justified by the fact that electrons are much lighter and faster than nuclei. They can adapt practically instantaneously to changes of the nuclear framework. This decoupling is called Born-Oppenheimer approximation.[89] The electronic wavefunction can thus be determined for fixed positions of the nuclei.

The second basic approximation is to represent the N-electron wavefunction as a Slater determinant of one-electron functions (orbitals) to ensure the anti-symmetry of the fermionic wavefunction and the Pauli exclusion principle. The variationally best orbitals are then obtained from the solution of the Hartree-Fock (HF) equations:

$$\mathscr{F}\psi_i = \epsilon_i\psi_i \tag{2.2}$$

(with $\mathscr{F}$: Fock operator; ψ_i: one-electron orbital; ϵ_i: orbital energy).

In order to solve the HF equations it is useful to express the single-electron wavefunctions

in terms of a linear combination of atomic orbitals (LCAO):

$$\psi = \sum_k C_{\mu i} \phi_\mu \qquad (2.3)$$

(with $C_{\mu i}$: LCAO coefficients; ϕ_μ: atomic orbitals).

Equation 2.2 can be rewritten in matrix form, which gives rise to the Roothan-Hall equations:

$$FC = SCE \qquad (2.4)$$

with S being the overlap matrix between the atomic orbitals:

$$S_{\mu\nu} = \int \phi_\mu(r_1)\phi_\nu(r_1)\,dr_1 \qquad (2.5)$$

The equations have to be solved in an iterative manner, through a self-consistent field procedure (SCF).

2.1.1. Semiempirical methods

In order to reduce the computational effort drastically, the semiempirical methods incorporate severe approximations when setting up and solving the Roothaan-Hall equations. Many terms are neglected or simplified, in order to avoid the costly evaluation of most of the multidimensional integrals. The remaining terms are represented by parametric functions and the parameters are optimized such that the semiempirical calculations yield results as close as possible to theoretical or experimental reference data. The quality of a semiempirical method thus depends both on the simplifications in the underlying model and on the chosen parameters. These parameters can be optimized with different goals in mind. They can be tuned so that the results will best meet experimental values for a wide variety of molecules and properties (general-purpose methods) or they can be specifically adapted to one system (special-purpose parametrizations).[90–93]

Almost all semiempirical methods use the so-called core approximation, in which the atomic core is collapsed with all inner shell electrons. Only the valence electrons are treated explicitly in the electronic calculations. Furthermore, they generally employ a minimal valence basis set to reduce the computational cost.

The most advanced semiempirical integral approximations make use of the neglect of diatomic differential overlap (NDDO) model, in which the differential overlap is set to zero between basis orbitals at different atoms. As a consequence, all three-center and four-center

two-electron integrals vanish so that only one-center and two-center integrals have to be calculated. Moreover, the overlap matrix S in equation 2.4 becomes the identity matrix and the secular equation gets simplified to a standard eigenvalue problem.[94]

The modified neglect of diatomic overlap (MNDO) method is based on the NDDO model.[35, 36] It uses Slater-type atomic orbitals. The one-center two-electron integrals are derived from experimental atomic spectra. The two-center two-electron integrals are computed from a point-charge multipole model that shows the correct classical electrostatic limit at large distances and converges to the MNDO one-center integrals at small distances. The two-center core-electron and core-core terms are represented in terms of related two-electron integrals. The two-center one-electron resonance integrals are described by scaled overlap integrals. The core-core terms contain an additional effective atom-pair potential which is repulsive and is designed to incorporate interactions formally neglected in the MNDO scheme, in particular Pauli exchange repulsion. Many of the more recent semiempirical methods (e.g. AM1,[32] PM3,[33, 34] PM6[37] and PM7[38]) are variants and reparametrizations of the MNDO method.

To go beyond the MNDO model, our group has over the years developed three orthogonalization models (OM1, OM2, OM3),[39–42] which include explicit orthogonalization corrections that appear in the transformation of the secular equation from a non-orthogonal basis ($FC = SCE$) to an orthogonal basis ($FC = CE$). These corrections were first incorporated only in the one-center terms in the core Hamiltonian (OM1) and later also in the two-center resonance integrals (OM2, OM3); OM3 differs from OM2 only in neglecting some smaller correction terms that do not influence the results much while notably increasing the computational effort for large molecules. The OMx methods also extend the MNDO model by including penetration terms and effective core potentials for inner-shell electrons, and there are some technical distinctions: the OMx methods use Gaussian basis orbitals, and many of the integral approximations are based on analytic integral evaluations. The OMx methods are fully described and validated in three recent publications.[43–45]

The OMx results are generally superior to those from MNDO-type methods.[44, 95–97] This is true, in particular, for the properties of electronically excited states,[45, 96] which motivates the widespread use of OM2 and OM3 in trajectory surface hopping simulations of photoinduced processes.

2.1.2. Excited states

The calculation of excited states is not a trivial task and can be done with different methods that all have their own strengths and weaknesses. At geometries where different states

become close in energy, the Born-Oppenheimer approximation[89] breaks down and internal conversion can occur. It is thus necessary to use a method that gives a balanced description of all relevant states and the interplay between them.

While a single Slater determinant is used to represent the ground-state wavefunction in HF theory, a more general ansatz involves linear combinations of Slater determinants or, preferably, of spin-adapted configuration state functions (CSFs). This leads to a method called configuration interaction (CI) which accounts for electron correlation and is suitable for excited state calculations.

In the CI method the wavefunction is a linear combination of CSFs:

$$\Psi = \sum_k c_k \psi_k \tag{2.6}$$

The coefficients c_k are determined variationally until the energy is minimized.

A CI with all possible CSFs that can be constructed by excitations from the HF determinant (full CI) is normally not feasible for the molecules of interest, because the computational effort grows exponentially with system size. The number of CSFs needs to be strongly reduced in order to make the CI calculation practical. To achieve this goal, one usually selects a set of molecular orbitals as active orbitals, and excitations are only allowed from active occupied orbitals into active unoccupied orbitals.

The number of CSFs can be further reduced by limiting the types of allowed excitations from the reference configurations. The latter are chosen such that they provide a realistic zero-order description of the molecule at all relevant geometries. Typically several reference configurations are required for a balanced description, especially around conical intersections. We usually only allow single and double excitations from the reference configurations, because higher excitations do not interact directly with the reference configurations and will thus normally not contribute much to the wavefunction. The resulting treatment is called multi-reference configuration interaction with single and double excitations (MRCISD).

Our code provides a general implementation of the MRCI method using the graphical unitary group approach (GUGA).[30, 31, 98] The combination of the semiempirical OMx methods with GUGA-MRCI gives an extremely fast, yet precise and versatile tool that can be applied to many ground and excited state problems.

A popular *ab initio* method based on the active space ansatz is the complete-active-space self-consistent field (CASSCF) method, which involves a full CI calculation in the active space with simultaneous optimization of the SCF and CI coefficients (whereas in standard CI approaches the SCF coefficients are not varied in the CI procedure). Generally the simultane-

ous optimization of SCF and CI coefficients is called multi-configurational SCF (MCSCF). The CASSCF approach recovers only a fraction of the dynamic correlation because of active-space limitations. This can be remedied for example by a second-order perturbation correction to the CASSCF treatment. Widely used is the complete-active-space second-order perturbation theory (CASPT2).

Linear response methods offer a different approach for the calculation of excited states. The most popular application is the combination with DFT, which gives rise to the time-dependent density functional theory (TD-DFT). A great advantage is their black-box character: TD-DFT calculations can be easily set up and many states can be calculated simultaneously. However, like other single-reference methods, TD-DFT breaks down in the vicinity of conical intersections between the ground and excited states.

2.2. Nonadiabatic dynamics

When a system approaches regions with significant nonadiabatic couplings between different states, the Born-Oppenheimer approximation[89] loses its validity. In such situations it is not sufficient to treat each state separately, but one needs to use a method that allows an initial wavepacket to evolve into different states.

The semiclassical trajectory surface hopping (TSH) method[46, 48] offers an efficient yet realistic approach to describe the dynamics in such cases. A TSH simulation employs a set of independent trajectories, each of which starts at a randomly sampled initial configuration (with regard to geometry and velocities). For this purpose, we generate a canonical NVT ensemble of configurations by a ground-state MD run with the Nosé-Hoover chains thermostat.[99–101] We select the desired number of initial geometries and velocities at random points of this MD run that should be sufficiently long (typically tens of picoseconds). The starting configurations are then filtered according to a selection criterion (see equation 2.7).[50, 102] The criterion depends on the oscillator strength as well as on the vertical excitation energy. This procedure ensures that only trajectories are started that are likely to be excited.

$$P = \frac{f/\Delta E^2}{\max(f/\Delta E^2)} \tag{2.7}$$

(with P: selection probability; f: oscillator strength; ΔE: vertical excitation energy)

More details about nonadiabatic dynamics can be found in the literature.[28, 47, 103–109]

Nonadiabatic dynamics are not limited to TSH methods. More advanced are full quantum dynamics approaches, for example the time-dependent Hartree (TDH)[110] and multi-

configuration time-dependent Hartree (MCTDH) methods.[111, 112] Another successful approach is *ab initio* multiple spawning (AIMS),[113] which extends the TSH ansatz by Gaussian wavepackets that can disperse along multiple potential energy surfaces and remove the statistical character of hopping events in TSH simulations.

2.2.1. Trajectory surface hopping

In TSH dynamics each trajectory evolves along a single potential energy surface that belongs to a single electronic state at a given time. The potential energy surfaces are obtained from the solution of the time-independent electronic Schrödinger equation. The motion of the nuclei is described by the classical Newton equations.[47, 72]

A basic approximation of the TSH method is that the trajectories are independent of each other. The method thus has a local character, which avoids the need for precalculated multidimensional energy surfaces. It allows simple implementations, in which all required energies, gradients and nonadiabatic couplings are calculated on-the-fly at each step of the trajectory.

The TSH method employs a hopping mechanism for the switching between different states that is controlled by the quantum population of each state. The average populations obtained from the set of trajectories should approximately resemble the quantum state populations.

In order to get the quantum amplitudes $c_i(t)$ of the states along a trajectory $\vec{R}(t)$, they need to be integrated for each MD step. The derivation starts from the time-dependent Schrödinger equation:

$$i\hbar\frac{\partial\Phi(\vec{r},\vec{R},t)}{\partial t} = H\Phi(\vec{r},\vec{R},t) \tag{2.8}$$

(with $\vec{R}$: nuclear coordinates; $\vec{r}$: electronic coordinates)

The total electronic wavefunction Φ is written as an expansion of adiabatic state wavefunctions ϕ_i:

$$\Phi(\vec{r},\vec{R},t) = \sum_i c_i(t)\phi_i(\vec{r},\vec{R}) \tag{2.9}$$

(with $c_i(t)$: complex-valued expansion coefficients)

The Hamiltonian that describes the motion of the electrons is given by:

$$H(\vec{r},\vec{R}) = -\frac{\hbar^2}{2m_e}\sum_\alpha \nabla^2_{\vec{r}_\alpha} + V_{rR}(\vec{r},\vec{R}) \tag{2.10}$$

(with V_{rR}: Coulomb-type potential energy operator; α: electronic degrees of freedom; m_e:

mass of the electron)

When equations 2.8 to 2.10 are combined, transformed and integrated,[72] one obtains the following equation in the adiabatic basis ($\dot{\vec{R}}$ marks the time derivative of $\vec{R}$):

$$i\hbar\frac{\mathrm{d}c_j(t)}{\mathrm{d}t} = \sum_i c_i(t)[H_{ji} - i\hbar\dot{\vec{R}} \cdot \vec{d}_{ji}] \tag{2.11}$$

where the nonadiabatic couplings $\vec{d}_{ji}$ are defined as:

$$\vec{d}_{ji}(\vec{R}) = \int \phi_j^*(\vec{r}, \vec{R})[\nabla_{\vec{R}}\phi_i(\vec{r}, \vec{R})]\mathrm{d}\vec{r} \tag{2.12}$$

When using adiabatic basis functions, equation 2.11 can be simplified to:

$$i\hbar\frac{\mathrm{d}c_j(t)}{\mathrm{d}t} = c_j(t)\epsilon_j - i\hbar \sum_i c_i(t)\dot{\vec{R}} \cdot \vec{d}_{ji} \tag{2.13}$$

The amplitudes of the quantum states are numerically calculated by integrating equation 2.13 along each MD step.

2.2.2. Fewest switches algorithm

The switching algorithm needs to guarantee that the distribution of states among all trajectories represents the integrated amplitudes from equation 2.13 well. For this purpose the fewest switches algorithm (FSA)[46] was introduced, which tries to reproduce the right statistical distribution with a number of electronic transitions as small as possible.

The number of trajectories N_i in state i and the total number of trajectories N are related by:

$$N_i(t) = \rho_{ii}(t)N \tag{2.14}$$

where the density matrix ρ_{ii} can be seen as a quantum probability:

$$\rho_{ii}(t) = c_i^*(t)c_i(t) \tag{2.15}$$

If the system evolves in time by $\mathrm{d}t$, equation 2.14 changes to:

$$N_i(t + \mathrm{d}t) = \rho_{ii}(t + \mathrm{d}t)N \tag{2.16}$$

To minimize the number of hops, it is sufficient to only consider the net flow of populations. Assuming that $N_i(t) > N_i(t + dt)$, the probability for hopping out of state i at an infinitesimally small time step equals

$$P_i(t)dt = \frac{N_i(t) - N_i(t + dt)}{N_i(t)} = \frac{\rho_{ii}(t) - \rho_{ii}(t + dt)}{\rho_{ii}(t)} \tag{2.17}$$

$$\approx -\frac{\dot{\rho}_{ii}dt}{\rho_{ii}} \tag{2.18}$$

After substitution with equation 2.13 and some rearrangement,[72] the following equation can be derived:

$$P_i(t)dt = 2\frac{\sum_j \text{Re}(c_i^* c_j \vec{R} \cdot \vec{d}_{ij})}{c_i^* c_i}dt \tag{2.19}$$

Switching from a differential time to a finite time provides the probability to hop out of state i in the time interval Δt:

$$P_i = 2\sum_j \frac{\int_t^{t+\Delta t} \text{Re}(c_i^* c_j \vec{R} \cdot \vec{d}_{ij})dt}{c_i^* c_i} \tag{2.20}$$

The chance for hopping from state i to state j is given by just one element from the sum in equation 2.20:

$$P_{ij} = 2\frac{\int_t^{t+\Delta t} \text{Re}(c_i^* c_j \vec{R} \cdot \vec{d}_{ij})dt}{c_i^* c_i} \tag{2.21}$$

In equation 2.18 we only considered the net flow in one direction. Therefore any negative value for the probability needs to be discarded. This leads to the following transition probability:

$$g_{ij} = \max(P_{ij}, 0) \tag{2.22}$$

The decision for an execution of a hop depends on the probability g_{ij} and a randomly drawn number $0 < \xi < 1$. A hop from state i to state k happens if:

$$\sum_j^k g_{ij} < \xi < \sum_j^{k+1} g_{ij} \tag{2.23}$$

3. Summaries of publications

3.1. Photodynamics of Schiff Base Salicylideneaniline: Trajectory Surface-Hopping Simulations

Lasse Spörkel, Ganglong Cui and Walter Thiel

The Journal of Physical Chemistry A, **2013**, 117, 4574–4483.

I carried out all calculations and performed the subsequent analysis. I wrote most parts of the manuscript. I created all included figures.[114]

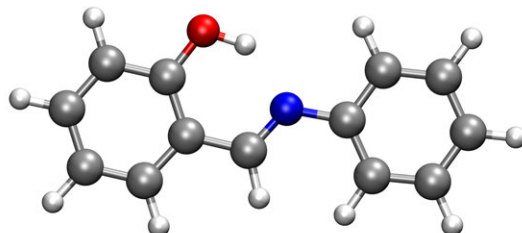In this paper we investigated the photochemical cycle of salicylideneaniline (SA, see fig. 3.1).

Figure 3.1.: Structure of Salicylideneaniline

This molecule is a typical representative of aromatic Schiff bases.[115] Because of an easily accessible intramolecular proton transfer in the excited state (ESIPT) it shows a strong photochromic behavior. We not only wanted to estimate the time scales of the deactivation and the ESIPT process, but also to clarify the pathways that lead to different isomers and identify their properties.

Previous experimental and theoretical studies recognized the competition between different pathways.

Early experimental studies gained limited insight into the photodynamics of SA. X-ray data indicated that the cis-enol isomer is the most stable one.[116] It was shown that the excitation of the cis-enol isomer populates a bright $^1\pi\pi^*$ singlet excited state. A large Stokes shift in the fluorescence spectrum gave a hint for an ESIPT process. This was considered the main channel for excited state relaxation in the $^1\pi\pi^*$ state.

More recent studies were performed with femtosecond fluorescence up-conversion[115] and transient absorption spectroscopy.[117] This led to the following consensus pathway: The excitation of the cis-enol isomer triggers an ultrafast ESIPT within 50 fs and after relaxation within 500 fs the excited tautomer may be deactivated either radiatively to the cis-keto ground state or in a radiationless process to the trans-keto ground state.[118] The kinetics of these processes could not be established experimentally, since both products have a strong overlap in their absorption spectra.

Other studies proposed further deactivation mechanisms. Sliwa et al. identified a bleaching process within 100 fs, featuring an out-of-plane rotation to a long-lived twisted enol form in addition to the ESIPT.[118] An analogous assumption was already made earlier on the basis of nanosecond flash photolysis.[119, 120] A theoretical study using TD-DFT and quantum dynamics located an S_1/S_0 conical intersection that can be accessed by a rotation around the central C=N double bond and that leads to the twisted-enol isomer within 38 fs.[81] However, the proposed formation of the twisted-enol isomer could never be observed in ultrafast transient spectroscopy experiments,[115, 117, 121, 122] which calls for clarification.

The goal of our study was to determine the competing deactivation channels and their characteristic timescales. We used nonadiabatic surface hopping dynamics in combination with the OM2/MRCI semiempirical method. In order to validate the semiempirical method we optimized all relevant structures and calculated the vertical excitation energies. The optimized geometries were compared with DFT results (B3LYP functional), while the vertical excitation energies were validated against TD-DFT results obtained with different functionals (B3LYP, CAM-B3LYP, ωB97X-D and M06-2X). We also collected further vertical excitation energies from theoretical and experimental (estimations from absorption spectra) studies. All comparisons show that the use of OM2/MRCI for this system is justified.

We started a set of 209 trajectories in the first excited state and ran them for a total simulation time of 1 ps. After standard consistency checks, 125 trajectories fulfilled all our requirements and were included in the analysis. In all trajectories an ultrafast ESIPT process was observed that was completed within a few tens of femtoseconds. This indicates a barrierless proton transfer. We did not see any isomerization around the central C-N bond, which was supposed to be a deactivation channel competing with ESIPT.[81] The ultrafast ESIPT process is completed before the molecule can undergo a rotation around the C-N

bond, and hence the corresponding conical intersection is not accessible dynamically. After the proton is transferred, a different conical intersection can be reached through rotation around the central C-C bond. In all our trajectories the deactivation happened in a narrow region around this conical intersection. The observed preferences are likely caused by the strong hydrogen bond between the OH group and the N atom, which suppresses the free rotation of the aromatic side group and instead supports the transfer of the proton.

After deexcitation, the trajectories bifurcate and reach both the cis-keto and trans-keto ground-state isomers. While the trans-keto isomer is a stable photoproduct, the cis-keto isomer will transfer the hydrogen back to the oxygen atom and restore the initial cis-enol isomer. Therefore, 45% of all trajectories end up in the initial cis-enol isomer and 55% in the trans-keto photoproduct.

The ESIPT is usually completed in less than 100 fs, which enables an ultrafast deactivation to the ground state between 150 and 250 fs. For the trajectories reaching the cis-keto isomer, the ground-state intramolecular hydrogen transfer (GSIHT) is typically finished in an additional few hundred femtoseconds.

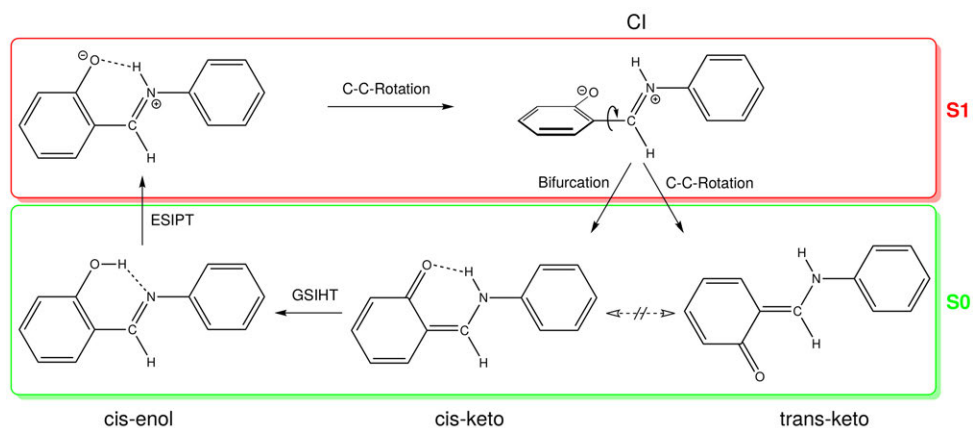The complete photocycle is shown in figure 3.2.

Figure 3.2.: Photocycle of salicylideneaniline

The radiationless deactivation of the excited state is strongly dependent on the ability to rotate around the central C-N or C-C bonds. This offers an easy way to control the quantum yield of the fluorescence. In a typical condensed-phase surrounding, the rotation of the aromatic side group requires too much space and will not happen in an efficient way. Experimentally, the system shows a very low fluorescence quantum yield in solution,[123] which can be increased by hindering the rotation around the central bonds via chemical modifications or rigid surroundings.[124, 125]

3. Summaries of publications

The nonadiabatic dynamics simulations with OM2/MRCI clarified that only the ESIPT channel is important for deactivation of the system and that the trans-enol isomer is never accessed in the dynamics. While static calculations and quantum dynamics with only a few dimensions can give valuable insights into a photocycle,[81] they cannot capture the dynamic competition between different deactivation channels. Our simulations also correctly identified the species responsible for fluorescence (cis-keto) and a stable photoproduct (trans-keto).

3.2. Nonequilibrium H/D Isotope Effects from Trajectory-Based Nonadiabatic Dynamics

Lasse Spörkel, Ganglong Cui, Axel Koslowski and Walter Thiel

The Journal of Physical Chemistry A, **2014**, 118, 152–157.

I carried out all OM2 calculations and performed the subsequent analysis. I wrote most parts of the manuscript. I created all included figures.[126]

In our second application project we addressed the excited-state deactivation times of 7-(2-pyridyl)indole and its deuterated analogue (see fig. 3.3).
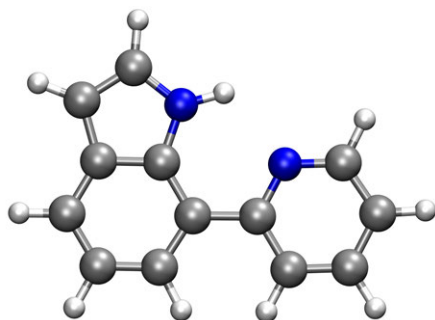

Figure 3.3.: Structure of 7-(2-pyridyl)indole

The isotopic substitution of an atom that is involved in a reaction can change the associated reaction rates. In the case of a barrierless nonequilibrium process, the difference in the rates should be directly related to the mass difference. To our knowledge, trajectory-based nonadiabatic dynamics have never been used before to explore nonequilibrium isotope effects.

7-(2-pyridyl)indole (7PyIn) was studied experimentally by absorption and fluorescence spectroscopy and found to show a strong Stokes shift.[127] Later, transient absorption spectroscopy gave a rough estimate of 1.0 ps for the excited-state deactivation time.[128] Higher resolution was possible with femtosecond pump-probe resonance-enhanced multiphoton ionization spectroscopy in a supersonic jet, which yielded deactivation time constants ascribed to the ESIPT process of 280 fs for 7PyIn and 390 fs for its deuterated analogue (7PyIn-D). A further

small signal was detected after about 1 ps and attributed to excited-state deactivation after torsional motion of the side group.[128]

Full-dimensional dynamics studies are indispensable for a detailed understanding of the whole photocycle and of the influence of deuteration on the rates. We ran extensive trajectory-based nonadiabatic dynamics simulations with OM2/MRCI both for 7PyIn and 7PyIn-D.

For validation purposes, we compared OM2/MRCI results for 7PyIn with those from high-level calculations (TD-DFT, DFT/MRCI and MS-CASPT2). The computed vertical excitation energies from OM2/MRCI were within the range of the high-level results: higher than the values from TD-DFT (with different functionals) and DFT/MRCI, but lower than the MS-CASPT2 values (with various active spaces and basis sets). The calculated potential energy surface showed an almost negligible barrier for the ESIPT process in the S_1 state of 1.5 kcal/mol with OM2/MRCI and 2.7 kcal/mol with MS-CASPT2, indicating a nearly barrierless transfer of the proton after excitation.

For the full-dimensional nonadiabatic dynamics, two sets of trajectories were run for 2 ps of simulation time. We measured the ESIPT times by adopting the criterion that the proton transfer has occurred when the distance to the initially bound N atom exceeds 1.5 Å. The corresponding analysis of the trajectories yielded average ESIPT times of 274 fs for 7PyIn and 339 ps for 7PyIn-D. These results are in good agreement with the experimental values.[128]

Additionally, we checked the influence of the initial temperature during trajectory preparation on the ESIPT time distribution. We found that a higher initial temperature leads to longer times for the proton transfer. This can be explained by the fact that higher kinetic energies (higher temperatures) lead to stronger distortions from the ground-state minimum structure in the initial sampling and in particular to more pronounced out-of-plane distortions that weaken the intramolecular hydrogen bond. After vertical photoexcitation, the ESIPT benefits from the presence of this hydrogen bond, and it will thus be faster at low temperatures and slower at higher temperatures.

The whole photocycle is shown in figure 3.4.

In summary, we successfully ran a large number of trajectory-based nonadiabatic dynamics with OM2/MRCI for this system (1367 successful trajectories) and demonstrated that it is possible to simulate nonequilibrium H/D isotope effects with this approach. The computed ESIPT times are in very good agreement with the experimental values. Additionally, we introduced an analysis tool that allowed us to correlate the ESIPT times with temperature fluctuations in the distribution of initial samples.
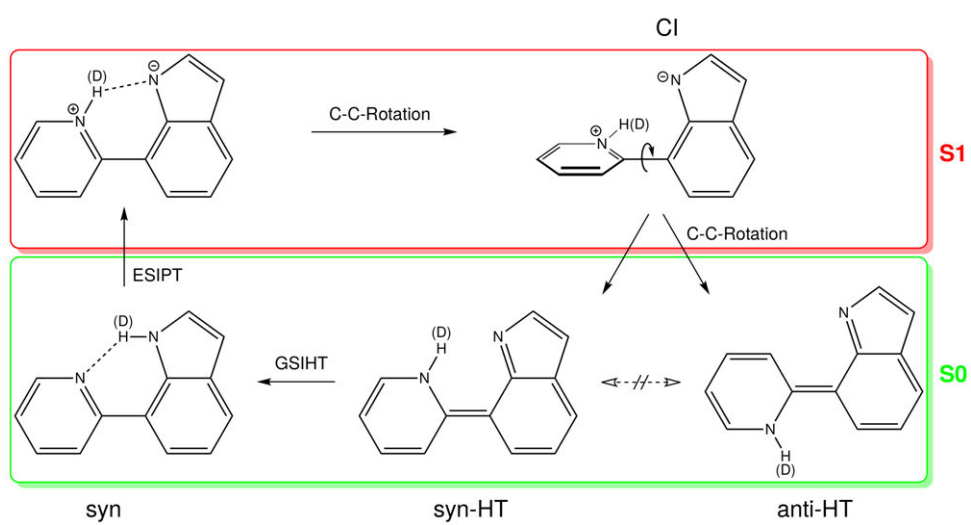
Figure 3.4.: Photocycle of 7-(2-pyridyl)indole

3.3. Photoswitching of Salicylidene Methylamine: A Theoretical Photodynamics Study

Lasse Spörkel, Joanna Jankowska and Walter Thiel

I carried out all calculations and performed the subsequent analysis. I wrote most parts of the manuscript. I created all included figures.[129]

Our third application project concerned the minimal photochromic Schiff base salicylidene methylamine (SMA, see figure 3.5).
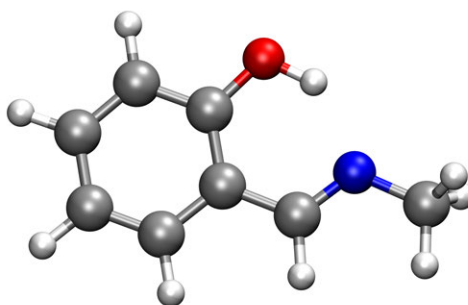
Figure 3.5.: Structure of Salicylidene Methylamine

Our goal was to elucidate the complete photocycle with all possible photoproducts and to assess the potential of SMA to act as photoswitching agent.

SMA meets all the qualitative requirements to be used as a photoswitch, since it has two stable photochromic isomers in the ground state, there is no overlap between their absorption spectra, and there exists a suitable conical intersection that allows radiationless deactivation of the excited state.[130, 131] Experimentally, the cis-enol isomer was identified as the most stable isomer, while the trans-keto isomer was assumed to be responsible for the observed photochromic behavior.[124, 132] The observed absorption and transient absorption spectra suggest a barrierless ESIPT process and an efficient nonradiative deactivation channel to the ground state.

Static calculations on SMA gave hints for a barrierless ESIPT process and located a conical

intersection that can be reached by rotation around the central C=C double bond and might allow for efficient excited state deactivation, but they do not provide a detailed understanding of all relevant photochannels and their competition.[80, 130, 133] Again the estimation of the efficiency of the photoswitching process requires full-dimensional dynamics simulations that involve all degrees of freedom.

In order to validate OM2/MRCI for SMA, we calculated vertical excitation energy profiles for the main reaction coordinates and compared them to previously published high-level *ab initio* CC2 results.[130] They were in good agreement: both methods show the same characteristics of two conical intersections and a barrierless ESIPT profile.

We started two sets of OM2/MRCI nonadiabatic TSH dynamics simulations from the two most stable ground-state isomers (cis-enol and trans-keto). For both molecules we could see an ultrafast excited state deactivation happening after ca. 100 fs for the trans-keto isomer and after ca. 150 fs for the cis-enol isomer. The longer deactivation time in the cis-enol case can be explained by the need for the initial ESIPT process to finish before the conical intersection can be accessed.

The bifurcation after passing of the conical intersection, and hence the photoproduct distribution, depends on which of the initial rotational isomer has been photoexcited. When starting from the trans-keto configuration, 90% of trajectories end up in the cis-isomer, while both rotational isomers are produced almost evenly when starting from the cis-enol configuration. This distinction is beneficial for the use of SMA as a photoswitching agent. It can be explained as follows. In order to access the relevant conical intersection, the dihedral angle around the central C=C bond needs to approach a value of 90 degree. This movement creates a momentum that drives the bifurcation towards the opposite rotational isomer. Furthermore, there is a general preference for cis-isomers because of a stabilizing intramolecular hydrogen bond. The combination of both effects accounts for the observed product distributions in a qualitative sense.

The formation of a very small amount (ca. 5%) of a rotated enol structure can be observed when the cis-enol isomer gets electronically excited. This corresponds to an inactive side product and shows that the ESIPT process is strongly preferred over the competing C-N bond rotation.

The complete photocycle is shown in figure 3.6.

To summarize, we explored the complete photocycle of SMA including all competing photoinduced processes with the use of OM2/MRCI nonadiabatic dynamics simulations. All the reported experimental features were well reproduced, and the overall mechanistic scenario allowed us to assess the merits of SMA-related systems as photoswitches.
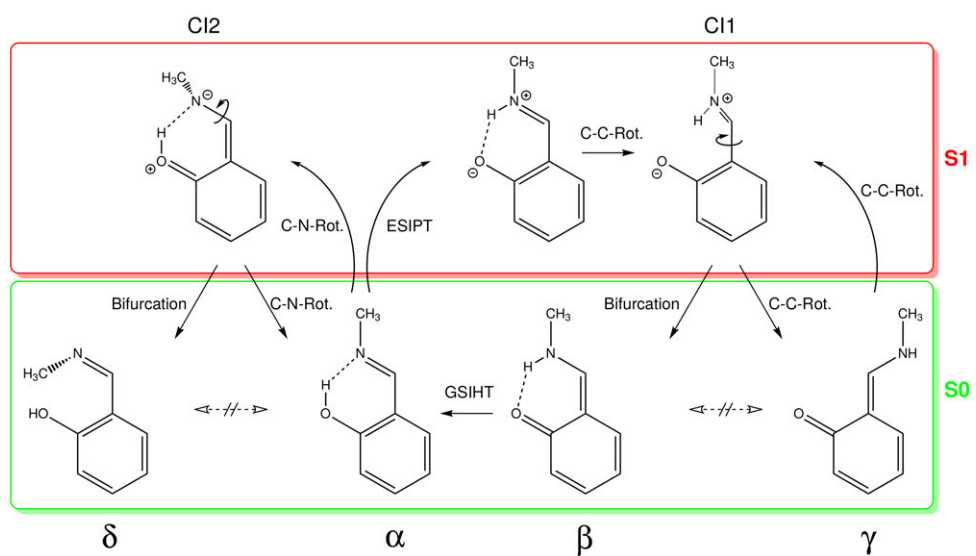
Figure 3.6.: Photocycle of Salicylidene Methylamine

3.4. Adaptive Time Steps in Trajectory Surface Hopping Simulations

Lasse Spörkel and Walter Thiel

I planned and implemented the adaptive time step. I carried out all example calculations and wrote most parts of the manuscript. I created all included figures.[134]

In our application projects we demonstrated the usefulness of trajectory-based nonadiabatic dynamics in combination with OM2/MRCI. Nevertheless we also encountered technical difficulties arising from the use of necessarily incomplete active spaces in the MRCI treatment. The interaction between active and inactive orbitals can cause local artifacts in the potential energy surface that may lead to energetic inconsistencies and problems in tracking certain properties along a trajectory.[71,72]

All of the previously mentioned problems can be diminished by using a smaller time step in the integration procedure of the dynamics. However, the time step cannot be chosen arbitrarily small, since the required number of steps for reaching a certain simulation time might grow strongly and become impractical. For this reason we introduced an adaptive procedure that can reduce the time step in an iterative manner, until a predetermined level of accuracy is achieved. This retains efficiency in unproblematic regions, while still maintaining high accuracy in regions with numeric difficulties.

The adaptive algorithm can be adjusted to check for customized criteria along a trajectory. In our implementation the first criterion is energy continuity, i.e. we compare the total energy of the system between two steps. If the energy does not stay constant and the difference surpasses a chosen threshold, the actual step is marked as invalid. As the second criterion we check the mapping of active orbitals. If the orbital overlaps of the best mapping are below a certain threshold, the step has to be redone. If one or more criteria fail, the actual dynamics step gets aborted and all results from the last correct step are restored. A new calculation is then done at half of the previous step size. When a step gets accepted as correct, all of the current results are stored for possible future restoration and a new calculation is done at the doubled actual step size. The full flow chart of the algorithm is shown in figure 3.7.
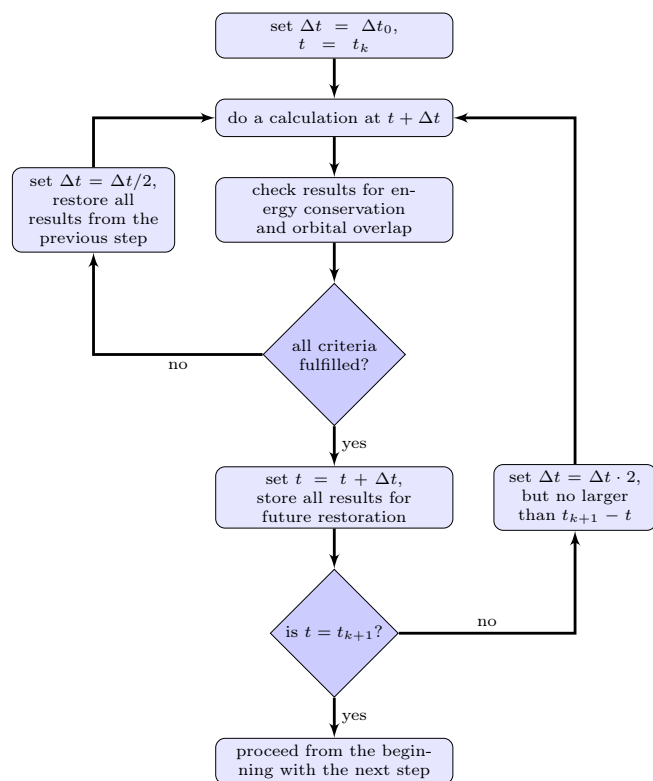
Figure 3.7.: Flowchart of the adaptive time step algorithm.[134]

In order to test our algorithm, we performed extensive comparisons of trajectory-based nonadiabatic dynamics simulations on two example molecules that have been previously investigated by our group (see figure 3.8).
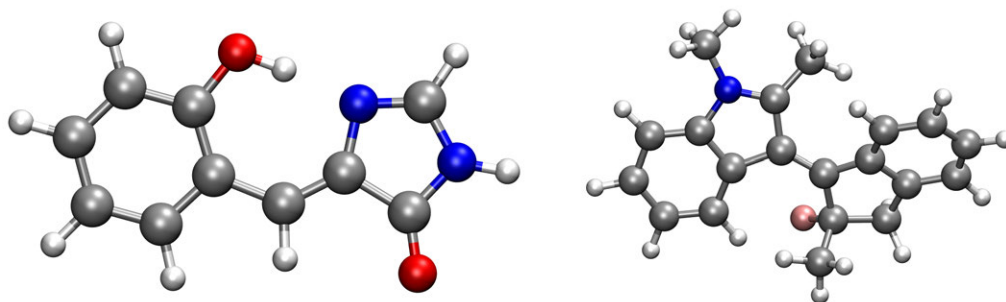
Figure 3.8.: Structure of the two example molecules: GFP chromophore (left) and F-NAIBP (right)

The first test case is the green fluorescent protein (GFP) chromophore (*4-(2-hydroxyben-*

zylidene)-1H-imidazol-5(4H)-one; OHBI), which was previously studied using nonadiabatic dynamics with fixed time steps and the OM2/MRCI method.[64] For a fair evaluation of the adaptive procedure, we started two sets of dynamics with 1000 trajectories each. It was immediately recognized that many trajectories (47%) fail when using the fixed time step procedure. This happened either because of numerical problems or non-constant total energies, which causes a rejection in our analysis scripts. With adaptive time steps, the ratio of failed trajectories could be strongly reduced to only 5%. This leads to a great improvement of computational efficiency and a higher accuracy along the trajectories, since the active orbital mapping is guaranteed to exceed a certain reliability level.

The analysis of all trajectories showed that the results of the nonadiabatic dynamics remained almost unchanged when comparing the constant with the adaptive time step runs. This indicates that the previous results obtained with constant time steps are still valid[64] and that we do not have to repeat all of our former projects.

In a second application example we studied a light-driven molecular motor, which was previously examined in our group (*3-[(2S)-2-fluoro-2-methyl-1-indanylidene]-1-methyl-2-me-thylindole*; F-NAIBP).[70]

This was the computationally most demanding system in our group until now that had been very prone to failures. The molecule consists of 41 atoms and the valence orbitals are very dense and close in energy. This leads to increased chances for orbitals changing their position and for a mixing of active and inactive orbitals. Although we deliberately chose a very small constant time step of 0.05 fs, only ca. 25% of all trajectories finished and fulfilled all of our continuity criteria. This percentage was greatly increased to a value of 96% of accepted trajectories by the use of adaptive time steps.

A high percentage of failed trajectories may reflect an intrinsic problem that affects trajectories reaching a certain region on the potential energy surface. Therefore, there is no guarantee that the final averaging over only 25% of all trajectories yields results representing the canonical ensemble. In our set of trajectories that use adaptive time steps, the lifetime of the excited state increases by ca. 19% with respect to the runs with constant time steps. However, the main qualitative conclusion drawn in the original publication[70] was the quantum efficiency of the photoisomerization. The use of the adaptive time step procedure had only very little effect on this value, and the main outcome of our previous work is thus still valid.[70]

The adaptive time step procedure is simple and easy to implement and the rejection criteria can be adjusted to any desired property. The computational effort will only be increased in situations where it is needed. Furthermore the simulation results become insensitive to the initially selected time step, since it will be decreased iteratively in problematic regions until

the desired accuracy is reached.

We thus recommend the use of adaptive time steps in all future projects, since it will never deteriorate the results, but will guarantee an increased efficiency and robustness.

3.5. Further publications: contributions as co-author

Semiempirical Quantum-Chemical Orthogonalization-Corrected Methods: Theory, Implementation, and Parameters

Pavlo O. Dral, Xin Wu, **Lasse Spörkel**, Axel Koslowski, Wolfgang Weber, Rainer Steiger, Mirjam Scholten and Walter Thiel

Journal of Chemical Theory and Computation, **2016**, 12, 1082–1096.

I implemented the D3 dispersion correction from Grimme[135] into MNDO.[136] I collected the CE345 benchmark set from Truhlar[137,138] and converted it into MNDO format. I carried out the calculations on the CE345 set and was involved in the planning and revision of the manuscript.[43]

Semiempirical Quantum-Chemical Orthogonalization-Corrected Methods: Benchmarks for Ground-State Properties

Pavlo O. Dral, Xin Wu, **Lasse Spörkel**, Axel Koslowski and Walter Thiel

Journal of Chemical Theory and Computation, **2016**, 12, 1097–1120.

See above.[44]

4. Conclusions and Outlook

In this thesis I presented several successful examples for the application of trajectory-based nonadiabatic dynamics using OM2/MRCI. We used this approach to elucidate the photoinduced processes of three molecules of recent research interest.[114, 126, 129] In all of our applications the ESIPT process was the preferred pathway after photoexcitation, which opened the opportunity to access alternative conical intersections and deactivation paths to the ground state.

Molecules that show an ESIPT after excitation have some unique experimental features like a strong Stokes shift in the fluorescence spectrum and ultrafast characteristics in time-resolved spectra. All of the experimental findings could be reproduced and explained by our simulations. Additionally we elucidated the complete photocycle of a possible candidate for a molecular photoswitch and were even able to quantify the switching quantum yield.[129]

We were able to demonstrate that despite of its simplicity the trajectory surface hopping method in combination with the fewest-switches criterion is a legitimate simulation technique that can help to understand complex problems.

The semiempirical OM2/MRCI method offers an excellent compromise between accuracy and computational efficiency. The large number of trajectories considered in this work (5633 trajectories in total) could not have been run with current *ab initio* methods. The low computational cost of OM2/MRCI allows for more complete sampling, better statistics in the averaging process and smaller time steps in the dynamics integration. Since we are currently working on the implementation of additional corrections and a reparametrization to more comprehensive benchmark data, the orthogonalization-corrected semiempirical methods are expected to become even more accurate. The planned incorporation of d-orbitals will enable the extension to heavier elements and allow for a wider range of applications, for example to large biomolecules containing hypervalent sulfur, phosphorus or transition metals.

Having recognized some flaws in the current TSH methods and procedures, we worked on an easy yet effective improvement to the dynamics code. The developed adaptive time step procedure allows an iterative increase in precision and stability in regions where this is needed.[134] It is simple to implement and can be adjusted to any criteria. The workflow of trajectory surface hopping simulations does not need to be changed, since the output file

format is not altered. We anticipate that the adaptive time step procedure will be used as a standard in future TSH projects.

To avoid failures that are connected to incomplete active spaces, one could alternatively use methods that do not require the selection of an active space and thus work more like a black-box method. Possible examples are single-reference methods, like configuration interaction singles (CIS) or linear response time-dependent DFT (TD-DFT) methods. However, they have their own intrinsic drawbacks, since in general single-reference methods cannot capture static correlation effects properly. Furthermore, TD-DFT methods do not provide a proper description in the vicinity of strong nonadiabatic couplings between the ground and the first excited state.

A different solution might be offered by the use of semiempirical multi-configuration SCF (MCSCF) methods. In the MCSCF procedure the MO and CI coefficients are optimized at the same time, which should avoid some of the active-space problems encountered at the MRCI level. However, the implementation of MCSCF methods and the generation of corresponding analytic gradients is not trivial and the computational costs might be high.

The ultimate goal would be to create a semiempirical method that can be applied to any kind of chemical problem (with a comprehensive ground- and excited-state parametrization), has intrinsic corrections to known flaws (e.g., dispersion and H-bonding), is able to treat a large range of elements (by incorporating a *spd* basis), does not suffer from active-space problems (e.g., using MCSCF) and provides a high level of accuracy while maintaining computational efficiency.

Bibliography

[1] M. Klessinger, J. Michl, *Excited states and photochemistry of organic molecules*, VCH, New York (USA), **1995**.

[2] E. S. Teller. The Crossing of Potential Surfaces. *J. Phys. Chem.* **1937**, *41*, 109–116.

[3] G. Herzberg, H. C. Longuet-Higgins. Intersection of potential energy surfaces in polyatomic molecules. *Discuss. Faraday Soc.* **1963**, *35*, 77–82.

[4] G. J. Atchity, S. S. Xantheas, K. Ruedenberg. Potential energy surfaces near intersections. *J. Chem. Phys.* **1991**, *95*, 1862–1876.

[5] F. Bernardi, M. Olivucci, M. A. Robb. Potential energy surface crossings in organic photochemistry. *Chem. Soc. Rev.* **1996**, *25*, 321–328.

[6] D. R. Yarkony. Conical intersections: The new conventional wisdom. *J. Phys. Chem. A* **2001**, *105*, 6277–6293.

[7] W. Domcke, D. R. Yarkony, H. Köppel (Eds.), *Conical intersections: electronic structure, dynamics and spectroscopy*, Vol. 15, World Scientific, Singapore, **2004**.

[8] W. Domcke, D. R. Yarkony, H. Köppel (Eds.), *Conical Intersections: Theory, Computation and Experiment*, Vol. 17, World Scientific, Singapore, **2011**.

[9] W. Domcke, D. R. Yarkony. Role of conical intersections in molecular spectroscopy and photoinduced chemical dynamics. *Annu. Rev. Phys. Chem.* **2012**, *63*, 325–352.

[10] B. O. Roos, K. Andersson, M. P. Fülscher, P. A. Malmqvist, L. Serrano-Andrés, K. Pierloot, M. Merchán, *Multiconfigurational Perturbation Theory: Applications in Electronic Spectroscopy* in *Advances in Chemical Physics: New Methods in Computational Quantum Mechanics, Vol. 93*, I. Prigogine, S. A. Rice (Eds.), John Wiley & Sons, **2007**, pp. 219–331.

[11] K. Andersson, P. A. Malmqvist, B. O. Roos, A. J. Sadlej, K. Wolinski. Second-order perturbation theory with a CASSCF reference function. *J. Phys. Chem.* **1990**, *94*, 5483–5488.

[12] K. Andersson, P. A. Malmqvist, B. O. Roos. Second-order perturbation theory with a complete active space self-consistent field reference function. *J. Chem. Phys.* **1992**, *96*, 1218–1226.

[13] B. O. Roos, *The Complete Active Space Self-Consistent Field Method and its Applications in Electronic Structure Calculations* in *Advances in Chemical Physics: Ab Initio Methods in Quantum Chemistry Part 2*, *Vol. 69*, K. P. Lawley (Ed.), John Wiley & Sons, **2007**, pp. 399–445.

[14] E. Runge, E. K. U. Gross. Density-Functional Theory for Time-Dependent Systems. *Phys. Rev. Lett.* **1984**, *52*, 997–1000.

[15] A. Dreuw, M. Head-Gordon. Single-Reference ab Initio Methods for the Calculation of Excited States of Large Molecules. *Chem. Rev.* **2005**, *105*, 4009–4037.

[16] S. Grimme. Density functional calculations with configuration interaction for the excited states of molecules. *Chem. Phys. Lett.* **1996**, *259*, 128–137.

[17] S. Grimme, M. Waletzke. A combination of Kohn–Sham density functional theory and multi-reference configuration interaction methods. *J. Chem. Phys.* **1999**, *111*, 5645–5655.

[18] I. Lyskov, M. Kleinschmidt, C. M. Marian. Redesign of the DFT/MRCI Hamiltonian. *J. Chem. Phys.* **2016**, *144*, 034104.

[19] J. F. Stanton, R. J. Bartlett. The equation of motion coupled-cluster method. A systematic biorthogonal approach to molecular excitation energies, transition probabilities, and excited state properties. *J. Chem. Phys.* **1993**, *98*, 7029–7039.

[20] H. Koch, P. Jørgensen. Coupled cluster response functions. *J. Chem. Phys.* **1990**, *93*, 3333–3344.

[21] O. Christiansen, H. Koch, P. Jørgensen. The second-order approximate coupled cluster singles and doubles model CC2. *Chem. Phys. Lett.* **1995**, *243*, 409–418.

[22] O. Christiansen, H. Koch, P. Jørgensen. Response functions in the CC3 iterative triple excitation model. *J. Chem. Phys.* **1995**, *103*, 7429–7441.

[23] H. Koch, O. Christiansen, P. Jørgensen, A. M. Sanchez de Merás, T. Helgaker. The CC3 model: An iterative coupled cluster approach including connected triples. *J. Chem. Phys.* **1997**, *106*, 1808–1818.

[24] K. Sneskov, O. Christiansen. Excited state coupled cluster methods. *WIREs Comput. Mol. Sci.* **2012**, *2*, 566–584.

[25] M. R. Silva-Junior, M. Schreiber, S. P. A. Sauer, W. Thiel. Benchmarks for electronically excited states: Time-dependent density functional theory and density functional theory based multireference configuration interaction. *J. Chem. Phys.* **2008**, *129*, 104103.

[26] M. Schreiber, M. R. Silva-Junior, S. P. A. Sauer, W. Thiel. Benchmarks for electronically excited states: CASPT2, CC2, CCSD, and CC3. *J. Chem. Phys.* **2008**, *128*, 134110.

[27] E. Tapavicza, A. M. Meyer, F. Furche. Unravelling the details of vitamin D photosynthesis by non-adiabatic molecular dynamics simulations. *Phys. Chem. Chem. Phys.* **2011**, *13*, 20986–20998.

[28] E. Tapavicza, G. D. Bellchambers, J. C. Vincent, F. Furche. Ab initio non-adiabatic molecular dynamics. *Phys. Chem. Chem. Phys.* **2013**, *15*, 18336–18348.

[29] J. W. Snyder, B. F. E. Curchod, T. J. Martínez. GPU-Accelerated State-Averaged Complete Active Space Self-Consistent Field Interfaced with Ab Initio Multiple Spawning Unravels the Photodynamics of Provitamin D3. *J. Phys. Chem. Lett.* **2016**, *7*, 2444–2449.

[30] A. Koslowski, M. E. Beck, W. Thiel. Implementation of a general multireference configuration interaction procedure with analytic gradients in a semiempirical context using the graphical unitary group approach. *J. Comput. Chem.* **2003**, *24*, 714–726.

[31] S. Patchkovskii, A. Koslowski, W. Thiel. Generic implementation of semi-analytical CI gradients for NDDO-type methods. *Theor. Chem. Acc.* **2005**, *114*, 84–89.

[32] M. J. S. Dewar, E. G. Zoebisch, E. F. Healy, J. J. P. Stewart. Development and use of quantum mechanical molecular models. 76. AM1: a new general purpose quantum mechanical molecular model. *J. Am. Chem. Soc.* **1985**, *107*, 3902–3909.

[33] J. J. P. Stewart. Optimization of parameters for semiempirical methods I. Method. *J. Comput. Chem.* **1989**, *10*, 209–220.

[34] J. J. P. Stewart. Optimization of parameters for semiempirical methods II. Applications. *J. Comput. Chem.* **1989**, *10*, 221–264.

[35] M. J. S. Dewar, W. Thiel. Ground states of molecules. 38. The MNDO method. Approximations and parameters. *J. Am. Chem. Soc.* **1977**, *99*, 4899–4907.

[36] M. J. S. Dewar, W. Thiel. Ground states of molecules. 39. MNDO results for molecules containing hydrogen, carbon, nitrogen, and oxygen. *J. Am. Chem. Soc.* **1977**, *99*, 4907–4917.

[37] J. J. P. Stewart. Optimization of parameters for semiempirical methods V: Modification of NDDO approximations and application to 70 elements. *J. Mol. Model.* **2007**, *13*, 1173–1213.

[38] J. J. P. Stewart. Optimization of parameters for semiempirical methods VI: more modifications to the NDDO approximations and re-optimization of parameters. *J. Mol. Model.* **2013**, *19*, 1–32.

[39] M. Kolb, W. Thiel. Beyond the MNDO model: Methodical considerations and numerical results. *J. Comput. Chem.* **1993**, *14*, 775–789.

[40] W. Weber, *Ein neues semiempirisches NDDO-Verfahren mit Orthogonalisierungskorrekturen: Entwicklung des Modells, Parametrisierung und Anwendungen*, Ph.D. thesis, Universität Zürich, **1996**.

[41] W. Weber, W. Thiel. Orthogonalization corrections for semiempirical methods. *Theor. Chem. Acc.* **2000**, *103*, 495–506.

[42] M. Scholten, *Semiempirische Verfahren mit Orthogonalisierungskorrekturen: Die OM3 Methode*, Ph.D. thesis, Heinrich Heine Universität Düsseldorf, **2003**.

[43] P. O. Dral, X. Wu, L. Spörkel, A. Koslowski, W. Weber, R. Steiger, M. Scholten, W. Thiel. Semiempirical Quantum-Chemical Orthogonalization-Corrected Methods: Theory, Implementation, and Parameters. *J. Chem. Theory Comput.* **2016**, *12*, 1082–1096.

[44] P. O. Dral, X. Wu, L. Spörkel, A. Koslowski, W. Thiel. Semiempirical Quantum-Chemical Orthogonalization-Corrected Methods: Benchmarks for Ground-State Properties. *J. Chem. Theory Comput.* **2016**, *12*, 1097–1120.

[45] D. Tuna, Y. Lu, A. Koslowski, W. Thiel. Semiempirical Quantum-Chemical Orthogonalization-Corrected Methods: Benchmarks of Electronically Excited States. *J. Chem. Theory Comput.* **2016**, *12*, 4400–4422.

[46] J. C. Tully. Molecular dynamics with electronic transitions. *J. Chem. Phys.* **1990**, *93*, 1061–1071.

[47] M. Barbatti. Nonadiabatic dynamics with trajectory surface hopping method. *WIREs Comput. Mol. Sci.* **2011**, *1*, 620–633.

[48] J. C. Tully. Mixed quantum-classical dynamics. *Faraday Discuss.* **1998**, *110*, 407–419.

[49] E. Wigner. On the Quantum Correction For Thermodynamic Equilibrium. *Phys. Rev.* **1932**, *40*, 749–759.

[50] M. Barbatti, G. Granucci, M. Persico, M. Ruckenbauer, M. Vazdar, M. Eckert-Maksić,

H. Lischka. The on-the-fly surface-hopping program system Newton-X: Application to ab initio simulation of the nonadiabatic photodynamics of benchmark systems. *J. Photochem. Photobiol., A* **2007**, *190*, 228–240.

[51] G. Granucci, M. Persico. Critical appraisal of the fewest switches algorithm for surface hopping. *J. Chem. Phys.* **2007**, *126*, 134114.

[52] G. Granucci, M. Persico, A. Zoccante. Including quantum decoherence in surface hopping. *J. Chem. Phys.* **2010**, *133*, 134111.

[53] J. E. Subotnik, N. Shenvi. A new approach to decoherence and momentum rescaling in the surface hopping algorithm. *J. Chem. Phys.* **2011**, *134*, 024105.

[54] N. Shenvi, J. E. Subotnik, W. Yang. Phase-corrected surface hopping: Correcting the phase evolution of the electronic wavefunction. *J. Chem. Phys.* **2011**, *135*, 024101.

[55] E. Fabiano, W. Thiel. Nonradiative Deexcitation Dynamics of 9H-Adenine: An OM2 Surface Hopping Study. *J. Phys. Chem. A* **2008**, *112*, 6859–6863.

[56] Z. Lan, E. Fabiano, W. Thiel. Photoinduced Nonadiabatic Dynamics of 9H-Guanine. *ChemPhysChem* **2009**, *10*, 1225–1229.

[57] Z. Lan, E. Fabiano, W. Thiel. Photoinduced Nonadiabatic Dynamics of Pyrimidine Nucleobases: On-the-Fly Surface-Hopping Study with Semiempirical Methods. *J. Phys. Chem. B* **2009**, *113*, 3548–3555.

[58] A. Kazaryan, Z. Lan, L. V. Schäfer, W. Thiel, M. Filatov. Surface Hopping Excited-State Dynamics Study of the Photoisomerization of a Light-Driven Fluorene Molecular Rotary Motor. *J. Chem. Theory Comput.* **2011**, *7*, 2189–2199.

[59] O. Weingart, Z. Lan, A. Koslowski, W. Thiel. Chiral Pathways and Periodic Decay in cis-Azobenzene Photodynamics. *J. Phys. Chem. Lett.* **2011**, *2*, 1506–1509.

[60] Y. Lu, Z. Lan, W. Thiel. Hydrogen Bonding Regulates the Monomeric Nonradiative Decay of Adenine in DNA Strands. *Angew. Chem. Int. Ed.* **2011**, *50*, 6864–6867.

[61] Z. Lan, Y. Lu, E. Fabiano, W. Thiel. QM/MM Nonadiabatic Decay Dynamics of 9H-Adenine in Aqueous Solution. *ChemPhysChem* **2011**, *12*, 1989–1998.

[62] Z. Lan, Y. Lu, O. Weingart, W. Thiel. Nonadiabatic Decay Dynamics of a Benzylidene Malononitrile. *J. Phys. Chem. A* **2012**, *116*, 1510–1518.

[63] G. Cui, W. Thiel. Nonadiabatic dynamics of a truncated indigo model. *Phys. Chem. Chem. Phys.* **2012**, *14*, 12378–12384.

[64] G. Cui, Z. Lan, W. Thiel. Intramolecular Hydrogen Bonding Plays a Crucial Role in

the Photophysics and Photochemistry of the GFP Chromophore. *J. Am. Chem. Soc.* **2012**, *134*, 1662–1672.

[65] B. Heggen, Z. Lan, W. Thiel. Nonadiabatic decay dynamics of 9H-guanine in aqueous solution. *Phys. Chem. Chem. Phys.* **2012**, *14*, 8137–8146.

[66] G. Cui, W. Thiel. Photoinduced Ultrafast Wolff Rearrangement: A Non-Adiabatic Dynamics Perspective. *Angew. Chem. Int. Ed.* **2013**, *52*, 433–436.

[67] J. A. Gamez, A. Koslowski, W. Thiel. Enhanced E → Z photoisomerisation in 2-aminoazobenzene. *RSC Adv.* **2014**, *4*, 1886–1889.

[68] D. Fazzi, M. Barbatti, W. Thiel. Modeling ultrafast exciton deactivation in oligothiophenes via nonadiabatic dynamics. *Phys. Chem. Chem. Phys.* **2015**, *17*, 7787–7799.

[69] D. Fazzi, M. Barbatti, W. Thiel. Unveiling the Role of Hot Charge-Transfer States in Molecular Aggregates via Nonadiabatic Dynamics. *J. Am. Chem. Soc.* **2016**, *138*, 4502–4511.

[70] A. Nikiforov, J. A. Gamez, W. Thiel, M. Filatov. Computational Design of a Family of Light-Driven Rotary Molecular Motors with Improved Quantum Efficiency. *J. Phys. Chem. Lett.* **2016**, *7*, 105–110.

[71] T. W. Keal, M. Wanko, W. Thiel. Assessment of semiempirical methods for the photoisomerisation of a protonated Schiff base. *Theor. Chem. Acc.* **2009**, *123*, 145–156.

[72] E. Fabiano, T. W. Keal, W. Thiel. Implementation of surface hopping molecular dynamics using semiempirical methods. *Chem. Phys.* **2008**, *349*, 334–347.

[73] E. Hadjoudis, I. M. Mavridis. Photochromism and thermochromism of Schiff bases in the solid state: structural aspects. *Chem. Soc. Rev.* **2004**, *33*, 579–588.

[74] A. L. Sobolewski, W. Domcke. Evidence for the need of a non-Born—Oppenheimer description of excited-state hydrogen transfer. *Chem. Phys. Lett.* **1993**, *211*, 82–87.

[75] A. L. Sobolewski, W. Domcke. Photophysics of intramolecularly hydrogen-bonded aromatic systems: ab initio exploration of the excited-state deactivation mechanisms of salicylic acid. *Phys. Chem. Chem. Phys.* **2006**, *8*, 3410–3417.

[76] A. L. Sobolewski. Reversible molecular switch driven by excited-state hydrogen transfer. *Phys. Chem. Chem. Phys.* **2008**, *10*, 1243–1247.

[77] L. Lapinski, M. J. Nowak, J. Nowacki, M. F. Rode, A. L. Sobolewski. A Bistable Molecular Switch Driven by Photoinduced Hydrogen-Atom Transfer. *ChemPhysChem* **2009**, *10*, 2290–2295.

[78] A. L. Sobolewski, W. Domcke, C. Hättig. Photophysics of Organic Photostabilizers. Ab Initio Study of the Excited-State Deactivation Mechanisms of 2-(2'-Hydroxyphenyl)benzotriazole. *J. Phys. Chem. A* **2006**, *110*, 6301–6306.

[79] A. L. Sobolewski, W. Domcke. Computational Studies of the Photophysics of Hydrogen-Bonded Molecular Systems. *J. Phys. Chem. A* **2007**, *111*, 11725–11735.

[80] J. M. Ortiz-Sánchez, R. Gelabert, M. Moreno, J. M. Lluch. Theoretical Study on the Excited-State Intramolecular Proton Transfer in the Aromatic Schiff Base Salicylidene Methylamine: an Electronic Structure and Quantum Dynamical Approach. *J. Phys. Chem. A* **2006**, *110*, 4649–4656.

[81] J. M. Ortiz-Sánchez, R. Gelabert, M. Moreno, J. M. Lluch. Electronic-structure and quantum dynamical study of the photochromism of the aromatic Schiff base salicylideneaniline. *J. Chem. Phys.* **2008**, *129*, 214308.

[82] I. Gómez, M. Reguero, M. Boggio-Pasqua, M. A. Robb. Intramolecular Charge Transfer in 4-Aminobenzonitriles Does Not Necessarily Need the Twist. *J. Am. Chem. Soc.* **2005**, *127*, 7119–7129.

[83] A. Migani, L. Blancafort, M. A. Robb, A. D. DeBellis. An Extended Conical Intersection Seam Associated with a Manifold of Decay Paths: Excited-State Intramolecular Proton Transfer in o-Hydroxybenzaldehyde. *J. Am. Chem. Soc.* **2008**, *130*, 6932–6933.

[84] C.-J. Xia, D.-S. Liu, H.-C. Liu, Y.-T. Zhang. A possible salicylideneanilines-based optical molecular switch induced by a reversible hydrogen transfer: an ab initio study. *Mol. Phys.* **2011**, *109*, 209–215.

[85] M. F. Rode, A. L. Sobolewski. Effect of Chemical Substituents on the Energetical Landscape of a Molecular Photoswitch: An Ab Initio Study. *J. Phys. Chem. A* **2010**, *114*, 11879–11889.

[86] A. Szabo, N. S. Ostlund, *Modern Quantum Chemistry: Introduction to Advanced Electronic Structure Theory*, Dover Publications, Mineola, New York (USA), **1996**.

[87] D. A. McQuarrie, *Quantum Chemistry*, University Science Books, Sausalito, California (USA), **2008**.

[88] I. N. Levine, *Quantum Chemistry*, in *Pearson Education*, Prentice Hall, Upper Saddle River, New Jersey (USA), **2009**.

[89] M. Born, R. Oppenheimer. Zur Quantentheorie der Molekeln. *Ann. Phys.* **1927**, *389*, 457–484.

[90] W. Thiel. Semiempirical methods: Current status and perspectives. *Tetrahedron* **1988**, *44*, 7393–7408.

[91] W. Thiel. Perspectives on semiempirical molecular orbital theory. *Adv. Chem. Phys.* **1996**, *93*, 703–757.

[92] W. Thiel, *Semiempirical Quantum-Chemical Methods in Computational Chemistry* in *Theory and Applications of Computational Chemistry: The First Forty Years*, C. E. Dykstra, G. Frenking, K. S. Kim, G. E. Scuseria (Eds.), Elsevier, **2005**, pp. 559–580.

[93] W. Thiel. Semiempirical quantum–chemical methods. *WIREs Comput. Mol. Sci.* **2014**, *4*, 145–157.

[94] J. A. Pople, D. P. Santry, G. A. Segal. Approximate Self-Consistent Molecular Orbital Theory. I. Invariant Procedures. *J. Chem. Phys.* **1965**, *43*, S129–S135.

[95] N. Otte, M. Scholten, W. Thiel. Looking at Self-Consistent-Charge Density Functional Tight Binding from a Semiempirical Perspective. *J. Phys. Chem. A* **2007**, *111*, 5751–5755.

[96] M. R. Silva-Junior, W. Thiel. Benchmark of Electronically Excited States for Semiempirical Methods: MNDO, AM1, PM3, OM1, OM2, OM3, INDO/S, and INDO/S2. *J. Chem. Theory Comput.* **2010**, *6*, 1546–1564.

[97] M. Korth, W. Thiel. Benchmarking Semiempirical Methods for Thermochemistry, Kinetics, and Noncovalent Interactions: OMx Methods Are Almost As Accurate and Robust As DFT-GGA Methods for Organic Molecules. *J. Chem. Theory Comput.* **2011**, *7*, 2929–2936.

[98] S. Patchkovskii, W. Thiel. Analytical first derivatives of the energy for small CI expansions. *Theor. Chem. Acc.* **1997**, *98*, 1–4.

[99] S. Nosé. A unified formulation of the constant temperature molecular dynamics methods. *J. Chem. Phys.* **1984**, *81*, 511–519.

[100] W. G. Hoover. Canonical dynamics: Equilibrium phase-space distributions. *Phys. Rev. A* **1985**, *31*, 1695–1697.

[101] G. J. Martyna, M. L. Klein, M. Tuckerman. Nosé-Hoover chains: The canonical ensemble via continuous dynamics. *J. Chem. Phys.* **1992**, *97*, 2635–2643.

[102] B. Bransden, C. Joachain, *Physics of Atoms and Molecules*, in *Pearson Education*, Prentice Hall, Harlow (England), **1983**.

[103] G. A. Worth, M. A. Robb, *Applying Direct Molecular Dynamics to Non-Adiabatic*

Systems in *The Role of Degenerate States in Chemistry, Vol. 124*, M. Baer, G. D. Billing (Eds.), John Wiley & Sons, **2003**, pp. 355–431.

[104] E. Tapavicza, I. Tavernelli, U. Rothlisberger. Trajectory Surface Hopping within Linear Response Time-Dependent Density-Functional Theory. *Phys. Rev. Lett.* **2007**, *98*, 023001.

[105] D. R. Yarkony. Nonadiabatic Quantum Chemistry - Past, Present, and Future. *Chem. Rev.* **2011**, *112*, 481–498.

[106] J. C. Tully. Perspective: Nonadiabatic dynamics theory. *J. Chem. Phys.* **2012**, *137*, 22A301.

[107] M. Persico, G. Granucci. An overview of nonadiabatic dynamics simulations methods, with focus on the direct approach versus the fitting of potential energy surfaces. *Theor. Chem. Acc.* **2014**, *133*, 1–28.

[108] M. Barbatti, R. Crespo-Otero, *Surface Hopping Dynamics with DFT Excited States* in *Density-Functional Methods for Excited States*, N. Ferré, M. Filatov, M. Huix-Rotllant (Eds.), Springer International Publishing, Cham, **2016**, pp. 415–444.

[109] R. B. Gerber, D. Shemesh, M. E. Varner, J. Kalinowski, B. Hirshberg. Ab initio and semi-empirical Molecular Dynamics simulations of chemical reactions in isolated molecules and in clusters. *Phys. Chem. Chem. Phys.* **2014**, *16*, 9760–9775.

[110] R. B. Gerber, V. Buch, M. A. Ratner. Time-dependent self-consistent field approximation for intramolecular energy transfer. I. Formulation and application to dissociation of van der Waals molecules. *J. Chem. Phys.* **1982**, *77*, 3022–3030.

[111] M. H. Beck, A. Jäckle, G. A. Worth, H.-D. Meyer. The multiconfiguration time-dependent Hartree (MCTDH) method: a highly efficient algorithm for propagating wavepackets. *Phys. Rep.* **2000**, *324*, 1–105.

[112] H. Wang, M. Thoss. Multilayer formulation of the multiconfiguration time-dependent Hartree theory. *J. Chem. Phys.* **2003**, *119*, 1289–1299.

[113] M. Ben-Nun, T. J. Martínez. Nonadiabatic molecular dynamics: Validation of the multiple spawning method for a multidimensional problem. *J. Chem. Phys.* **1998**, *108*, 7244–7257.

[114] L. Spörkel, G. Cui, W. Thiel. Photodynamics of Schiff Base Salicylideneaniline: Trajectory Surface-Hopping Simulations. *J. Phys. Chem. A* **2013**, *117,* 4574–4583.

[115] W. Rodríguez-Córdoba, J. S. Zugazagoitia, E. Collado-Fregoso, J. Peon. Excited state

intramolecular proton transfer in schiff bases. Decay of the locally excited enol state observed by femtosecond resolved fluorescence. *J. Phys. Chem. A* **2007**, *111*, 6241–6247.

[116] R. Destro, A. Gavezzotti, M. Simonetta. Salicylideneaniline. *Acta Cryst. Sect. B* **1978**, *34*, 2867–2869.

[117] M. Ziółek, J. Kubicki, A. Maciejewski, R. Naskręcki, A. Grabowska. An ultrafast excited state intramolecular proton transfer (ESPIT) and photochromism of salicylideneaniline (SA) and its "double" analogue salicylaldehyde azine (SAA). A controversial case. *Phys. Chem. Chem. Phys.* **2004**, *6*, 4682–4689.

[118] M. Sliwa, N. Mouton, C. Ruckebusch, L. Poisson, A. Idrissi, S. Aloïse, L. Potier, J. Dubois, O. Poizat, G. Buntinx. Investigation of ultrafast photoinduced processes for salicylidene aniline in solution and gas phase: toward a general photo-dynamical scheme. *Photochem. Photobiol. Sci.* **2010**, *9*, 661–669.

[119] D. G. Anderson, G. Wettermark. Photoinduced Isomerizations in Anils. *J. Am. Chem. Soc.* **1965**, *87*, 1433–1438.

[120] M. Ottolenghi, D. S. McClure. Photochromism. II. Photochemistry of Salicylideneaniline. *J. Chem. Phys.* **1967**, *46*, 4620–4629.

[121] S. Mitra, N. Tamai. Dynamics of photochromism in salicylideneaniline: A femtosecond spectroscopic study. *Phys. Chem. Chem. Phys.* **2003**, *5*, 4647–4652.

[122] C. Okabe, T. Nakabayashi, Y. Inokuchi, N. Nishi, H. Sekiya. Ultrafast excited-state dynamics in photochromic N-salicylideneaniline studied by femtosecond time-resolved REMPI spectroscopy. *J. Chem. Phys.* **2004**, *121*, 9436–9442.

[123] M. I. Knyazhansky, A. V. Metelitsa, A. J. Bushkov, S. M. Aldoshin. Role of structural flexibility in fluorescence and photochromism of the salicylideneaniline: the aldehyde ring rotation. *Journal of Photochemistry & Photobiology, A: Chemistry* **1996**, *97*, 121–126.

[124] M. I. Knyazhansky, A. V. Metelitsa, M. E. Kletskii, A. A. Millov, S. O. Besugliy. The structural transformations and photo-induced processes in salicylidene alkylimines. *J. Mol. Struct.* **2000**, *526*, 65–79.

[125] M. Sliwa, N. Mouton, C. Ruckebusch, S. Aloïse, O. Poizat, G. Buntinx, R. Métivier, K. Nakatani, H. Masuhara, T. Asahi. Comparative Investigation of Ultrafast Photoinduced Processes in Salicylidene-Aminopyridine in Solution and Solid State. *J. Phys. Chem. C* **2009**, *113*, 11959–11968.

[126] L. Spörkel, G. Cui, A. Koslowski, W. Thiel. Nonequilibrium H/D Isotope Effects from Trajectory-Based Nonadiabatic Dynamics. *J. Phys. Chem. A* **2014**, *118*, 152–157.

[127] G. Wiosna, I. Petkova, M. S. Mudadu, R. P. Thummel, J. Waluk. Intra- and inter-molecular fluorescence quenching in 7-(pyridyl)indoles. *Chem. Phys. Lett.* **2004**, *400*, 379–383.

[128] Y. Nosenko, G. Wiosna-Sałyga, M. Kunitski, I. Petkova, A. Singh, W. J. Buma, R. P. Thummel, B. Brutschy, J. Waluk. Proton transfer with a twist? Femtosecond Dynamics of 7-(2-pyridyl)indole in Condensed Phase and in Supersonic Jets. *Angew. Chem. Int. Ed.* **2008**, *47*, 6037–6040.

[129] L. Spörkel, J. Jankowska, W. Thiel. Photoswitching of Salicylidene Methylamine: A Theoretical Photodynamics Study. *J. Phys. Chem. B* **2015**, *119*, 2702–2710.

[130] J. Jankowska, M. F. Rode, J. Sadlej, A. L. Sobolewski. Photophysics of Schiff Bases: Theoretical Study of Salicylidene Methylamine. *ChemPhysChem* **2012**, *13*, 4287–4294.

[131] J. Jankowska, M. F. Rode, J. Sadlej, A. L. Sobolewski. Excited-State Intramolecular Proton Transfer: Photoswitching in Salicylidene Methylamine Derivatives. *ChemPhysChem* **2014**, *15*, 1643–1652.

[132] M. Z. Zgierski, A. Grabowska. Theoretical approach to photochromism of aromatic Schiff bases: A minimal chromophore salicylidene methylamine. *J. Chem. Phys.* **2000**, *113*, 7845–7852.

[133] A. Grabowska, K. Kownacki, Ł. Kaczmarek. Structural Aspects of Photochromism of the Internally H-Bonded Schiff Bases. "A Minimal Chromophore". *Acta Phys. Pol. A* **1995**, *88*, 1081–1088.

[134] L. Spörkel, W. Thiel. Adaptive time steps in trajectory surface hopping simulations. *J. Chem. Phys.* **2016**, *144*, 194108.

[135] S. Grimme, J. Antony, S. Ehrlich, H. Krieg. A consistent and accurate ab initio parametrization of density functional dispersion correction (DFT-D) for the 94 elements H-Pu. *J. Chem. Phys.* **2010**, *132*, 154104.

[136] W. Thiel, *MNDO2005 program, version 7.0*, **2005**, Max-Planck-Institut für Kohlenforschung, Mülheim, Germany.

[137] *The Minnesota databases. Accessed on July 24th, 2014.* http://comp.chem.umn.edu/db/.

[138] R. Peverati, D. G. Truhlar. Quest for a universal density functional: the accuracy of

density functionals across a broad spectrum of databases in chemistry and physics. *Philosophical Transactions of the Royal Society of London A: Mathematical, Physical and Engineering Sciences* **2014**, *372*.

A. Photodynamics of Schiff Base Salicylideneaniline: Trajectory Surface-Hopping Simulations

Lasse Spörkel, Ganglong Cui and Walter Thiel

I carried out all calculations and performed the subsequent analysis. I wrote most parts of the manuscript. I created all included figures.

Photodynamics of Schiff Base Salicylideneaniline: Trajectory Surface-Hopping Simulations

Lasse Spörkel, Ganglong Cui,* and Walter Thiel*

Max-Planck-Institut für Kohlenforschung, Kaiser-Wilhelm-Platz 1, 45470 Mülheim an der Ruhr, Germany

S *Supporting Information*

ABSTRACT: We report a computational study on the photochemistry of the prototypical aromatic Schiff base salicylideneaniline in the gas phase using static electronic structure calculations (TDDFT, OM2/MRCI) and surface-hopping dynamics simulations (OM2/MRCI). Upon photoexcitation of the most stable cis-enol tautomer into the bright S_1 state, we find an ultrafast excited-state proton transfer that is complete within tens of femtoseconds, without any C=N double bond isomerization. The internal conversion of the resulting S_1 cis-keto species is initiated by an out-of-plane motion around the C–C single bond, which guides the molecule toward a conical intersection that provides an efficient deactivation channel to the ground state. We propose that the ease of this C–C single bond rotation regulates fluorescence quenching and photocoloration in condensed-phase environments. In line with previous work, we find the S_1 cis-keto conformer to be responsible for fluorescence, especially in rigid surroundings. The S_0 cis-keto species is a transient photoproduct, while the stable S_0 trans-keto photoproduct is responsible for photochromism. The trajectory calculations yield roughly equal amounts of the S_0 cis-enol and trans-keto photoproducts. Methodologically, full-dimensional nonadiabatic dynamics simulations are found necessary to capture the preferences among competitive channels and to gain detailed mechanistic insight into Schiff base photochemistry.
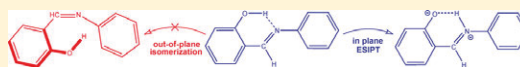
■ INTRODUCTION

Photochromism is of crucial importance for the development of photomemories, photoswitches, optical data processing, and data storage materials.[1−10] Aromatic Schiff bases are among the most popular photochromic compounds, and their photochemistry has been extensively studied in past decades. They undergo fast excited-state intramolecular proton transfer, which makes them potentially very valuable for switching applications.

Experimentally, the most thoroughly explored aromatic photochromic Schiff base is salicylideneaniline (Figure 1). In the following, we briefly summarize a few issues that have been debated over the years on the experimental side.

Relaxation Dynamics. Photoexcitation of the most stable cis-enol tautomer populates the lowest bright $^1\pi\pi^*$ singlet excited state. The corresponding strong absorption is found between 300 and 400 nm. The fluorescence spectrum shows a
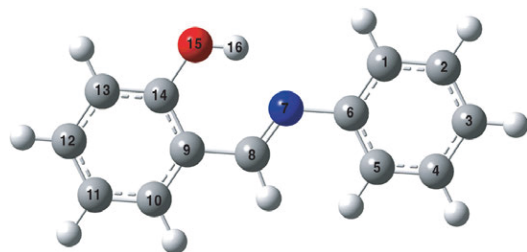

Figure 1. Schiff base salicylideneaniline with the chosen atom numbering.

large Stokes shift, with the first band around 570 nm, which indicates an excited-state intramolecular proton transfer (ESIPT) that leads to the cis-keto tautomer. This ESIPT has been observed in numerous experiments and is commonly considered to be the main excited-state relaxation process in the $^1\pi\pi^*$ state. However, other ultrafast relaxation processes have also been reported by Sliwa et al. (within 100 fs, out-of-plane rotation to the twisted-enol form in addition to ESIPT)[11] and by Mitra and Tamai (within a few hundred femtoseconds).[12] It has also been proposed that $^1\pi\pi^* \rightarrow {}^1n\pi^*$ internal conversion may occur both in the cis-enol form and the cis-keto form, which could serve as an alternative relaxation channel.[13−15]

Time Scales. The experimentally derived time constants for the $^1\pi\pi^*$ intramolecular excited-state proton transfer differ significantly. Using various types of femtosecond spectroscopy, early studies reported ESIPT rates of $(210 \text{ fs})^{-1}$ in cyclohexane and $(380 \text{ fs})^{-1}$ in ethanol,[14] ESIPT and internal conversion processes that occur within 750 fs,[13] proton transfer and photochromic product formation within a few hundred femtoseconds,[12] and typical ESIPT times of 200−300 fs for most of the solvents.[16] With increasing time resolution of the experiments, these values became smaller. The characteristic times for the ESIPT process were found to be below 50 fs[17,18] and in the sub-100 fs regime.[11,19] This time scale is now commonly accepted.

Fluorescence Quenching and Photocoloration. Salicylideneaniline has an ultralow fluorescence quantum yield (ca.

1.2×10^{-4} in acetonitrile)[17] because of ultrafast excited-state deactivation. This yield is higher in rigid media and can also be increased by chemical modification. Salicylideneaniline exhibits photochromism both in the crystalline phase and in solution.[20−22] There is consensus that the photocolored species is the trans-keto tautomer. It is long-lived in the solid state and transient in solution, implying that there is an efficient internal conversion channel for the photocolored species, which is accessible in solution but is blocked in the solid state.

Characterization of the Transient Photoproducts and Their Precursors. Yuzawa et al. formulated a resonance hybrid between quinoid and zwitterionic structures to describe the transient trans-keto species, and they suggested that the relative contribution of these two structures will depend on the solvent environment.[23] Barbara et al. proposed that the photochromic product is formed from the vibrationally hot cis-keto tautomer generated by ESIPT.[21] Harada et al. identified a trans-keto form to be the long-lived transient in the crystalline state.[24]

On the theoretical side, early studies of salicylideneaniline mainly focused on electronic structure calculations at the semiempirical and Hartree−Fock (HF) levels.[17,25−31] Kletskii et al. employed the PM3 method to explore the photo-transformations of salicylideneaniline and arrived at a photo-chemical scenario that starts with a fast adiabatic ESIPT followed by a diabatic isomerization of the C8−C9 bond.[32] More recently, the mechanism was addressed through time-dependent density functional theory (TDDFT) and ab initio (CASPT2/CASSCF) calculations by Ortiz-Sánchez et al.[33] They identified another diabatic isomerization channel involving rotation around the N7═C8 bond and estimated the corresponding decay time (37.7 fs) using adiabatic quantum dynamics on a one-dimensional fitted energy profile. Ab initio electronic structure calculations at the HF and configuration interaction singles (CIS) levels were used by Zgierski and Grabowska[15] to study the ground state and the $^1n\pi^*$ and $^1\pi\pi^*$ excited states, respectively, as well as the $^1\pi\pi^* \rightarrow {}^1n\pi^*$ internal conversion process. They computed an ESIPT barrier of 7.2 kcal/mol (CIS) in the $^1\pi\pi^*$ state, whereas more recent TDDFT calculations found the ESIPT reaction to be barrierless.[33]

Previous static electronic structure calculations have provided valuable insights into the photoinduced processes of salicylideneaniline, but full-dimensional dynamics simulations remain desirable to shed light on mechanistic issues that cannot be captured by static computations, for example, the time scales of ultrafast photodynamical processes and the dynamical competition between different deactivation channels. This motivates the present theoretical study, which employs the semiempirical OM2/MRCI method (orthogonalization model 2 with multireference configuration interaction) in combination with trajectory surface-hopping simulations to explore the photodynamics of salicylideneaniline.

COMPUTATIONAL METHODS

All semiempirical calculations were performed using the OM2/MRCI method[34−37] as implemented in the MNDO99 code.[38] During geometry optimizations and dynamics simulations, all required energies, gradients, and nonadiabatic coupling elements were computed analytically. Minimum-energy conical intersections were optimized using the Lagrange−Newton approach.[39]

In the calculations on salicylideneaniline, the restricted open-shell HF formalism was applied in the self-consistent-field (SCF) treatment (i.e., the orbitals were optimized for the leading configuration of the S_1 state with two singly occupied orbitals). The active space in the MRCI calculations included 12 electrons in 12 orbitals (see Supporting Information, Figure 1). In terms of the SCF configuration, it comprised the five highest doubly occupied orbitals, the two singly occupied orbitals, and the five lowest unoccupied orbitals. For the MRCI treatment, three configuration state functions were chosen as references, namely the SCF configuration and the two closed-shell configurations derived therefrom (i.e., all singlet configurations that can be generated from the HOMO and LUMO of the closed-shell ground state). The MRCI wave function was built by allowing all single and double excitations from these three references.

The nonadiabatic dynamics was studied by performing 1 ps OM2/MRCI trajectory surface-hopping simulations.[40−42] The initial atomic coordinates and velocities were randomly selected from 2 ps trajectories of ground-state molecular dynamics. The number of excited-state dynamics runs was then chosen according to the computed $S_0 \rightarrow S_1$ transition probability. A total of 209 surface-hopping trajectories were run, with all relevant energies, gradients, and nonadiabatic coupling vectors being computed on-the-fly as needed. For points with an $S_1–S_0$ energy gap of less than 10 kcal/mol, the fewest-switches criterion was applied to decide whether to hop.[41] The time step was chosen to be 0.1 fs for the nuclear motion and 0.0005 fs for the electronic propagation. The unitary propagator evaluated at midpoint was used to propagate the electronic motion.[42,43] The translational and rotational motions were removed in each step. The empirical decoherence correction (0.1 au) proposed by Granucci et al. was employed.[44] The final evaluations were done for the 125 trajectories that finished successfully and satisfied our energy continuity criterion (no changes greater than 30 kcal/mol between any two consecutive molecular dynamics (MD) steps). Further technical details are given in our previous publications.[42,45]

The adopted semiempirical MRCI approach has been shown to perform well in a comprehensive general evaluation of excited-state properties[46] and in a number of recent excited-state studies.[45,47−57]

For further specific validation, we have performed DFT and TDDFT calculations using the Gaussian 09 program.[58] Ground-state geometry optimizations were done with the B3LYP functional[59−61] and the 6-31+G* basis set.[62] Vertical excitation energies were calculated at these structures using TDDFT with different modern functionals (CAM-B3LYP,[63] ωB97X-D,[64] M06-2X[65]) and the aug-cc-pVDZ basis set.[66]

ELECTRONIC STRUCTURE CALCULATIONS

Equilibrium Structures and Relative Energies in the S_0 State. We have optimized four stable salicylideneaniline conformers, namely the cis-enol form (S0-CIS-ENOL), the cis-keto form (S0-CIS-KETO), the trans-keto form (S0-TRA-KETO), and the trans-enol form (S0-TRA-ENOL). Their structures are schematically shown in Figure 2 with selected geometric parameters collected in Table 1. Relative energies are listed in Table 2 for OM2/MRCI and B3LYP/6-31+G* (evaluated at the corresponding optimized geometries).

In the S_0 state the most stable structure is S0-CIS-ENOL. In this species, there is a strong intramolecular hydrogen bond, N7···H16 (1.758 Å), making the six-membered N7−C8−C9−C14−O15−H16 moiety nearly planar. S0-CIS-ENOL contains a N7═C8 double bond (1.291 Å) and a C8−C9 single bond
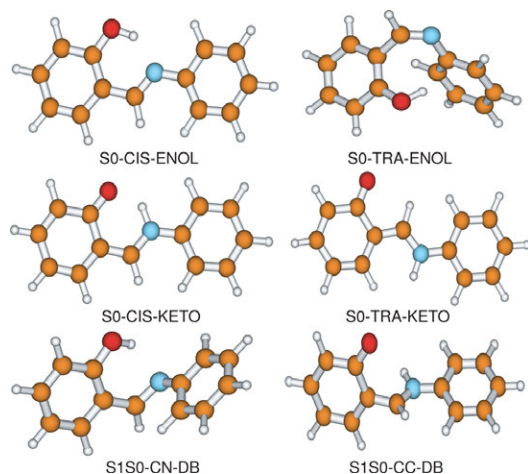
47

Figure 2. OM2/MRCI optimized structures (see text). The atomic numbering is defined in Figure 1. S1-CIS-KETO is not shown because it looks similar to S0-CIS-KETO.

(1.464 Å). This pattern is reversed when the H16 hydrogen is transferred from the O15 atom to the N7 atom, forming the cis-keto tautomer S0-CIS-KETO, with a N7−C8 single bond and a C8=C9 double bond. According to OM2/MRCI, S0-CIS-KETO lies 3.5 kcal/mol above S0-CIS-ENOL. The hydrogen transfer between S0-CIS-ENOL and S0-CIS-KETO is facile, with a barrier of 6.2 (2.6) kcal/mol in the forward (backward) direction. The trans conformers are somewhat higher in energy (S0-TRA-KETO 9.4 kcal/mol and S0-TRA-ENOL 12.7 kcal/mol relative to S0-CIS-ENOL), but S0-TRA-KETO is kinetically stable because the ground-state isomerization to S0-CIS-KETO involves double-bond rotation and requires considerable activation. These OM2/MRCI results are in good agreement with our present DFT (B3LYP/6-31+G*) results (see Table 1) and with previous DFT work.[33]

Electronic Structure of the cis-enol Form in the S_1 State. Using OM2/MRCI and TDDFT we have calculated the $S_0 \rightarrow S_1$ vertical excitation energies of S0-CIS-ENOL (see the Supporting Information, Table 2). OM2/MRCI performs as well as TDDFT with range-separated functionals (CAM-B3LYP, ωB97X-D) and with M06-2X, and approaches the CASPT2 prediction (within 0.3 eV for the cis-enol form and 0.1 eV for the cis-keto form). Furthermore, the gas-phase OM2/MRCI predictions are close to the experimental values obtained in various solvents.

Table 2. Relative Energies (kcal/mol)

	OM2/MRCI	B3LYP/6-31+G*
S0-CIS-ENOL	0.0	0.0
S0-CIS-KETO	3.5	3.4
S0-TRA-KETO	9.4	13.8
S0-TRA-ENOL	12.7	11.0
S0-TS-HT	6.2	6.2
S0-TS-KETO-ISOM	51.9	43.9
S1-CIS-KETO	63.0	
S1S0-CN-DB	62.6	
S1S0-CC-DB	55.2	

In the Franck−Condon region, the $S_0 \rightarrow S_1$ transition mainly consists of a $\pi \rightarrow \pi^*$ excitation from the highest occupied molecular orbital (HOMO) to the lowest unoccupied molecular orbital (LUMO) of the closed-shell configuration (coefficients: 0.83, OM2/MRCI; 0.69, TDDFT/B3LYP). Both the HOMO and LUMO are delocalized over the whole molecule (Figure 3); hence the transition is not associated with
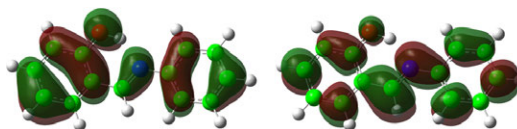

Figure 3. Isosurface of (left) HOMO and (right) LUMO for S0-CIS-ENOL at isovalue 0.02.

any significant charge transfer (as also indicated by the computed dipole moments: S_0, 2.52 D; S_1, 2.45 D). There is a nodal plane between C8 and C9 in the HOMO and between N7 and C8 in the LUMO. The excitation from S_0 to S_1 will thus weaken the N7=C8 bond and strengthen the C8−C9 bond. The S_1 state is a bright state with an oscillator strength of 0.359 (TDDFT/B3LYP) for the $S_0 \rightarrow S_1$ transition.

Electronic Structure of the cis-keto Form in the S_1 State. There is no stable minimum of cis-enol type in the S_1 state. All S_1 energy minimizations starting from the Franck−Condon cis-enol region quickly evolve to the cis-keto region by ESIPT, which implies that there is a barrierless downhill path for this conversion on the S_1 potential energy surface. This topological feature has also been noted in the previous PM3, CIS, and TDDFT calculations.[15,33] At the OM2/MRCI level, there is an energy plateau on the S_1 surface with essentially planar cis-keto structures. We have been able to locate a shallow minimum (S1-CIS-KETO) in this region by an unconstrained optimization, with a well depth of around 2 kcal/mol against out-of-plane motion toward a conical

Table 1. Selected Bond Lengths (Å) and Dihedral Angles (deg) in the OM2/MRCI Optimized Structures[a]

	N7C8	C8C9	N7H16	C14O15	O15H16	ϕ_1	ϕ_2	ϕ_3
S0-CIS-ENOL	1.291	1.464	1.758	1.340	1.007	0.0	180.0	0.0
S0-CIS-KETO	1.340	1.401	1.048	1.256	1.649	0.0	180.0	0.0
S0-TRA-KETO	1.353	1.393	1.020	1.244	4.661	0.0	180.0	180.0
S0-TRA-ENOL	1.278	1.480	2.517	1.354	0.996	42.8	−1.7	51.0
S1-CIS-KETO	1.340	1.467	1.059	1.268	1.594	0.0	180.0	0.0
S1S0-CN-DB	1.376	1.431	1.966	1.363	0.994	5.5	92.8	5.9
S1S0-CC-DB	1.353	1.462	1.018	1.249	3.373	17.4	169.7	−84.8

[a]Notation for dihedral angles: ϕ_1, C1C6N7C8; ϕ_2, C6N7C8C9; ϕ_3, N7C8C9C14.

intersection (see the Supporting Information, Figure 2). S1-CIS-KETO is calculated to be 27 kcal/mol below the cis-enol Franck–Condon geometry on the S_1 surface. We note for comparison that previous TDDFT calculations could locate an S_1 cis-keto minimum structure only when imposing planarity.[33]

The overall topological features of the HOMO and LUMO at the optimized S0-CIS-KETO geometry (Figure 4) look
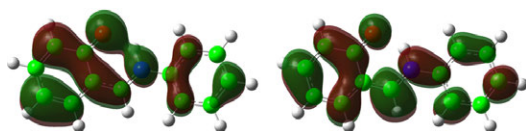

Figure 4. Isosurface of (left) HOMO and (right) LUMO for S0-CIS-KETO at isovalue 0.02.

similar to those at the S0-CIS-ENOL geometry (Figure 3), but there are also some differences. In particular, the C8–C9 bond shows π antibonding (bonding) character in the HOMO (LUMO) of the cis-enol form, and the opposite character in the cis-keto form.

S_1/S_0 Minimum-Energy Conical Intersections. At the OM2/MRCI level, we have located two minimum-energy S_1/S_0 conical intersections that involve N7=C8 and C8–C9 torsions and that are labeled as S1S0-CN-DB and S1S0-CC-DB, respectively. In both structures, the corresponding π bond is fully broken, one of the two states is a biradical, and the other one has charge-transfer character, being mainly composed of a HOMO → LUMO single excitation. The relevant orbitals are illustrated in Figures 5 and 6, respectively.
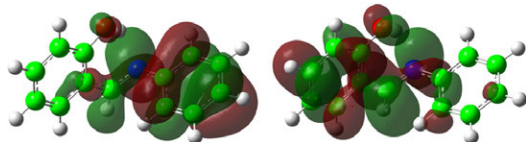

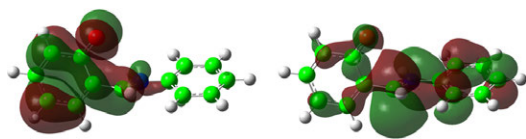**Figure 5.** Isosurface of (left) HOMO and (right) LUMO for S1S0-CN-DB at isovalue 0.02.

Figure 6. Isosurface of (left) HOMO and (right) LUMO for S1S0-CC-DB at isovalue 0.02.

Both conical intersections are energetically accessible considering the total energy available in the Franck–Condon region (OM2/MRCI: vertical $S_0 \rightarrow S_1$ excitation energy of 90.1 kcal/mol). At the OM2/MRCI level, S1S0-CN-DB and S1S0-CC-DB are computed to lie 27.5 and 34.9 kcal/mol below the S_1 Franck–Condon point. At the TDDFT level, the corresponding energy differences are reported to be 32.8 and 27.8 kcal/mol at geometries in the vicinity of the conical intersections (with a residual gap of about 3 kcal/mol between the two states).[33] One might assume on the basis of these relative energies that both conical intersections can be reached

in the OM2/MRCI excited-state dynamics, presumably with a preference for the lower-energy one (S1S0-CC-DB).

NONADIABATIC DYNAMICS SIMULATIONS

S_1 Ultrafast Proton Transfer Suppresses C=N Isomerization. The excited-state proton transfer in salicylideneaniline is ultrafast. In all our 125 trajectories, this process is finished within several tens of femtoseconds. This is consistent with recent experimental measurements: Peon and co-workers reported a value of 50 fs for the excited-state proton transfer time.[19] In addition, they did not observe a hydrogen/deuterium isotope effect and thus concluded that the S_1 potential energy surface is downhill from the Franck–Condon region toward the cis-keto minimum. This is in line with our finding (see above) that OM2/MRCI geometry optimizations starting from the S_1 cis-enol Franck–Condon region invariably move toward planar cis-keto species, indicative of a barrierless relaxation on the S_1 potential energy surface.

We have not seen the N7=C8 double bond isomerization in the S_1 state in any of our dynamic trajectories. This contrasts with previous theoretical predictions based on TDDFT calculations and one-dimensional quantum wavepacket simulations, which suggested N7=C8 isomerization and ESIPT to be competitive processes in the deactivation of the S_1 cis-enol conformer.[33] We note in this context that static electronic structure calculations and one-dimensional model simulations neglect the dynamic interplay between competitive decay channels (for example, isomerization and ESIPT) and may thus fail to give the correct mechanistic scenario. While this is true in general, it is still desirable to understand in a qualitative manner the outcome of our surface hopping trajectory calculations in the specific case of salicylideneaniline.

So, how do we rationalize the surprising finding that the N7=C8 double bond isomerization does not happen in the S_1 state in our simulations? The S_0 cis-enol tautomer (S0-CIS-ENOL) has a nearly planar structure with a strong N7···H16–O15 hydrogen bond, and hence, its motion in the ground state will mainly sample geometries that remain close to planar (with rather small skeletal deformations). In the present study, the initial conditions for the S_1 nonadiabatic dynamics were prepared from S_0 MD simulations. These will tend to favor parts of the phase space that are spanned mostly by the in-plane coordinates (positions and momenta). Consequently, the out-of-plane vibrational modes will be scarcely sampled, and there will thus be not much initial velocity in these modes, including the one for the C6–N7=C8–C9 torsion. After photo-excitation into the S_1 state, out-of-plane motions have to compete against the ESIPT process, which is so fast that the N7=C8 double bond isomerization channel is completely suppressed. Activating this channel would require breaking the strong N7···H16–O15 hydrogen bond very quickly (within tens of femtoseconds, the time scale of ESIPT). According to our simulations, this does not happen: in the S_1 state, the ESIPT process is too fast to allow the molecule to accumulate sufficient out-of-plane momentum to open up the N7=C8 double bond isomerization channel. This preference arises from the strong N7···H16–O15 hydrogen-bonding interaction that tends to maintain an almost planar conformation, which is beneficial for ESIPT and detrimental for N7=C8 double bond isomerization.

This phenomenon has also been observed in our study on a variant of the green fluorescent protein (GFP) chromophore.[53] In the ortho-substituted variant, there is a strong intramolecular
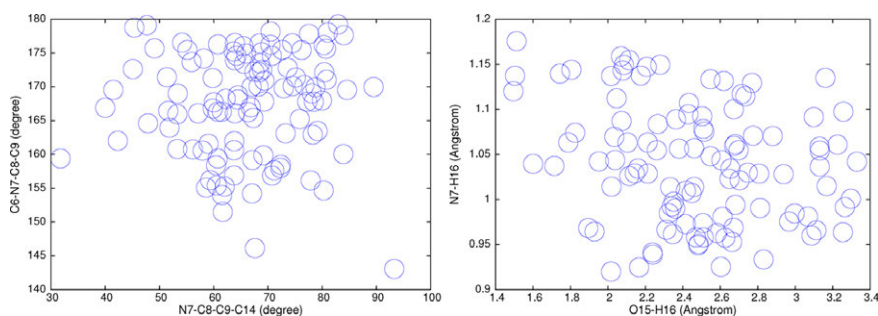
49

Article

Figure 7. Distribution of key geometric parameters at the $S_1 \rightarrow S_0$ hopping points. Values at the associated conical intersection S1S0-CC-DB: C6−N7−C8−C9, 169.7°; N7−C8−C9−C14, 84.8°; N7−H16, 1.018 Å (see Table 1).
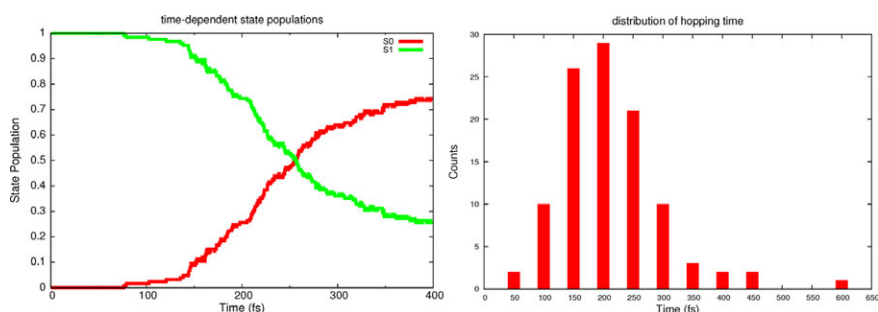

Figure 8. Time-dependent state populations and distribution of hopping times.

hydrogen-bonding interaction, different from the naturally occurring para-substituted chromophore (without intramolecular hydrogen bonding). In this GFP variant, the ultrafast excited-state proton transfer also occurs within a few tens of femtoseconds and completely suppresses the double bond isomerization decay channel, which explains the experimental finding that the original cis conformation is retained with a quantum yield of more than 95%.[53]

C−C Rotation Deactivates the S_1 State. The ultrafast ESIPT process in the S_1 state leads to cis-keto structures (S1-CIS-KETO). As already noted, the S1-CIS-KETO region has a rather flat energy landscape, with a shallow minimum that lies above the S_1/S_0 minimum-energy conical intersection S1S0-CC-DB (Table 1). The latter can be reached through an almost barrierless out-of-plane N7−C8−C9−C14 torsional motion (see the Supporting Information, Figure 2), as already discussed in previous TDDFT work.[33]

In all trajectories, the $S_1 \rightarrow S_0$ hopping points are structurally similar to the minimum-energy S_1/S_0 conical intersection S1S0-CC-DB (see Table 1). This is illustrated in Figure 7 showing the distribution of key geometric parameters at the hopping points. The C6−N7−C8−C9 and N7−C8−C9−C14 dihedral angles (see Figure 7, left) assume values around 165 and 60°, respectively, while the N7−H16 and O15−H16 distances (see Figure 7, right) clearly indicate the presence of a covalent NH bond (typically values of 1.0−1.1 Å) and a hydrogen-bonding interaction between O15 and H16 (typically values of 2.0−2.6 Å). It is thus obvious that all $S_1 \rightarrow S_0$ hopping events take place after the excited-state proton transfer from O15 to N7, emphasizing again that the ESIPT process is faster than N7═C8 double bond isomerization. The $S_1 \rightarrow S_0$ internal

conversion involves rotation around the C8−C9 bond, with partial retention of the N7−H16···O15 hydrogen bonding that is present in the cis-keto form. In our previous study on an ortho-substituted GFP chromophore, we also found that such intramolecular hydrogen bonding is capable of guiding the excited-state dynamics toward a particular channel.[53]

S_1 Excited-State Lifetime. The time-dependent S_1 state population $p(t)$ is shown in the left panel of Figure 8. Its exponential decay can be expressed in terms of the lifetime τ, the delay time τ_c for the initial excited-state proton transfer during which the system does not decay to the ground state, and the residual S_1 state population p_0 at the end of the simulation after 1 ps:

$$p(t) = e^{-t/(\tau - \tau_c)} + p_0 \qquad (1)$$

A fit of the data to eq 1 yields an excited-state lifetime of 295 fs, a delay time of 79 fs, and a residual population of 0.22. The right panel of Figure 8 shows the time distribution of the $S_1 \rightarrow S_0$ hopping events. Most of the trajectories decay to the ground state after 150−250 fs.

The present simulations for salicylideneaniline were done in the gas phase. In the condensed phase, the viscosity of the surroundings should affect the S_1 excited-state lifetime significantly. The main decay channel involves C8−C9 single bond rotation (see above) that demands a large conformational change, and it is thus reasonable to expect that the more rigid the surrounding, the more difficult it will be for the system to reach the S_1/S_0 conical intersection S1S0-CC-DB.

Bifurcation Processes in the S_0 State. An analysis of the branching vector near S1S0-CC-DB shows that the dynamics bifurcates at this S_1/S_0 conical intersection. One branch returns

to the cis-enol conformer via the cis-keto intermediate, while the other one directly leads to the trans-keto conformer.

Reverse Hydrogen Transfer. After the $S_1 \rightarrow S_0$ internal conversion around S1S0-CC-DB, many trajectories have instantaneous momenta that point toward the cis-keto conformer S0-CIS-KETO and thus immediately relax to the cis-keto region. Since the barrier to keto−enol tautomerization is small in the S_0 ground state (ca. 2 kcal/mol at the OM2/MRCI level), the system finally ends up in the cis-enol region, with the H16 atom transferred back to the O15 atom. Analogous ground-state reverse hydrogen transfers have been observed in our recent simulations of an ortho-substituted GFP chromophore[53] and a truncated indigo model.[56] In both cases, this process is essentially barrierless and thus ultrafast in vacuo. It is also found in other chemical and biological systems, e.g., in adenine−thymine and cytosine−guanine base pairs[67−69] and in *o*-phthalaldehyde.[70]

Direct Conversion to the trans-keto Conformer. The remaining trajectories head toward the trans-keto region. In these species, the N7−C8 bond is of single-bond character, so rotational motion around this bond is facile and is frequently observed in our trajectories. Since the ground-state barrier for cis/trans isomerization of the keto form involves rotation around the C8=C9 double bond and therefore requires considerable activation (more than 30 kcal/mol), the trans-keto isomer is expected to be long-lived and able to dissipate its excess energy. S0-TRA-KETO will thus be an observable photoproduct.

Product Distribution. The 1 ps simulations generate three ground-state species, namely the cis-enol, cis-keto, and trans-keto forms of salicylideneaniline. The corresponding yields can be seen from the distribution of the characteristic N7−H16 and O15−H16 distances (Figure 9) and the N7−C8−C9−C14
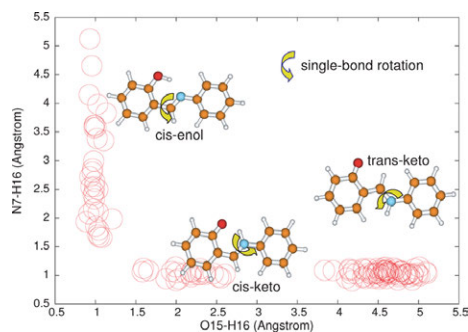
Figure 9. Distribution of N7H16 and O15H16 distances at the end of the 1 ps simulation.

dihedral angle (Figure 10). At the end of the 1 ps simulations, more than half of trajectories cluster around the trans-keto form (S0-TRA-KETO), with the remainder being split rather evenly between the cis-enol and cis-keto forms (S0-CIS-ENOL and S0-CIS-KETO). As already discussed, the latter will all end up in the most stable cis-enol minimum (S0-CIS-ENOL). A closer analysis of the outcome of the current 125 trajectories suggests a branching of roughly 45% S0-CIS-ENOL and 55% S0-TRA-KETO (see the Supporting Information, section 5).

Two Typical Trajectories. Figure 11 presents a typical trajectory, in which the system eventually returns to the starting cis-enol conformer (S0-CIS-ENOL). Upon excitation to the S_1
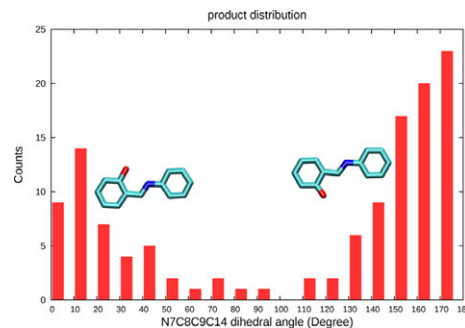
Figure 10. Distribution of N7C8C9C14 dihedral angles at the end of the 1 ps simulation.

state, the H16 proton initially attached to the O15 atom rapidly moves to the N7 atom within 20 fs (see Figure 11, bottom), thus forming the cis-keto form (S1-CIS-KETO). The system then wanders around the cis-keto region until it decays to the S_0 state after 260 fs. At this point, the N7−C8−C9−C14 and C6−N7−C8−C9 dihedral angles (see Figure 11, top) are close to 60 and 180°, respectively, indicating that the C8−C9 single bond rotation plays a crucial role in deactivating the S_1 state of salicylideneaniline (rather than the isomerization of the original N7=C8 double bond that remains essentially planar). Upon arrival in the S_0 state, the molecule immediately returns to the cis-keto region and remains there for ca. 300 fs. Thereafter, the H16 atom moves back from N7 to O15 (see Figure 11, bottom, near 600 fs) thus regenerating the cis-enol form S0-CIS-ENOL.

Figure 12 shows another typical trajectory, in which the system directly evolves toward the trans-keto conformer, after the $S_1 \rightarrow S_0$ internal conversion via S1S0-CC-DB. In this case, the H16 proton is transferred to the N7 atom after 50 fs. The molecule then spends about 300 fs in the cis-keto region (S1-CIS-KETO) until it decays to the S_0 state after 350 fs. Here the out-of-plane N7−C8−C9−C14 torsional mode still has enough momentum to carry the system directly into the trans-keto region (see the increase in the N7−C8−C9−C14 dihedral angle, Figure 12, top left). Thereafter, the molecule is trapped in the trans-keto region (S0-TRA-KETO) and does not manage to escape in the course of the 1 ps simulation.

■ RELATION TO PREVIOUS WORK

All our dynamics trajectories start with an initial ultrafast excited-state proton transfer, without any evidence for N7=C8 double bond isomerization. This initial relaxation mode is consistent with the available experiments.[12−14,16,20,21,23,32,71−74] The excited-state proton transfer is generally completed within a few tens of femtoseconds in our simulations, in good agreement with recent measurements.[11,17,19]

The origin of this ultrafast process is the potential energy surface topology of the $S_1(\pi\pi^*)$ state obtained from OM2/MRCI: Starting from the cis-enol Franck−Condon region, the excited molecule can quickly relax upon geometry optimization to the cis-keto region on an apparently barrierless downhill path. In typical trajectories, this proton transfer is finished within 1−2 vibrational periods of the O15−H16 stretching mode (see Figures 11 and 12). We note that some of the previous electronic structure calculations gave a small barrier for this ESIPT process: 7.2 kcal/mol at the CIS/6-31G* level (reduced to 3.2 kcal/mol in single-point TD-B3LYP/6-31G*
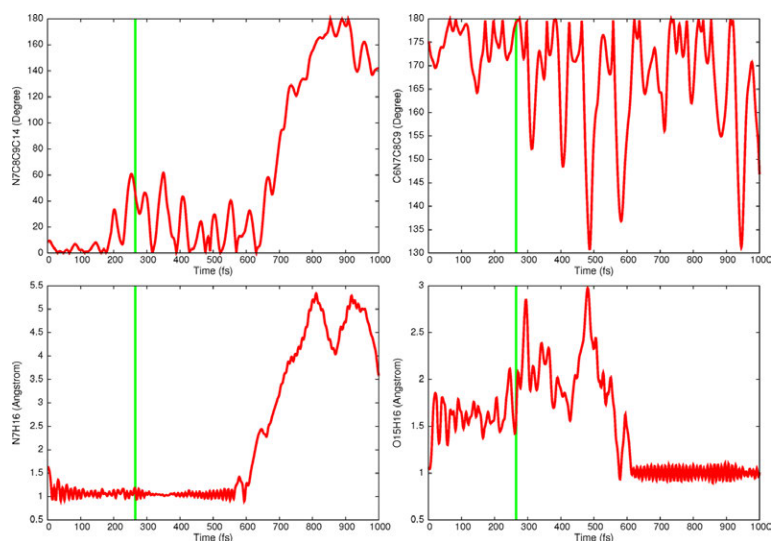
51

Figure 11. Typical trajectory for the photocycle of the cis-enol form. The green line in each panel marks the $S_1 \rightarrow S_0$ hopping event.
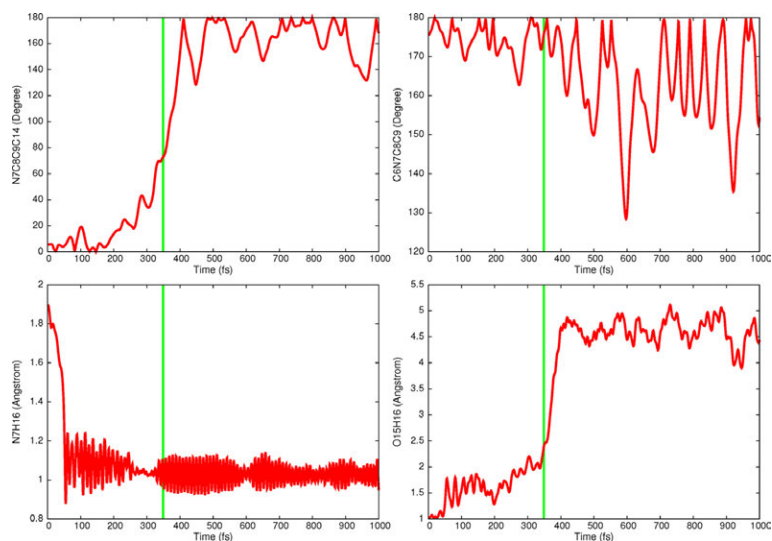

Figure 12. Typical trajectory for photoconversion to the trans-keto form. The green line in each panel marks the $S_1 \rightarrow S_0$ hopping event.

calculations)[15] and 0.4 kcal/mol at the PM3 level.[32] By contrast, the most recent explorations of the S_1 potential surface using TD-B3LYP with an augmented 6-31G** basis suggest a barrierless ESIPT process,[33] in agreement with our current OM2/MRCI results.

The recent work by Sliwa et al.[11] reported two competing ultrafast processes in salicylideneaniline (within 100 fs), namely excited-state proton transfer and excited-state enol rotation. In our dynamics simulations, we only see the ESIPT process although we note that the proton transfer is accompanied by some fluctuations of the C6−N7−C8−C9 dihedral angle (see Figures 11 and 12), which is considered to be the dominant reaction coordinate for excited-state enol rotation.[11,33] Excited-

state torsion along this coordinate bond would lead to the conical intersection S1S0-CN-DB (see Table 1 and Figure 2), but this deactivation path to the ground state is not followed in the present full-dimensional dynamics.

The cis-keto tautomer is the species responsible for fluorescence emission in salicylideneaniline.[74] Experimentally, an ultralow fluorescence quantum yield (0.001) was observed in a glassy solution at low temperature, along with an anomalous Stokes shift.[74] Importantly, the quantum yield could be increased significantly (to 0.044) by locking the N7=C8 and C8−C9 torsional modes of salicylideneaniline via chemical modifications.[74,75] The observed fluorescence quantum yield in the solid state is generally higher than that in

solution, indicating that the deactivation channel is heavily inhibited in the solid state but can be accessed in solution.[76] All these findings are consistent with our simulations that identify the sterically demanding isomerization around the C8−C9 single bond as the main deactivation channel during internal conversion.

Our results confirm the generally accepted notion that the trans-keto tautomer is the photocolored product generated by irradiation of salicylideneaniline. The most direct evidence for this assignment comes from the X-ray study of a derivative by Harada et al.[24] Already in an early photochemical kinetics study, Barbara et al. proposed that the vibrationally hot, excited cis-keto tautomer serves as precursor to the trans-keto photochromic product.[21] In their interpretation of submicro-second time-resolved infrared spectra of the transient photo-chromic species in acetonitrile, Yuzawa et al. described the trans-keto tautomer as a resonance hybrid between a quinoid structure and a zwitterionic structure, and they suggested that the relative contribution of these two structures should depend on solvent polarity.[23]

The present results from static OM2/MRCI calculations generally agree well with those from high-level (TDDFT, CASPT2) electronic structure calculations by Ortiz-Sánchez et al.[33] This holds for the optimized geometries (see Table 1), the relative energies of ground-state species (see Table 2), and the vertical excitation energies (see the Supporting Information, Table 2). Likewise, both S_1/S_0 minimum-energy conical intersections share the same characteristic geometric features in OM2/MRCI as well as in TDDFT and CASSCF/CASPT2.[33] Making use of the coordinates deposited as Supporting Information in the previous paper,[33] we obtain the following values for the key dihedral angles C1−C6−N7−C8 and N7−C8−C9−C14: 175 and −92° in S1S0-CC-DB, and 92 and 6° in S1S0-CN-DB, respectively. These values are very close to the OM2/MRCI results, typically within 5° (see Table 1). Obviously, OM2/MRCI and the first-principles methods predict the same types of conical intersections, involving C8−C9 single bond torsion for S1S0-CC-DB and N7=C8 double bond torsion for S1S0-CN-DB.

Concerning the dynamics, Ortiz-Sánchez et al. considered the two corresponding deactivation channels, namely double bond isomerization around N7=C8 in the cis-enol form (called IC1 channel) and around the C8−C9 single bond in the cis-keto form obtained by ESIPT (called IC2 channel).[33] They predicted an ultrafast time scale (37.7 fs) for the IC1 channel, using a quantum dynamics treatment based on a fitted one-dimensional energy profile, which neglects all other degrees of freedom and their interplay. They did not study the dynamics of the IC2 channel because they judged the limitations of one-dimensional treatments as being too severe for this process. We find in our full-dimensional treatment that the IC1 channel is completely suppressed by the ultrafast excited-state proton transfer and is therefore not accessed in any of our trajectories. As already discussed, this seems qualitatively reasonable: the (essentially barrierless) in-plane proton transfer is dynamically favored and so fast (1−2 vibrational periods of the O15−H16 stretching mode) that there is no time for out-of-plane vibrational modes to accumulate the sufficient momentum: the proton transfer has finished before the double bond isomerization can start to take effect.

Finally, we comment on the role of the $^1n\pi^*$ excited state in the photodynamics of salicylideneaniline. Zgierski and Grabowska[15] suggested the $^1\pi\pi^* \rightarrow {}^1n\pi^*$ internal conversion

as the second ultrafast relaxation channel. Since our simulations give an ultrafast excited-state proton transfer (within tens of femtoseconds), it seems highly unlikely that the $^1n\pi^*$ state plays an important role in the cis-enol form. By contrast, the $^1\pi\pi^* \rightarrow {}^1n\pi^*$ internal conversion could become more relevant for the cis-keto form in a rigid environment, especially in the crystalline state, which may impede the deactivation via the C8−C9 single bond rotation and thus increase the lifetime of the $S_1(\pi\pi^*)$ state.

■ CONCLUSIONS

We have used trajectory surface-hopping dynamics to simulate ultrafast photoinduced processes of salicylideneaniline in the gas phase. Mechanistically we find (see Figure 13) that
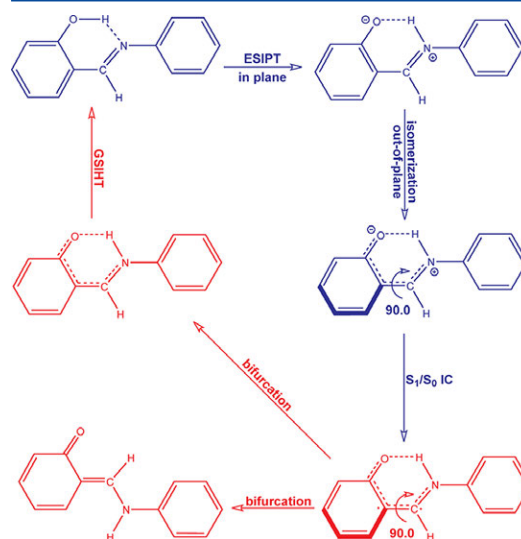

Figure 13. Major photoinduced processes observed in nonadiabatic dynamics simulations (IC, internal conversion; GSIHT, ground-state intramolecular hydrogen transfer).

photoexcitation of the most stable cis-enol conformer to the bright S_1 state triggers an ultrafast proton transfer that completely suppresses the alternative isomerization around the C=N double bond. The internal conversion of the resulting S_1 cis-keto species is initiated by an out-of-plane motion around the C−C single bond, which guides the molecule toward a conical intersection that provides an efficient deactivation channel to the ground state. After the internal conversion, the trajectories bifurcate in the ground state, either via the cis-keto to the cis-enol form or directly to the trans-keto form of salicylideneaniline. The knowledge about the dominant relaxation pathway in the gas phase enables us to discuss possible environmental effects in a qualitative manner, for example with regard to fluorescence quenching and photo-coloration in the condensed phase, where the internal conversion via the C−C single bond rotation is expected to be slowed down. In line with previous work, we assign the S_1 cis-keto conformer as the species responsible for fluorescence, especially in rigid surroundings. The S_0 cis-keto species is a transient photoproduct, while the S_0 trans-keto photoproduct is stable and responsible for the experimentally observed

53

photochromism. According to our simulations, the S_0 cis-enol and trans-keto photoproducts should be formed in roughly equal amounts in the gas phase.

On the methodological side, the present study demonstrates the merits of full-dimensional dynamics simulations. At face value, both S_1/S_0 conical intersections are accessible energetically, and both have been considered in previous work as possible deactivation channels. The surface-hopping trajectory calculations reveal, however, that only one of them is dynamically relevant. Unlike static or low-dimensional dynamics treatments, the full-dimensional dynamics simulations thus allow us to arrive at a comprehensive mechanistic scenario that includes the interplay among different competing channels.

■ ASSOCIATED CONTENT

Ⓢ Supporting Information

Active space used in OM2/MRCI calculations, OM2/MRCI and B3LYP relative energies, OM2/MRCI excited-state energy profile, OM2/MRCI and TDDFT vertical excitation energies, time evolution of key geometric parameters during the OM2/MRCI trajectory surface-hopping simulations, and Cartesian coordinates of all optimized structures. This material is available free of charge via the Internet at http://pubs.acs.org.

■ AUTHOR INFORMATION

Corresponding Author

*E-mail: ganglong@mpi-muelheim.mpg.de (G.C.); thiel@mpi-muelheim.mpg.de (W.T.).

Notes

The authors declare no competing financial interest.

■ REFERENCES

(1) Yokoyama, Y. Fulgides for Memories and Switches. *Chem. Rev.* **2000**, *100*, 1717−1740.

(2) Irie, M. Diarylethenes for Memories and Switches. *Chem. Rev.* **2000**, *100*, 1685−1716.

(3) Berkovic, G.; Krongauz, V.; Weiss, V. Spiropyrans and Spirooxazines for Memories and Switches. *Chem. Rev.* **2000**, *100*, 1741−1754.

(4) Tian, H.; Yang, S. Recent Progresses on Diarylethene Based Photochromic Switches. *Chem. Soc. Rev.* **2004**, *33*, 85−97.

(5) Beharry, A.; Woolley, G. Azobenzene Photoswitches for Biomolecules. *Chem. Soc. Rev.* **2011**, *40*, 4422−4437.

(6) Feringa, B.; van Delden, R.; Koumura, N.; Geertsema, E. Chiroptical Molecular Switches. *Chem. Rev* **2000**, *100*, 1789−1816.

(7) Feringa, B.; Browne, W. *Molecular Switches*; Wiley-VCH: Weinheim, Germany, 2011.

(8) Kawata, S.; Kawata, Y. Three-Dimensional Optical Data Storage Using Photochromic Materials. *Chem. Rev.* **2000**, *100*, 1777−1788.

(9) Wuttig, M.; Yamada, N. Phase-Change Materials for Rewriteable Data Storage. *Nat. Mater.* **2007**, *6*, 824−832.

(10) Raymo, F.; Giordani, S. All-Optical Processing with Molecular Switches. *Proc. Natl. Acad. Sci. U.S.A.* **2002**, *99*, 4941−4944.

(11) Sliwa, M.; Mouton, N.; Ruckebusch, C.; Poisson, L.; Idrissi, A.; Alose, S.; Potier, L.; Dubois, J.; Poizat, O.; Buntinx, G. Investigation of Ultrafast Photoinduced Processes for Salicylidene Aniline in Solution and Gas Phase: Toward a General Photo-Dynamical Scheme. *Photochem. Photobiol. Sci.* **2010**, *9*, 661−669.

(12) Mitra, S.; Tamai, N. Femtosecond Spectroscopic Study on Photochromic Salicylideneaniline. *Chem. Phys. Lett.* **1998**, *282*, 391−397.

(13) Okabe, C.; Nakabayashi, T.; Inokuchi, Y.; Nishi, N.; Sekiya, H. Ultrafast Excited-State Dynamics in Photochromic N-Salicylideneaniline Studied by Femtosecond Time-Resolved REMPI Spectroscopy. *J. Chem. Phys.* **2004**, *121*, 9436−9442.

(14) Otsubo, N.; Okabe, C.; Mori, H.; Sakota, K.; Amimoto, K.; Kawato, T.; Sekiya, H. Excited-State Intramolecular Proton Transfer in Photochromic Jet-Cooled Salicylideneaniline. *J. Photochem. Photobiol., A* **2002**, *154*, 33−39.

(15) Zgierski, M.; Grabowska, A. Photochromism of Salicylideneaniline (SA). How the Photochromic Transient Is Created: A Theoretical Approach. *J. Chem. Phys.* **2000**, *112*, 6329−6337.

(16) Mitra, S.; Tamai, N. Dynamics of Photochromism in Salicylideneaniline: A Femtosecond Spectroscopic Study. *Phys. Chem. Chem. Phys.* **2003**, *5*, 4647−4652.

(17) Ziółek, M.; Kubicki, J.; Maciejewski, A.; Naskrecki, R.; Grabowska, A. An Ultrafast Excited State Intramolecular Proton Transfer (ESPIT) and Photochromism of Salicylideneaniline (SA) and Its "Double" Analogue Salicylaldehyde Azine (SAA). A Controversial Case. *Phys. Chem. Chem. Phys.* **2004**, *6*, 4682−4689.

(18) Ziółek, M.; Kubicki, J.; Maciejewski, A.; Naskrecki, R.; Grabowska, A. Excited State Proton Transfer and Photochromism of an Aromatic Schiff Base. Pico- and Femtosecond Kinetics of the N,N′-Bis(salicylidene)-p-phenylenediamine (BSP). *Chem. Phys. Lett.* **2003**, *369*, 80−89.

(19) Rodríguez-Córdoba, W.; Zugazagoitia, J.; Collado-Fregoso, E.; Peon, J. Excited State Intramolecular Proton Transfer in Schiff Bases. Decay of the Locally Excited Enol State Observed by Femtosecond Resolved Fluorescence. *J. Phys. Chem. A* **2007**, *111*, 6241−6247.

(20) Cohen, M.; Schmidt, G. Photochromy and Thermochromy of Anils. *J. Phys. Chem.* **1962**, *66*, 2442−2446.

(21) Barbara, P.; Rentzepis, P.; Brus, L. Photochemical Kinetics of Salicylideneaniline. *J. Am. Chem. Soc.* **1980**, *102*, 2786−2791.

(22) Becker, R.; Lenoble, C.; Zein, A. A Comprehensive Investigation of the Photophysics and Photochemistry of Salicylideneaniline and Derivatives of Phenylbenzothiazole Including Solvent Effects. *J. Phys. Chem.* **1987**, *91*, 3509−3517.

(23) Yuzawa, T.; Takahashi, H.; Hamaguchi, H. Submicrosecond Time-Resolved Infrared Study on the Structure of the Photoinduced Transient Species of Salicylideneaniline in Acetonitrile. *Chem. Phys. Lett.* **1993**, *202*, 221−226.

(24) Harada, J.; Uekusa, H.; Ohashi, Y. X-ray Analysis of Structural Changes in Photochromic Salicylideneaniline Crystals. Solid-State Reaction Induced by Two-Photon Excitation. *J. Am. Chem. Soc.* **1999**, *121*, 5809−5810.

(25) Zhang, Y.; Zhao, C.; Fang, W.; You, X. A Molecular Design View on the First Hyperpolarizability of Salicylideneaniline Derivatives. *Theor. Chem. Acc.* **1997**, *96*, 129−134.

(26) Enchev, V.; Ugrinov, A.; Neykov, G. Intramolecular Proton Transfer Reactions in Internally Hydrogen-Bonded Schiff Bases: Ab Initio and Semiempirical Study. *J. Mol. Struct.* **2000**, *530*, 223−235.

(27) Becker, R.; Lenoble, C.; Zein, A. Photophysics and Photochemistry of the Nitro Derivatives of Salicylideneaniline and 2-(2′-Hydroxyphenyl)benzothiazole and Solvent Effects. *J. Phys. Chem.* **1987**, *91*, 3517−3524.

(28) Alarcón, S.; Pagani, D.; Bacigalupo, J.; Olivieri, A. Spectroscopic and Semi-Empirical MO Study of Substituent Effects on the Intramolecular Proton Transfer in Anils of 2-Hydroxybenzaldehydes. *J. Mol. Struct.* **1999**, *475*, 233−240.

(29) Fang, W.; You, X.; Yin, Z. Theoretical Studies on the Photochromic Processes of 4-Bromo-N-salicylideneaniline. *Theor. Chem. Acc.* **1995**, *92*, 297−303.

(30) Fang, W.; Zhang, Y.; You, X. Theoretical Studies on the Mechanisms of Proton Transfer in Schiff Bases. *J. Mol. Struct.* **1995**, *334*, 81−89.

(31) Tinland, B. A Semiempirical LCAO MO SCF Study of the Electronic Structure of Photochromic Anils with a Variable β Approximation. *Tetrahedron* **1970**, *26*, 4795−4798.

(32) Kletskii, M.; Millov, A.; Metelitsa, A.; Knyazhansky, M. Role of Structural Flexibility in the Fluorescence and Photochromism of Salicylideneaniline: The General Scheme of the Phototransformations. *J. Photochem. Photobiol., A* **1997**, *110*, 267−270.

(33) Ortiz-Sánchez, J.; Gelabert, R.; Moreno, M.; Lluch, J. M. Electronic-Structure and Quantum Dynamical Study of the Photo-

chromism of the Aromatic Schiff Base Salicylideneaniline. *J. Chem. Phys.* **2008**, *129*, 214308.

(34) Weber, W. Ph.D. Thesis, University of Zürich, 1996

(35) Weber, W.; Thiel, W. Orthogonalization Corrections for Semiempirical Methods. *Theor. Chem. Acc.* **2000**, *103*, 495−506.

(36) Otte, N.; Scholten, M.; Thiel, W. Looking at Self-Consistent-Charge Density Functional Tight Binding from a Semiempirical Perspective. *J. Phys. Chem. A* **2007**, *111*, 5751−5755.

(37) Koslowski, A.; Beck, M.; Thiel, W. Implementation of a General Multireference Configuration Interaction Procedure with Analytic Gradients in a Semiempirical Context Using the Graphical Unitary Group Approach. *J. Comput. Chem.* **2003**, *24*, 714−726.

(38) Thiel, W. *MNDO99 Program*, version 6.1; Max-Planck-Institut für Kohlenforschung: Mülheim, Germany, 2007.

(39) Keal, T.; Koslowski, A.; Thiel, W. Comparison of Algorithms for Conical Intersection Optimization Using Semiempirical Methods. *Theor. Chem. Acc.* **2007**, *118*, 837−844.

(40) Tully, J.; Preston, R. Trajectory Surface Hopping Approach to Nonadiabatic Molecular Collisions: Reaction of H with D_2. *J. Chem. Phys.* **1971**, *55*, 562−572.

(41) Hammes-Schiffer, S.; Tully, J. Proton Transfer in Solution: Molecular Dynamics with Quantum Transitions. *J. Chem. Phys.* **1994**, *101*, 4657−4667.

(42) Fabiano, E.; Keal, T.; Thiel, W. Implementation of Surface Hopping Molecular Dynamics Using Semiempirical Methods. *Chem. Phys.* **2008**, *349*, 334−347.

(43) Keal, T.; Wanko, M.; Thiel, W. Assessment of Semiempirical Methods for the Photoisomerisation of a Protonated Schiff Base. *Theor. Chem. Acc.* **2009**, *123*, 145−156.

(44) Granucci, G.; Persico, M.; Zoccante, A. Including Quantum Decoherence in Surface Hopping. *J. Chem. Phys.* **2010**, *133*, 134111.

(45) Fabiano, E.; Thiel, W. Nonradiative Deexcitation Dynamics of 9H-adenine: An OM2 Surface Hopping Study. *J. Phys. Chem. A* **2008**, *112*, 6859−6863.

(46) Silva-Junior, M.; Thiel, W. Benchmark of Electronically Excited States for Semiempirical Methods: MNDO, AM1, PM3, OM1, OM2, OM3, INDO/S, and INDO/S2. *J. Chem. Theory Comput.* **2010**, *6*, 1546−1564.

(47) Lan, Z.; Fabiano, E.; Thiel, W. Photoinduced Nonadiabatic Dynamics of Pyrimidine Nucleobases: On-the-Fly Surface-Hopping Study with Semiempirical Methods. *J. Phys. Chem. B* **2009**, *113*, 3548−3555.

(48) Lan, Z. G.; Fabiano, E.; Thiel, W. Photoinduced Nonadiabatic Dynamics of 9H-Guanine. *ChemPhysChem* **2009**, *10*, 1225−1229.

(49) Lan, Z.; Lu, Y.; Fabiano, E.; Thiel, W. QM/MM Nonadiabatic Decay Dynamics of 9H-Adenine in Aqueous Solution. *ChemPhysChem* **2011**, *12*, 1989−1998.

(50) Lu, Y.; Lan, Z.; Thiel, W. Hydrogen Bonding Regulates the Monomeric Nonradiative Decay of Adenine in DNA Strands. *Angew. Chem., Int. Ed.* **2011**, *50*, 6864−6867.

(51) Weingart, O.; Lan, Z.; Koslowski, A.; Thiel, W. Chiral Pathways and Periodic Decay in cis-Azobenzene Photodynamics. *J. Phys. Chem. Lett.* **2011**, *2*, 1506−1509.

(52) Kazaryan, A.; Lan, Z.; Schäfer, L.; Thiel, W.; Filatov, M. Surface Hopping Excited-State Dynamics Study of the Photoisomerization of a Light-Driven Fluorene Molecular Rotary Motor. *J. Chem. Theory Comput.* **2011**, *7*, 2189−2199.

(53) Cui, G.; Thiel, W. Intramolecular Hydrogen Bonding Plays a Crucial Role in the Photophysics and Photochemistry of the GFP Chromophore. *J. Am. Chem. Soc.* **2012**, *134*, 1662−1672.

(54) Lan, Z.; Lu, Y.; Weingart, O.; Thiel, W. Nonadiabatic Decay Dynamics of a Benzylidene Malononitrile. *J. Phys. Chem. A* **2012**, *116*, 1510−1518.

(55) Lu, Y.; Lan, Z.; Thiel, W. Monomeric adenine decay dynamics influenced by the DNA environment. *J. Comput. Chem.* **2012**, *33*, 1225−1235.

(56) Cui, G.; Thiel, W. Nonadiabatic Dynamics of a Truncated Indigo Model. *Phys. Chem. Chem. Phys.* **2012**, *14*, 12378−12384.

(57) Cui, G.; Thiel, W. Photoinduced Ultrafast Wolff Rearrangement: A Non-Adiabatic Dynamics Perspective. *Angew. Chem., Int. Ed.* **2013**, *52*, 433−436.

(58) Frisch, M. J.; Trucks, G. W.; Schlegel, H. B.; Scuseria, G. E.; Robb, M. A.; Cheeseman, J. R.; Scalmani, G.; Barone, V.; Mennucci, B.; Petersson, G. A.; et al. *Gaussian 09*, revision B.01; Gaussian, Inc.: Wallingford, CT, 2010.

(59) Becke, A. Density-Functional Exchange-Energy Approximation with Correct Asymptotic Behavior. *Phys. Rev. A* **1988**, *38*, 3098−3100.

(60) Lee, C.; Yang, W.; Parr, R. Development of the Colle-Salvetti Correlation-Energy Formula into a Functional of the Electron Density. *Phys. Rev. B* **1988**, *37*, 785−789.

(61) Becke, A. A New Mixing of Hartree-Fock and Local Density-Functional Theories. *J. Chem. Phys.* **1993**, *98*, 1372−1377.

(62) Ditchfield, R.; Hehre, W.; Pople, J. Self-Consistent Molecular-Orbital Methods. IX. An Extended Gaussian-Type Basis for Molecular-Orbital Studies of Organic Molecules. *J. Chem. Phys.* **1971**, *54*, 724−728.

(63) Yanai, T.; Tew, D.; Handy, N. A New Hybrid Exchange-Correlation Functional Using the Coulomb-Attenuated Method CAM-B3LYP. *Chem. Phys. Lett.* **2004**, *393*, 51−57.

(64) Chai, J. D.; Head-Gordon, M. Systematic Optimization of Long-Range Corrected Hybrid Density Functionals. *J. Chem. Phys.* **2008**, *128*, 084106.

(65) Zhao, Y.; Truhlar, D. The M06 Suite of Density Functionals for Main Group Thermochemistry, Thermochemical Kinetics, Non-covalent Interactions, Excited States, And Transition Elements: Two New Functionals and Systematic Testing of Four M06-Class Functionals and 12 Other Functionals. *Theor. Chem. Acc.* **2008**, *120*, 215−241.

(66) Dunning, T. H., Jr. Gaussian Basis Sets for Use in Correlated Molecular Calculations. I. The Atoms Boron through Neon and Hydrogen. *J. Chem. Phys.* **1989**, *90*, 1007−1023.

(67) Perun, S.; Sobolewski, A.; Domcke, W. Role of Electron-Driven Proton-Transfer Processes in the Excited-State Deactivation of the Adenine-Thymine Base Pair. *J. Phys. Chem. A* **2006**, *110*, 9031−9038.

(68) Sobolewski, A.; Domcke, W. Ab Initio Studies on the Photophysics of the Guanine-Cytosine Base Pair. *Phys. Chem. Chem. Phys.* **2004**, *6*, 2763−2771.

(69) Groenhof, G.; Schäfer, L.; Boggio-Pasqua, M.; Goette, M.; Grubmüller, H.; Robb, M. Ultrafast Deactivation of an Excited Cytosine-Guanine Base Pair in DNA. *J. Am. Chem. Soc.* **2007**, *129*, 6812−6819.

(70) Li, Q.; Migani, A.; Blancafort, L. Irreversible Phototautomerization of o-Phthalaldehyde through Electronic Relocation. *Phys. Chem. Chem. Phys.* **2012**, *14*, 6561−6568.

(71) Sekikawa, T.; Kobayashi, T.; Inabe, T. Femtosecond Fluorescence Study of the Substitution Effect on the Proton Transfer in Thermochromic Salicylideneaniline Crystals. *J. Phys. Chem. A* **1997**, *101*, 644−649.

(72) Kownacki, K.; Mordzinski, A.; Wilbrandt, R.; Grabowska, A. Laser-Induced Absorption and Fluorescence Studies of Photochromic Schiff Bases. *Chem. Phys. Lett.* **1994**, *227*, 270−276.

(73) Karpicz, R.; Gulbinas, V.; Lewanowicz, A.; Macernis, M.; Sulskus, J.; Valkunas, L. Relaxation Pathways of Excited *N*-(Triphenylmethyl)salicylideneimine in Solutions. *J. Phys. Chem. A* **2011**, *115*, 1861−1868.

(74) Knyazhansky, M.; Metelitsa, A.; Bushkov, A.; Aldoshin, S. Role of Structural Flexibility in Fluorescence and Photochromism of the Salicylideneaniline: The "Aldehyde" Ring Rotation. *J. Photochem. Photobiol., A* **1996**, *97*, 121−126.

(75) Knyazhansky, M.; Metelitsa, A.; Kletskii, M.; Millov, A.; Besugliy, S. The Structural Transformations and Photo-Induced Processes in Salicylidene Alkylimines. *J. Mol. Struct.* **2000**, *526*, 65−79.

(76) Sliwa, M.; Mouton, N.; Ruckebusch, C.; Alose, S.; Poizat, O.; Buntinx, G.; Metivier, R.; Nakatani, K.; Masuhara, H.; Asahi, T. Comparative Investigation of Ultrafast Photoinduced Processes in Salicylidene-Aminopyridine in Solution and Solid State. *J. Phys. Chem. C* **2009**, *113*, 11959−11968.

55

Supporting Information: Photodynamics of Schiff Base Salicylideneaniline: Trajectory Surface-Hopping Simulations

Lasse Spörkel, Ganglong Cui,* and Walter Thiel*

Max-Planck-Institut für Kohlenforschung, Kaiser-Wilhelm-Platz 1, 45470 Mülheim an der Ruhr,

Germany

E-mail: ganglong@mpi-muelheim.mpg.de; thiel@mpi-muelheim.mpg.de

Table of Contents

*To whom correspondence should be addressed

1

1 OM2/MRCI Active Space

The active space in the MRCI calculations included 12 electrons in 12 orbitals. Figure 1 shows the active orbitals for the most stable ground-state conformer of salicylideneaniline (cis-enol form).
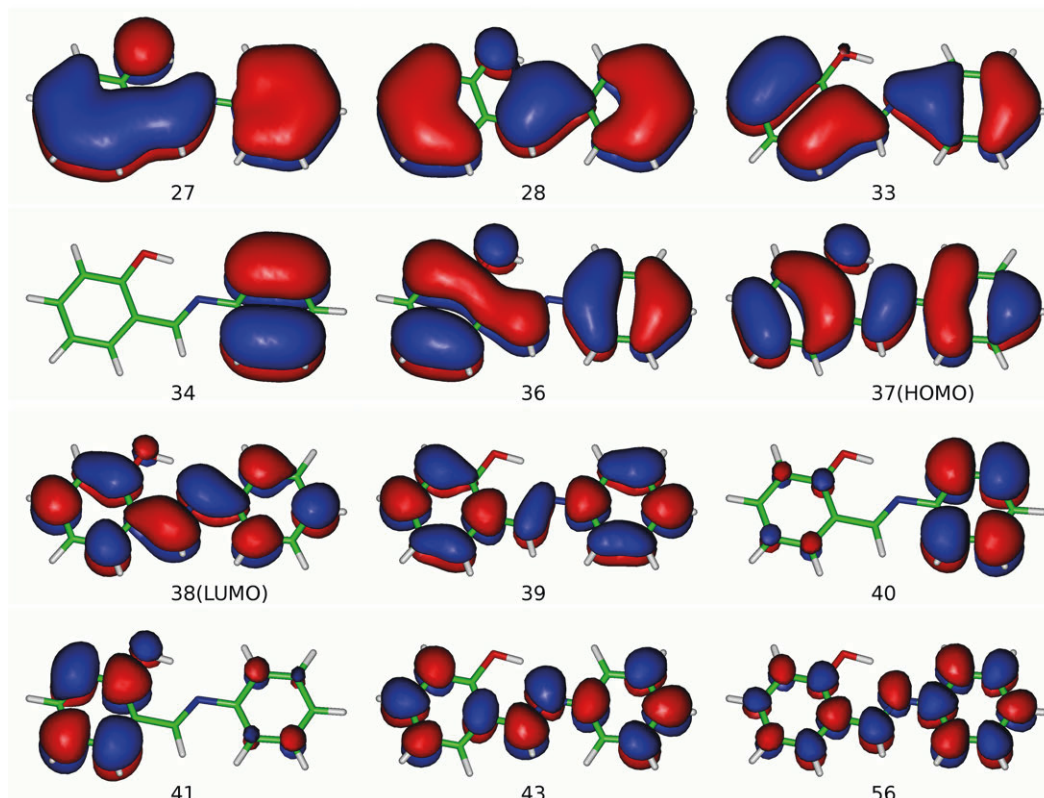

Figure 1: The active space (12e,12o) of salicylideneaniline (cis-enol form) used in the OM2/MRCI calculations. All orbitals are of π type. See text for simulation details.

In the closed-shell wavefunction of the planar ground state, the set of active orbitals consists of the 6 highest occupied π orbitals and the 6 lowest unoccupied π^* orbitals. During the simulations, an orbital tracking procedure[1] was applied to ensure that the active space remained intact also at non-planar geometries. Test calculations were done with an alternative choice of active orbitals, namely using the 6 highest occupied and 6 lowest unoccupied orbitals throughout (regardless of their character, selection solely based on energies). Static calculations with this alternative active

2

space gave results that are very similar to those reported here (data not shown), which is not too surprising since the most important orbitals are part of the active space in both cases.

2   Ground-State Potential Energy Profil

There are four relevant stable ground-state structures of salicylideneaniline (see Figure 2 of the main paper): the cis-enol form (S0-CIS-ENOL), the cis-keto form (S0-CIS-KETO), the trans-keto form (S0-TRA-KETO), and the twisted trans-enol form (S0-TRA-ENOL). S0-CIS-ENOL and S0-CIS-KETO can be interconverted by hydrogen transfer (via the transition state S0-TS-HT). The re-arrangement between S0-CIS-KETO and S0-TRA-KETO requires rotation around the C8=C9 double bond (via S0-TS-KETO-ISOM). The geometries of these species have been optimized at the OM2/MRCI level (see Table 1 of the main paper) and at the B3LYP/6-31+G* level. The optimized Cartesian coordinates are given in sections 6 and 7 (see below). The relative energies are listed in Table 1.

Both at the OM2/MRCI and B3LYP/6-31+G* levels, the cis-enol form is the most stable structure followed by the cis-keto form (3–4 kcal/mol higher in energy). The two trans-conformers are less favorable, with energies of 11–13 kcal/mol (S0-TRA-ENOL) and 9–14 kcal/mol (S0-TRA-KETO) relative to the cis-enol form. The conversion of the cis-keto form to the cis-enol minimum is facile, with a barrier of 2–3 kcal/mol, while the trans-keto isomer has to surmount a large barrier of more than 30 kcal/mol to reach the region of the cis-keto isomer. The OM2/MRCI and B3LYP/6-31+G* relative energies agree well with each other (Table 1).

The OM2/MRCI nonadiabatic dynamics simulations show ultrafast $S_1 \rightarrow S_0$ internal conversion. After 1 ps three ground-state species are found (see section 5 below), namely the cis-enol, cis-keto, and trans-keto forms. In view of the computed ground-state barriers, any cis-keto species will quickly evolve towards the most stable cis-enol minimum, while the trans-keto form is expected to be trapped and to constitute the second photoproduct.

3

Table 1: Relative Energies (kcal/mol) of Ground-State Conformers and Transition States

Structure	OM2/MRCI	B3LYP/6-31+G*
S0-CIS-ENOL	0.0	0.0
S0-CIS-KETO	3.5	3.4
S0-TRA-KETO	9.4	13.8
S0-TRA-ENOL	12.7	11.0
S0-TS-HT	6.2	6.2
S0-TS-KETO-ISOM	51.9	43.9

3 Excited-State Reaction Coordinate

The path from the shallow S1-CIS-KETO excited-state minimum towards the conical intersection S1S0-CC-DB was traced by varying the dihedral angle N7-C8-C9-C14 in steps of $0.9°$ and performing constrained geometry optimizations at each point using OM2/MRCI. The resulting energy profil is shown in Figure 2. The energy rises by about 2 kcal/mol before it drops again after a rotation of about $50°$.
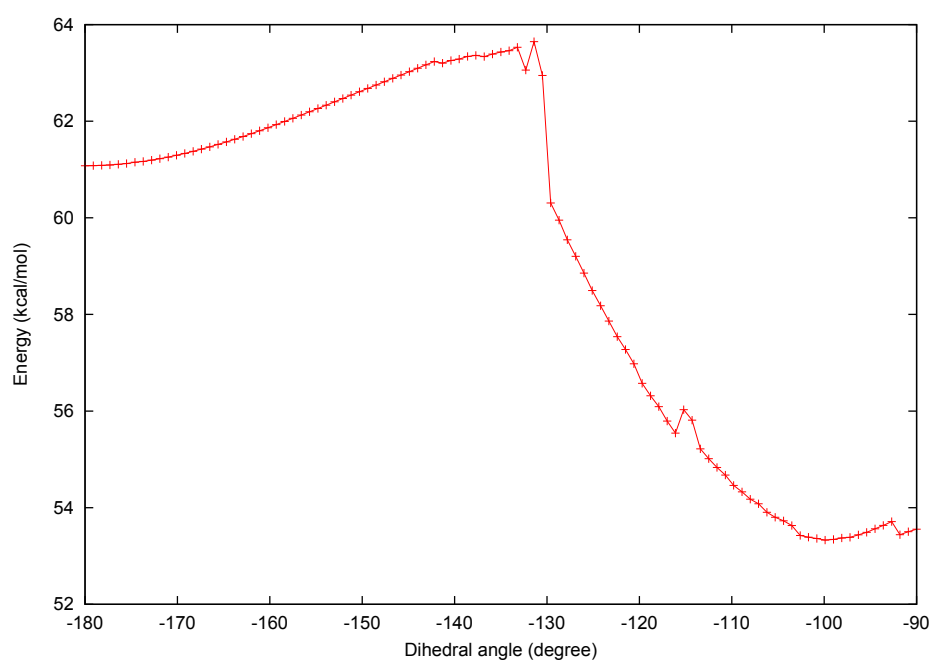

Figure 2: S_1 energy plotted against the dihedral angle N7-C8-C9-C10.

4

4   Vertical Excitation Energies

Theoretical and experimental $S_0 \rightarrow S_1$ vertical excitation energies of S0-CIS-ENOL and S0-CIS-KETO are presented in Table 2. The calculations were performed in the gas phase using OM2/MRCI and TDDFT (time-dependent density functional theory) at the corresponding ground-state geometries from OM2/MRCI and DFT(B3LYP), respectively (optimized coordinates see sections 6 and 7 below).

In the case of the cis-enol form, OM2/MRCI gives a vertical excitation energy of 3.91 eV. The TDDFT results are slightly lower (by 0.04–0.07 eV) for the M06-2X functional and the range-separated functionals (CAM-B3LYP, wB97X-D), and considerably more so for the B3LYP hybrid functional (by 0.40 eV). Also somewhat lower are the previously published TDDFT and CASPT2 values (3.63–3.75 eV) and the published experimental results obtained in solution (3.54–3.69 eV).

For the cis-keto form, the OM2/MRCI vertical excitation energy (2.90 eV) is slightly lower than the currently computed TDDFT values (2.95–3.18 eV). It lies in the range of the published TDDFT and CASPT2 values (2.79–3.26 eV), but above the experimental results in solution (2.60–2.62 eV). The firs absorption of the cis-keto form is strongly red-shifted compared with the cis-enol form. OM2/MRCI predicts the corresponding shift in the vertical excitation energies to be 1.01 eV, which is close to the experimental data in solution (1.06–1.09 eV). This shift is underestimated by the current TDDFT calculations (0.56–0.69 eV) and by the published TDDFT and CASPT2 results (0.49–0.84 eV). Overall the OM2/MRCI performance appears to be quite satisfactory for the excitation energies.

5   Time Evolution of Key Geometric Parameters

Figure 3 illustrates the variation of the N7-C8-C9-C14 and C6-N7-C8-C9 dihedral angles during the simulations. The N7-C8-C9-C14 dihedral angle is indicative of cis and trans conformations at the C8-C9 bond. It starts out around $0°$ (cis-enol), reaches ca. $60°$ at the hopping points, and ends up in a very broad distribution covering both cis and trans conformers, with the latter being somewhat more frequent (see left side). The C6-N7-C8-C9 dihedral angle reflect the configu ation around

5

Table 2: Theoretical and Experimental $S_0 \rightarrow S_1$ Vertical Excitation Energies (eV)

Reference	cis-enol	cis-keto
OM2/MRCI	3.91	2.90
TDDFT(B3LYP)/6-31+G*	3.51	2.95
TDDFT(CAM-B3LYP)/aug-cc-pVDZ	3.84	3.16
TDDFT(wB97XD)/aug-cc-pVDZ	3.87	3.18
TDDFT(M062X)/aug-cc-pVDZ	3.86	3.12
TDDFT(B3LYP)/6-31G* [Zgierski, 2000[2]]	3.75	3.26
TDDFT(B3LYP)/6-31+G** [Ortiz-Sánchez, 2008[3]]	3.66	2.82
CASPT2(10,10)/cc-pVDZ [Ortiz-Sánchez, 2008[3]]	3.63	2.79
Exp. (in methylcyclohexane) [Barbara, 1980[4]]	3.59	
Exp. (in acetonitrile) [Kownacki, 1994[5]]	3.69	2.60
Exp. (in acetonitrile) [Ziolek, 2004[6]]	3.68	2.62
Exp. (in acetonitrile) [Sliwa, 2010[7]]	3.54	

the N7=C8 double bond. It always remains around 180° during the whole simulation (see right side), thus clearly indicating that N7=C8 double bond isomerization does not play any role in the dynamics.

Figure 4 shows the distributions of the N7-H16 and O15-H16 distances in all trajectories. It is obvious from these plots that the $S_0 \rightarrow S_0$ internal conversion happens after the ultrafast excited-state proton transfer. At the starting geometries (top), the O15-H16 and N7-H16 distances cluster around 1.0 and 2.0 Å, respectively (cis-enol form with an O15-H16 covalent bond and an N7...H16 hydrogen bond). At the hopping points (middle), the H16 atom has in all trajectories been transferred to the N7 atom: the $S_1 \rightarrow S_0$ internal conversion thus occurs in the keto form that contains an N7-H16 bond (ca. 1.0 Å), with a broad distribution of O15-H16 distances that reflect the out-of-plane twist around the C8-C9 bond (see Figure 3). At the end points (bottom), three products can be identified the cis-enol form with the H16 atom transferred back to the O15 atom as well as the cis-keto and trans-keto forms with an N7-H16 bond. Closer inspection of the bottom panel of Figure 4 shows that, after 1 ps, 32 of the 125 trajectories end up at an enol structure with an O15-H16 bond, while the remaining 93 trajectories are in the keto region with an N7-H16 bond. Among the latter, 69 have large O15-H16 distances of typically 4–5 Å (corresponding to the trans-keto form) and 24 have O15-H16 distances in the hydrogen bonding range around 2 Å (corresponding to the cis-keto
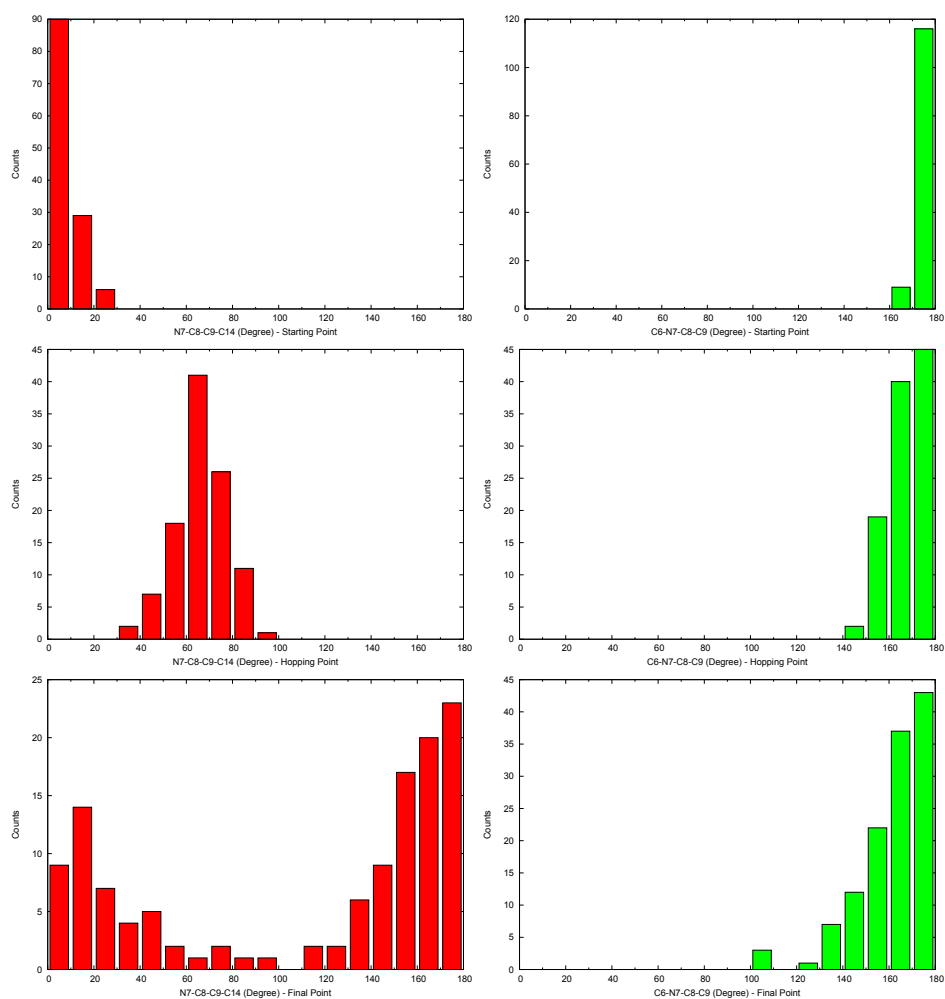
6

Figure 3: Distribution of key dihedral angles (degree) at the starting points (top), the hopping points (middle), and the end points (bottom).

7

form). Considering the ground-state energy barriers (see section 2 above), the cis-keto species will quickly rearrange to the most stable cis-enol minimum so that a total of 56 trajectories will yield the cis-enol photoproduct. The present simulations thus predict a branching ratio of 56:69 between the cis-enol and trans-keto photoproducts, i.e. about 45% vs. 55%.
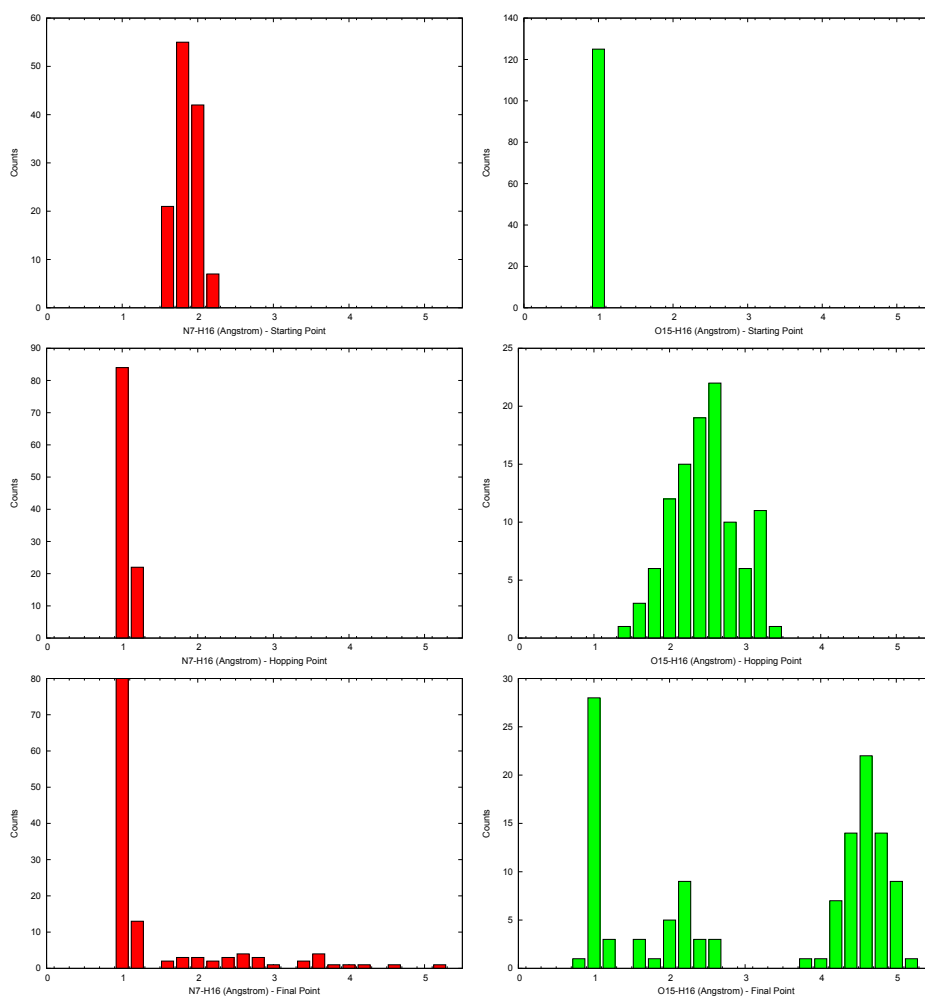

Figure 4: Distribution of key distances (Å) involving the mobile hydrogen for the starting points (top), the hopping points (middle) and the end points (bottom).

8

	S1S0-CN-DB		
C	1.77899	-2.20528	0.99616
C	1.81956	-3.29302	1.85342
C	0.70883	-3.66013	2.62611
C	-0.47577	-2.92301	2.54792
C	-0.52458	-1.83069	1.67276
C	0.59418	-1.42611	0.90297
H	2.65198	-1.91830	0.40048
H	2.74004	-3.88801	1.92888
H	0.75497	-4.54606	3.27108
H	-1.34639	-3.19445	3.13590
C	0.60700	-0.26443	0.06809
H	1.40114	-0.14719	-0.67585
O	-1.72756	-1.19105	1.64338
H	-1.76967	-0.58163	0.85921
C	-0.33064	1.67337	0.90323
C	0.82432	1.94107	1.69567
C	-1.44891	2.56165	0.97161
C	0.85080	3.05220	2.52100
H	1.67260	1.25486	1.65220
C	-1.39288	3.67519	1.79173
H	-2.33203	2.34224	0.36688
C	-0.25068	3.92168	2.56816
H	1.72587	3.25528	3.14451
H	-2.23985	4.36520	1.84081
H	-0.22058	4.80010	3.22424
N	-0.44570	0.62173	0.04395

	S1S0-CC-DB		
C	-0.13184	-2.82447	-0.65598
C	-0.98860	-3.92178	-0.72091
C	-2.14189	-3.99242	0.09265
C	-2.44225	-2.97358	0.96499
C	-1.58090	-1.81790	1.07628
C	-0.40220	-1.77776	0.22784
H	0.74438	-2.77149	-1.31072
H	-0.77624	-4.74623	-1.41098
H	-2.78394	-4.87804	0.02524
H	-3.33559	-3.00357	1.59013
C	0.52164	-0.65000	0.33168
H	1.23370	-0.63822	1.15533
O	-1.84437	-0.88622	1.86583
H	-0.59756	0.46616	-0.96114
C	0.90296	1.69675	-0.22987
C	2.15235	1.77789	0.41339
C	0.30369	2.84410	-0.79329
C	2.77747	3.01779	0.50050
H	2.63166	0.89022	0.84303
C	0.96008	4.06361	-0.69823
H	-0.66517	2.76695	-1.29642
C	2.19403	4.15981	-0.04933
H	3.74256	3.09269	1.00893
H	0.50252	4.96233	-1.12790
H	2.70170	5.14056	0.03833
N	0.23771	0.46539	-0.37937

References

(1) Keal, T. W.; Koslowski, A.; Thiel, W. *Theor. Chem. Acc.* **2007**, *118*, 837.

(2) Zgierski, M.; Grabowska, A. *J. Chem. Phys.* **2000**, *112*, 6329.

(3) Ortiz-Sánchez, J.; Gelabert, R.; Moreno, M.; Lluch, J. *J. Chem. Phys.* **2008**, *129*, 214308.

(4) Barbara, P.; Rentzepis, P.; Brus, L. *J. Am. Chem. Soc.* **1980**, *102*, 2786.

(5) Kownacki, K.; Mordzinski, A.; Wilbrandt, R.; Grabowska, A. *Chem. Phys. Lett.* **1994**, *227*, 270.

(6) Ziółek, M.; Kubicki, J.; Maciejewski, A.; Naskręcki, R.; Grabowska, A. *Phys. Chem. Chem. Phys.* **2004**, *6*, 4682.

(7) Sliwa, M.; Mouton, N.; Ruckebusch, C.; Poisson, L.; Idrissi, A.; Aloïse, S.; Potier, L.; Dubois, J.; Poizat, O.; Buntinx, G. *Photochem. Photobiol. Sci.* **2010**, *9*, 661.

13

B. Nonequilibrium H/D Isotope Effects from Trajectory-Based Nonadiabatic Dynamics

Lasse Spörkel, Ganglong Cui, Axel Koslowski and Walter Thiel

I carried out all OM2 calculations and performed the subsequent analysis. I wrote most parts of the manuscript. I created all included figures.

Nonequilibrium H/D Isotope Effects from Trajectory-Based Nonadiabatic Dynamics

Lasse Spörkel, Ganglong Cui,* Axel Koslowski, and Walter Thiel*

Max-Planck-Institut für Kohlenforschung, Kaiser-Wilhelm-Platz 1, 45470 Mülheim an der Ruhr, Germany

S *Supporting Information*

ABSTRACT: Ground-state equilibrium kinetic isotope effects can be treated well in the framework of transition state theory, whereas excited-state nonequilibrium isotope effects are theoretically less explored. In this article we show for the first time that trajectory-based nonadiabatic dynamics simulations are able to reproduce experimental values for nonequilibrium H/D isotope effects in excited-state processes. We use high-level electronic structure calculations (MS-CASPT2, DFT/MRCI, and TDDFT) and full-dimensional OM2/MRCI-based nonadiabatic dynamics simulations to study the ultrafast intramolecular excited-state proton transfer (ESIPT) and the subsequent deactivation of 7-(2-pyridyl)indole (7PyIn) and its deuterated analogue (7PyIn-D). We evaluate a total of 1367 surface-hopping trajectories to establish the differences in the dynamical behavior of 7PyIn and 7PyIn-D. The computed H/D isotope effects for ESIPT and excited-state decay are consistent with recent experimental results from femtosecond pump−probe resonance-enhanced multiphoton ionization spectroscopy. We also analyze the influence of temperature fluctuations in the initially prepared sample on the photodynamics of 7PyIn and 7PyIn-D.
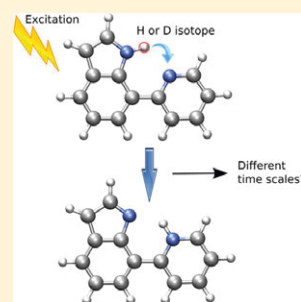
■ INTRODUCTION

Proton transfer is ubiquitous in chemical and biological systems and optoelectronic materials, including ion channels of membrane proteins,[1] green fluorescence proteins,[2] natural and synthesized water-oxidation centers,[3,4] light-emitting diodes,[5] and other systems.[6−10] In the past decades, kinetic H/D isotope effects have been measured in numerous experiments to elucidate the detailed mechanism of chemical reactions involving proton or hydrogen transfer. The influence of isotopic substitution on the reaction rate is normally evaluated in the framework of transition state theory.[11] However, such treatment is invalid for ultrafast nonequilibrium processes, e.g., an excited-state intramolecular proton transfer (ESIPT) on an essentially barrierless potential energy surface, because this process is already completed before arriving at its thermodynamic equilibrium. Quantum wavepacket dynamics can be used to simulate ESIPT processes[12] and to analyze excited-state nonequilibrium H/D isotope effects,[13] but such calculations are quite expensive and are thus, at the current stage, limited to model systems with a few degrees of freedom. This bottleneck can be overcome by full-dimensional trajectory-based surface-hopping simulations,[14−16] which have been widely applied in recent years[17−22] (for reviews see refs 23 and 24). However, to our knowledge, such dynamics simulations have not yet addressed excited-state nonequilibrium isotope effects.

In this article, we chose 7-(2-pyridyl)indole (7PyIn) as our target system to explore ESIPT-related nonequilibrium isotope effects. We use OM2/MRCI-based surface-hopping simulations for this purpose,[16] which have recently been applied successfully to study the excited-state dynamics of medium-sized organic molecules (see, for example, refs 2 and 25−31). Experimentally,[32] transient absorption (TA) spectra of 7PyIn in solution reveal that the initially excited species decays to the ground state in about 1.0 ps. Femtosecond pump−probe resonance-enhanced multiphoton ionization (REMPI) in a supersonic jet generates an immediate strong ion signal indicating an ultrafast depopulation of the initially generated S_1 species in the gas phase, which has been attributed to ESIPT coupled with a twisting motion, with time constants of 280 fs for 7PyIn and 390 fs for the deuterated analogue.[32] A second small ion signal in the REMPI spectra after about 1 ps has been tentatively associated with excited-state decay after one period of a torsional vibrational motion.[32] Previous electronic structure calculations have addressed the photochemical mechanism of 7PyIn in much detail,[33] but complementary dynamical insights remain desirable. Therefore, we report the first trajectory-based nonadiabatic dynamics simulations of the photodynamics of 7PyIn and 7PyIn-D. We demonstrate that trajectory-based dynamics simulations are capable of describing the experimentally observed nonequilibrium H/D isotope effects. Furthermore, we perform an initial-condition temperature-decomposition analysis to evaluate the influence of thermal fluctuations on the photoinduced processes. In the following, we summarize our main results; the computational methods and further detailed results are presented in the Supporting Information.

■ RESULTS AND DISCUSSION

At the B3LYP/6-31G* level, there are four ground-state minima for 7PyIn, which are referred to as S0-syn, S0-anti, S0-
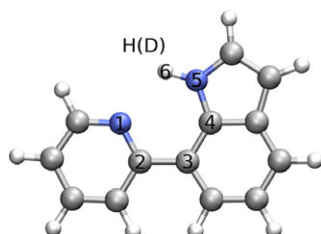

Figure 1. Molecules studied in this work: 7PyIn and its deuterated analogue 7PyIn-D. Color code: nitrogen atoms in blue, carbon atoms in gray, and hydrogen atoms in white. Also shown is the numbering scheme for some relevant atoms.

Table 1. Calculated $S_0 \rightarrow S_1$ Vertical Excitation Energies (eV)[a]

B3LYP[b]	CAM-B3LYP[b]	M062X[b]	OM2/MRCI[c]	DFT/MRCI[d]	MS-CASPT2[e]	RI-CC2[f]
3.59	4.06	4.08	4.19	3.95	4.34	4.0

[a]See the Supporting Information for methods and absorption spectrum; experimental spectra are available only in solution (band maximum around 3.8 eV). [b]B3LYP/6-31G* optimized structure, energies from single-point TD-DFT/6-31++G** calculations. [c]OM2/MRCI(12,12) energy at the corresponding optimized structure. [d]CASSCF(10,8)/6-31G* optimized structure, energy from single-point DFT/MRCI calculation (BHLYP/TZVP). [e]CASSCF(10,8)/6-31G* optimized structure, energy from single-point MS-CASPT2-(14,12)/cc-pVTZ calculation; note that single-point MS-CASPT2-(14,12)/6-31G*, MS-CASPT2(10,8)/6-31G*, and MS-CASPT2-(10,8)/cc-pVTZ calculations give values of 4.38, 4.69, and 4.48 eV, respectively. [f]Coupled cluster RI-CC2/cc-pVDZ result from Sobolewski and Domcke.[33]

syn-ht, and S0-anti-ht (Figure SI-1, Supporting Information). The most stable syn conformer (S0-syn, Figure 1) has C_s symmetry and a strong intramolecular hydrogen bond (N5−H6···N1). The anti conformer, S0-anti, is less stable by 5.9 kcal/mol, while the ground-state tautomers generated by transfer of H6 from N5 to N1 (S0-syn-ht and S0-anti-ht) are much higher in energy (Table SI-2, Supporting Information).

The vertical excitation energy to the first singlet excited state of the S0-syn conformer was computed with a variety of electronic structure methods (Table 1) including time-dependent density functional theory (TD-DFT using the B3LYP, CAM-B3LYP, and M06-2X exchange−correlation functionals), DFT-based multireference configuration interaction (DFT/MRCI), and multistate complete-active-space second-order perturbation theory (MS-CASPT2). Computation of the full absorption spectrum (Figure SI-3, Supporting Information) shows that the $S_0 \rightarrow S_1$ electronic transition gives rise to the strongest absorption band. The S_1 state is of partial charge-transfer character so that the conventional hybrid functional B3LYP underestimates its energy by ca. 0.5 eV, compared with range-separated (CAM-B3LYP) and modern (M06-2X) functionals. The latter give vertical excitation energies (4.06−4.08 eV) that are close to the values from DFT/MRCI (3.95 eV) and the coupled-cluster CC2 method (4.0 eV[33]), but lower than the OM2/MRCI result (4.37 eV) and the MS-CASPT2 results that range between 4.34 and 4.69 eV for different active spaces and basis sets (Table 1).

In the Franck−Condon (FC) region, we could locate a very shallow S_1 minimum for the syn conformer (S1-syn) at the OM2/MRCI and CASSCF(10,8) levels (Table SI-2, Supporting Information), with very small barriers to tautomerization via ESIPT (see below). This minimum was not obtained in previous RI-CC2/SV(P) calculations that predicted a barrierless ESIPT process.[33] Experimentally, the ESIPT is also believed to be essentially barrierless because lowering the temperature does not stop the ultrafast excited-state deactivation.[32] Our scans of the S_1 minimum-energy ESIPT reaction path (transfer of H6 from N5 to N1) indicate a barrier of 1.5 kcal/mol at the OM2/MRCI level (Figure 2), which is found to be insignificant in our OM2/MRCI dynamics simulations (see below). The CASSCF/6-31G* energy profiles look qualitatively similar, with a rather flat S_1 plateau in the early ESIPT stages (Figure 2). Single-point MS-CASPT2/6-31G* calculations at the CASSCF geometries yield an ESIPT barrier of 2.7 kcal/mol in the S_1 state (Figure SI-4, Supporting Information).

After the transfer of H6, the S_1 potential energy profile of the resulting tautomer is rather flat with regard to the N1−C2−C3−C4 dihedral angle in the whole range between 0° and 90° (Figure 2). This twist leads to the S_1/S_0 conical intersection region. We have optimized the minimum-energy S_1/S_0 conical intersection (MECI, labeled as S1S0-CI). Its N1−C2−C3−C4
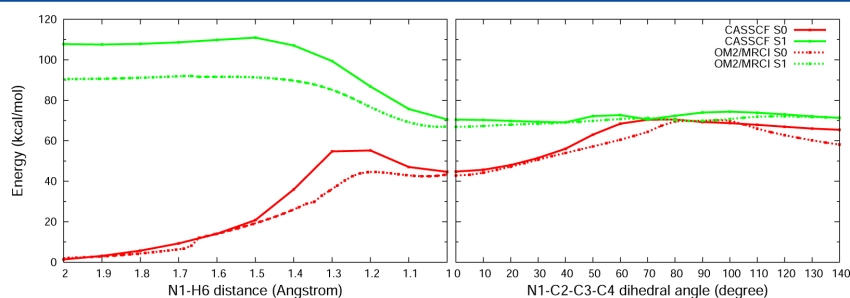

Figure 2. CASSCF/6-31G* and OM2/MRCI energy profiles for relaxed one-dimensional minimum-energy paths (MEPs) along the N1−H6 bond length (left) and the N1−C2−C3−C4 dihedral angle (right). The S_1 MEPs are fully optimized with respect to the other coordinates, and the S_0 curves are obtained from single-point calculations.
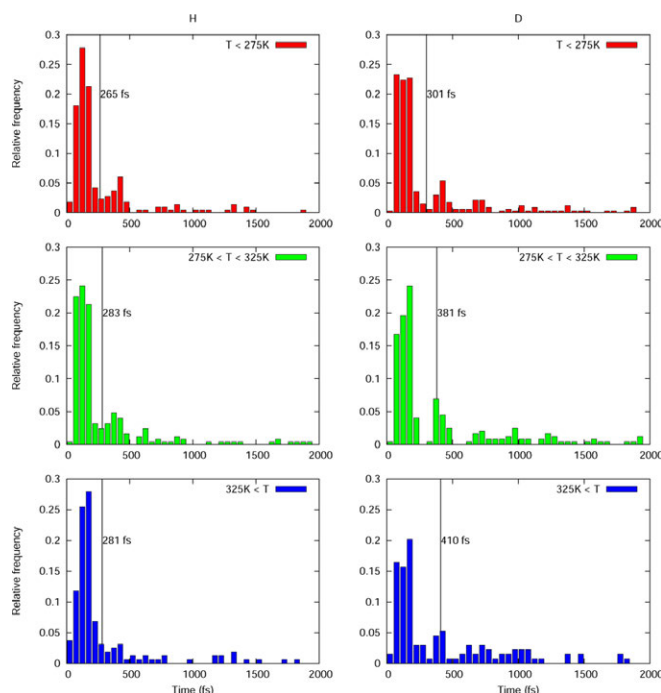
Figure 3. ESIPT time distributions in three temperature windows of initial conditions (top, less than 275 K; middle, between 275 and 325 K; bottom, greater than 325 K).

dihedral angle is computed to be 63.2° at the CASSCF(10,8)/6-31G* level, close to the recent CASSCF(6,6)/6-31G* optimized value of 72°,[34] but considerably smaller than the RI-CC2/SV(P) estimate of ca. 90°.[33] OM2/MRCI yields a rather extended and flat conical intersection region for N1−C2−C3−C4 dihedral angles between 50° and 90°, with an essentially perpendicular MECI (like RI-CC2, see the Supporting Information for further detailed information). Energetically, this conical intersection is easily accessed: the energy gap relative to the most stable S syn conformer is computed to be 3.37 eV at the MS-CASPT2 level and 3.35 eV at the OM2/MRCI level; these values are considerably lower than the corresponding S_1 vertical excitation energies of 4.69 and 4.37 eV at the FC point. The computed relaxed potential energy profiles (Figure 2) suggest that the dynamics from the FC region to S1S0−CI should be very fast (as confirmed by our OM2/MRCI simulations, see below). Single-point MS-CASPT2/6-31G* calculations at the CASSCF geometries also give a rather flat profile, but there remains a sizable S_0/S_1 energy gap in the MECI region because of the use of CASSCF geometries (Figure SI-4, Supporting Information).

To gain further insight into the dynamics, we performed extensive full-dimensional nonadiabatic surface-hopping simulations, with a total of 632 trajectories for 7PyIn and 735 for 7PyIn-D (2 ps each, see the Supporting Information for details of the simulations and their analysis). Our main focus is the nonequilibrium H/D isotope effect on the ultrafast ESIPT process of 7PyIn. We adopted the criterion to measure the ESIPT time in each trajectory at the point when the distance in the breaking N5−H6 bond exceeds 1.5 Å, which yields average

ESIPT times of 274 fs for 7PyIn and 339 fs for 7PyIn-D (see Figure SI-7 (Supporting Information) and the associated discussion). These values are consistent with the spectroscopically observed H/D isotope effect: As mentioned above, Nosenko et al.[32] attributed the first ion signal in pump−probe REMPI spectra to the ESIPT process and determined time constants of 280 fs for 7PyIn and 390 fs for 7PyIn-D in a supersonic jet (for depopulation of the initially excited species by ESIPT). Moreover, their second small ion signal at about 1.0 ps may correspond to the few ESIPT events observed in our simulations in this range, especially for 7PyIn-D (Figure 3). In spite of lacking nuclear quantum effects, trajectory-based dynamics simulations thus seem capable of capturing nonequilibrium H/D isotope effects, in particular for essentially barrierless ultrafast processes such as ESIPT.

We have further analyzed the influence of thermal fluctuations in the initially prepared ensemble on the ESIPT time distribution (Figure 3). Overall, the higher the temperature, the longer the ESIPT time. This can be understood in a qualitative manner. A higher temperature implies a higher kinetic energy, which is reflected in nuclear motions that sample distorted molecular geometries further away from the ground-state equilibrium structure. In the case of 7PyIn, the planar ground-state structure contains a nearly "perfect" hydrogen-bonding arrangement, which is ideally suited for ESIPT after vertical excitation. On the other hand, the ESIPT process will be less favorable (and thus take longer) when the vertical excitation occurs from distorted structures, especially those with strong out-of-plane displacements, which will be encountered more often at higher temperatures. In our
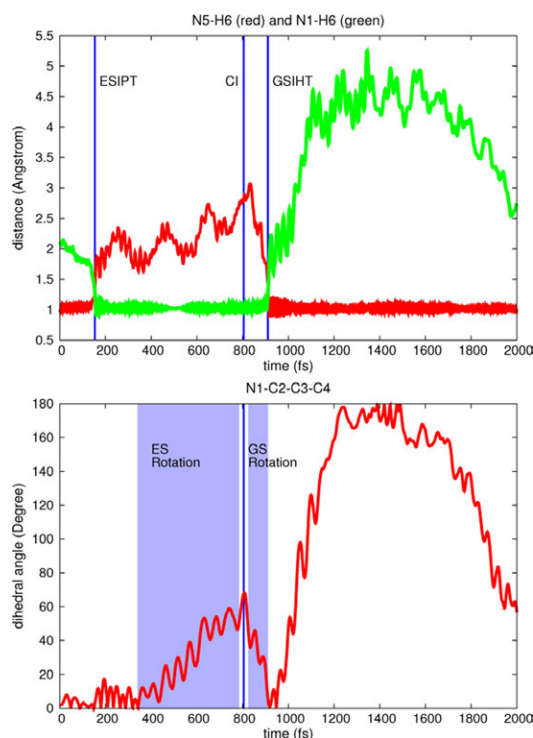
Figure 4. Typical trajectory for 7PyIn. The excited-state proton transfer is completed at 200 fs and after another 600 fs, the $S_1 \rightarrow S_0$ internal conversion takes place. In the S_0 state, the hydrogen atom is transferred back to the original donor atom. See text for more details.

simulations, this is reflected in average ESIPT times that increase with increasing temperature in the three chosen windows (7PyIn from 265 fs to 283 and 281 fs, 7PyIn-D from 301 fs to 381 and 410 fs).

The average hopping time in our trajectories is found to be 605 fs for 7PyIn and 669 fs for 7PyIn-D (Figure SI-8, Supporting Information), indicating that internal conversion occurs about 330 fs after completion of the ESIPT process. Both isotopologues thus take roughly the same time for the

twisting motion that is required to reach the conical intersection region. The computed gas-phase excited-state decay times and the measured gas-phase REMPI time constants are shorter than the excited-state decay time of about 1.0 ps deduced from the TA spectra in solution. Our simulations support the qualitative explanation given previously,[32] namely that the solvent environment may slow down the excited-state deactivation. Access to the S_1/S_0 conical intersection with an N1−C2−C3−C4 dihedral angle of ca. 90° (OM2/MRCI and CC2) requires a twist around the central C2−C3 bond, which will be harder to achieve in solution than in vacuo, because solute−solvent interactions will hinder the required out-of-plane motions.

To illustrate the photodynamics of 7PyIn and to highlight the main photochemical events, we discuss the time evolution of three key geometric parameters in a typical trajectory (Figure 4). In the first 180 fs after the vertical photoexcitation, the H6 atom remains bound to the N5 atom. During this period, the excited-state decay is impossible because of the very large S_1−S_0 energy gap (more than 80 kcal/mol) and the small S_1/S_0 nonadiabatic coupling. The ESIPT process after ca. 180 fs generates the planar S_1 syn-ht tautomer with an N1−H6···N5 hydrogen bond. After roaming around this planar conformation for about 200 fs, the N1−C2−C3−C4 dihedral angle starts to twist, and the molecule then decays to the ground state via the S_1/S_0 conical intersection at 800 fs. At this point, the nonadiabatic coupling is much larger (Figure SI-11, Supporting Information). After further 100 fs of roaming in the S_0 state, the H6 atom returns back to N5 forming the most stable S0-syn tautomer. Similar dynamical features are observed for the deuterated analogue, albeit with some time delay (see Figure SI-12 (Supporting Information) and the associated discussion).

CONCLUSIONS

To summarize, we have explored the photodynamics of 7PyIn and its deuterated analogue by means of high-level electronic structure calculations (MS-CASPT2, TDDFT, and DFT/MRCI) and extensive OM2/MRCI nonadiabatic dynamics simulations (1367 successful runs in total). The latter provide mechanistic insights complementary to those from previous electronic structure calculations. The proposed complete photochemical mechanism is shown in Figure 5. We have demonstrated for the first time that full-dimensional trajectory-based dynamics methods are capable of simulating the nonequilibrium H/D isotope effect quite well, in the favorable
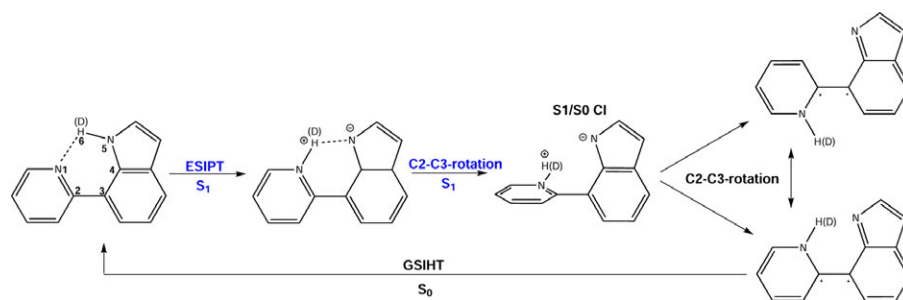

Figure 5. Proposed photochemical mechanism for 7PyIn. An ultrafast ESIPT process is followed by a N1−C2−C3−C4 twist that guides the system toward the conical intersection and allows internal conversion to the S_0 state. On average, the ESIPT process takes 274 fs in 7PyIn, and the internal conversion occurs after another 330 fs (see text for details).

case of an essentially barrierless ESIPT process where tunneling is not important. We have also analyzed the influence of the thermal fluctuations in the initially prepared sample on the photodynamics of 7PyIn and 7PyIn-D. The current study thus extends the use of trajectory-based nonadiabatic dynamics simulation methods to the study of nonequilibrium H/D isotope effects and temperature effects in ultrafast excited-state processes.

■ ASSOCIATED CONTENT

⑤ Supporting Information

Computational details; further OM2/MRCI validation for geometries and energies; figures with energy profiles, absorption spectrum, ESIPT and hopping time distributions, and typical trajectories; Cartesian coordinates of all optimized structures. This material is available free of charge via the Internet at http://pubs.acs.org.

■ AUTHOR INFORMATION

Corresponding Authors
*G. Cui: e-mail, ganglong@kofo.mpg.de.
*W. Thiel: e-mail, thiel@kofo.mpg.de.
Notes
The authors declare no competing financial interest.

■ ACKNOWLEDGMENTS

■ REFERENCES

(1) Lórenz-Fonfría, V.; Resler, T.; Krause, N.; Nack, M.; Gossing, M.; von Mollard, G.; Bamann, C.; Bamberg, E.; Schlesinger, R.; Heberle, J. Transient protonation changes in channelrhodopsin-2 and their relevance to channel gating. *Proc. Nat. Acad. Sci. U. S. A.* **2013**, *110*, 1273−1281.

(2) Cui, G.; Lan, Z.; Thiel, W. Intramolecular hydrogen bonding plays a crucial role in the photophysics and photochemistry of the GFP chromophore. *J. Am. Chem. Soc.* **2012**, *134*, 1662−1672.

(3) Pantazis, D.; Ames, W.; Cox, N.; Lubitz, W.; Neese, F. Two Interconvertible Structures that Explain the Spectroscopic Properties of the Oxygen-Evolving Complex of Photosystem II in the S2 State. *Angew. Chem., Int. Ed.* **2012**, *51*, 9935−9940.

(4) Lin, X.; Hu, X.; Concepcion, J.; Chen, Z.; Liu, S.; Meyer, T.; Yang, W. Theoretical study of catalytic mechanism for single-site water oxidation process. *Proc. Nat. Acad. Sci. U. S. A.* **2012**, *109*, 15669−15672.

(5) Tang, K.; Chang, M.; Lin, T.; Pan, H.; Fang, T.; Chen, K.; Hung, W.; Hsu, Y.; Chou, P. Fine tuning the energetics of excited-state intramolecular proton transfer (ESIPT): white light generation in a single ESIPT system. *J. Am. Chem. Soc.* **2011**, *133*, 17738−17745.

(6) Migani, A.; Bearpark, M.; Olivucci, M.; Robb, M. Photostability versus photodegradation in the excited-state intramolecular proton transfer of nitro enamines: Competing reaction paths and conical intersections. *J. Am. Chem. Soc.* **2007**, *129*, 3703−3713.

(7) Migani, A.; Blancafort, L.; Robb, M.; DeBellis, A. An extended conical intersection seam associated with a manifold of decay paths: excited-state intramolecular proton transfer in o-hydroxybenzaldehyde. *J. Am. Chem. Soc.* **2008**, *130*, 6932−6933.

(8) Shemesh, D.; Sobolewski, A.; Domcke, W. Efficient Excited-State Deactivation of the Gly-Phe-Ala Tripeptide via an Electron-Driven Proton-Transfer Process. *J. Am. Chem. Soc.* **2009**, *131*, 1374−1375.

(9) Li, X.; Chung, L.; Mizuno, H.; Miyawaki, A.; Morokuma, K. Primary events of photodynamics in reversible photoswitching fluorescent protein Dronpa. *J. Phys. Chem. Lett.* **2010**, *1*, 3328−3333.

(10) Hammes-Schiffer, S. Current Theoretical Challenges in Proton-Coupled Electron Transfer: Electron Proton Nonadiabaticity, Proton Relays, and Ultrafast Dynamics. *J. Phys. Chem. Lett.* **2011**, *2*, 1410−1416.

(11) Pu, J.; Gao, J.; Truhlar, D. Multidimensional tunneling, recrossing, and the transmission coefficient for enzymatic reactions. *Chem. Rev.* **2006**, *106*, 3140−3169.

(12) Lan, Z.; Frutos, L.; Sobolewski, A.; Domcke, W. Photochemistry of hydrogen-bonded aromatic pairs: Quantum dynamical calculations for the pyrrole-pyridine complex. *Proc. Nat. Acad. Sci. U. S. A.* **2008**, *105*, 12707−12712.

(13) Venkataraman, C.; Soudackov, A.; Hammes-Schiffer, S. Photoinduced homogeneous proton-coupled electron transfer: Model study of isotope effects on reaction dynamics. *J. Chem. Phys.* **2009**, *131*, 154502.

(14) Tully, J. Molecular dynamics with electronic transitions. *J. Chem. Phys.* **1990**, *93*, 1061−1071.

(15) Hammes-Schiffer, S.; Tully, J. Proton transfer in solution: Molecular dynamics with quantum transitions. *J. Chem. Phys.* **1994**, *101*, 4657−4667.

(16) Fabiano, E.; Keal, T.; Thiel, W. Implementation of surface hopping molecular dynamics using semiempirical methods. *Chem. Phys.* **2008**, *349*, 334−347.

(17) Coe, J.; Martinez, T. Competitive decay at two-and three-state conical intersections in excited-state intramolecular proton transfer. *J. Am. Chem. Soc.* **2005**, *127*, 4560−4561.

(18) Barbatti, M.; Lischka, H. Nonadiabatic Deactivation of 9H-Adenine: A Comprehensive Picture Based on Mixed Quantum-Classical Dynamics. *J. Am. Chem. Soc.* **2008**, *130*, 6831−6839.

(19) Tapavicza, E.; Tavernelli, I.; Rothlisberger, U.; Filippi, C.; Casida, M. Mixed time-dependent density-functional theory/classical trajectory surface hopping study of oxirane photochemistry. *J. Chem. Phys.* **2008**, *129*, 124108.

(20) Barbatti, M.; Aquino, A. J. A.; Lischka, H.; Schriever, C.; Lochbrunner, S.; Riedle, E. Ultrafast internal conversion pathway and mechanism in 2-(2′-hydroxyphenyl)benzothiazole: a case study for excited-state intramolecular proton transfer systems. *Phys. Chem. Chem. Phys.* **2009**, *11*, 1406−1415.

(21) Virshup, A. M.; Punwong, C.; Pogorelov, T. V.; Lindquist, B. A.; Ko, C.; Martínez, T. J. Photodynamics in Complex Environments: Ab Initio Multiple Spawning Quantum Mechanical/Molecular Mechanical Dynamics. *J. Phys. Chem. B* **2009**, *113*, 3280−3291.

(22) Barbatti, M.; Aquino, A. J. A.; Szymczak, J. J.; Nachtigallova, D.; Hobza, P.; Lischka, H. Relaxation mechanisms of UV-photoexcited DNA and RNA nucleobases. *Proc. Natl. Acad. Sci. U. S. A.* **2010**, *107*, 21453−21458.

(23) Barbatti, M. Nonadiabatic dynamics with trajectory surface hopping method. *WIREs Comput. Mol. Sci.* **2011**, *1*, 620−633.

(24) Curchod, B.; Rothlisberger, U.; Tavernelli, I. Trajectory-based Nonadiabatic Dynamics with Time-Dependent Density Functional Theory. *ChemPhysChem* **2013**, *14*, 1314−1340.

(25) Lan, Z.; Fabiano, E.; Thiel, W. Photoinduced Nonadiabatic Dynamics of Pyrimidine Nucleobases: On-the-Fly Surface-Hopping Study with Semiempirical Methods. *J. Phys. Chem. B* **2009**, *113*, 3548−3555.

(26) Lu, Y.; Lan, Z.; Thiel, W. Hydrogen Bonding Regulates the Monomeric Nonradiative Decay of Adenine in DNA Strands. *Angew. Chem., Int. Ed.* **2011**, *50*, 6864−6867.

(27) Weingart, O.; Lan, Z.; Koslowski, A.; Thiel, W. Chiral Pathways and Periodic Decay in cis-Azobenzene Photodynamics. *J. Phys. Chem. Lett.* **2011**, *2*, 1506−1509.

(28) Kazaryan, A.; Lan, Z.; Schäfer, L.; Thiel, W.; Filatov, M. Surface Hopping Excited-State Dynamics Study of the Photoisomerization of a Light-Driven Fluorene Molecular Rotary Motor. *J. Chem. Theory Comput.* **2011**, *7*, 2189−2199.

(29) Cui, G.; Thiel, W. Photoinduced Ultrafast Wolff Rearrangement: A Non-Adiabatic Dynamics Perspective. *Angew. Chem., Int. Ed.* **2013**, *52*, 433−436.

(30) Spörkel, L.; Cui, G.; Thiel, W. Photodynamics of Schiff base salicylideneaniline: Trajectory surface-hopping simulations. *J. Phys. Chem. A* **2013**, *117*, 4574−4583.

(31) Gamez, J.; Weingart, O.; Koslowski, A.; Thiel, W. Periodic Decay in the Photoisomerisation of p-Aminoazobenzene. *Phys. Chem. Chem. Phys.* **2013**, *15*, 11814−11821.

(32) Nosenko, Y.; Wiosna-Salyga, G.; Kunitski, M.; Petkova, I.; Singh, A.; Buma, W.; Thummel, R.; Brutschy, B.; Waluk, J. Proton transfer with a twist? Femtosecond Dynamics of 7-(2-pyridyl) indole in Condensed Phase and in Supersonic Jets. *Angew. Chem., Int. Ed.* **2008**, *47*, 6037−6040.

(33) Sobolewski, A.; Domcke, W. Computational studies of the photophysics of hydrogen-bonded molecular systems. *J. Phys. Chem. A* **2007**, *111*, 11725−11735.

(34) Kochman, M.; Morrison, C. Hybrid QM/QM Simulations of Excited-State Intramolecular Proton Transfer in the Molecular Crystal 7-(2-pyridyl)-indole. *J. Chem. Theory Comput.* **2013**, *9*, 1182−1192.

157

dx.doi.org/10.1021/jp4120749 | *J. Phys. Chem. A* 2014, 118, 152−157

71

Supporting Information: Nonequilibrium H/D Isotope Effects from Trajectory-based Nonadiabatic Dynamics

Lasse Spörkel, Ganglong Cui*, Axel Koslowski, and Walter Thiel*

October 1, 2013

Email: ganglong@kofo.mpg.de and thiel@kofo.mpg.de

Max-Planck-Institut für Kohlenforschung, Kaiser-Wilhelm-Platz 1, 45470 Mülheim an der Ruhr, Germany

Table of Contents

1

1 Electronic Structure Calculations

All semiempirical calculations were performed using the OM2/MRCI method, [1–3] as implemented in the MNDO99 code. [4] During optimizations, all required energies and gradients were computed analytically. Minimum-energy conical intersections were located using the Lagrange-Newton approach. [5]

The half-electron restricted open-shell Hartree-Fock (HF) formalism [6] was applied in the self-consistent fiel (SCF) treatment (i.e., the orbitals were optimized for the leading configu ation of the S_1 state with two singly occupied orbitals). The active space in the multi-reference configu ation interaction (MRCI) calculations included 12 electrons in 12 orbitals. In terms of the SCF conf guration, it comprised the fi e highest doubly occupied orbitals, the two singly occupied orbitals, and the fi e lowest unoccupied orbitals. For the MRCI treatment, three configu ation state functions were chosen as references, namely the SCF configu ation and the two closed-shell configu ations derived therefrom (i.e., all singlet configu ations that can be generated from the HOMO and LUMO of the closed-shell ground state). The MRCI wavefunction was built by allowing all single and double excitations from these three references. This semiempirical OM2/MRCI approach has been recently shown to perform well in a comprehensive general evaluation of excited-state properties [7] and in a number of recent excited-state studies. [8–20]

Ground-state geometries were also optimized using density functional theory (DFT) calculations with the hybrid B3LYP exchange-correlation functional [21–23] and the 6-31G* basis set. [24] Vertical excitation energies were calculated at these structures using the linear-response TD-DFT (time-dependent DFT) approach, the B3LYP [21–23] and CAM-B3LYP [25] functionals, and the 6-31++G** basis set. [26]

The parameterized, DFT-based multi-reference configu ation interaction (DFT/MRCI) method [27] was also used to calculate the vertical excitation energies. To be consistent with the original parameterization, the hybrid BHLYP functional [23] and the TZVP basis set [28, 29] were employed in the DFT/MRCI calculations.

In addition, the complete-active-space self-consistent fiel (CASSCF) method was applied to optimize the ground- and excited-state structures and to scan the relevant potential energy profile . In the CASSCF calculations, an active space of ten electrons in eight orbitals was adopted. The multi-state CASSCF second-order perturbation method (CASPT2) [30] was employed to determine improved single-point energies at all CASSCF structures. The MS-CASPT2 calculations were done using two roots with equal weights and the imaginary shift technique (0.3 a.u.). [31]

The following codes were used for the electronic structure calculations in this work: ChemShell 3.4 [32] and MNDO99 [4] for OM2/MRCI; GAUSSIAN09 [33] for DFT, TD-DFT, and minimum-energy conical intersection optimizations (CASSCF); MOLCAS 7.6 [34, 35] for CASSCF and MS-CASPT2; and TURBOMOLE 5.7.1 [36] for DFT/MRCI. [27]

2

Table 1: The Number of Trajectories that (a) Undergo ESIPT, (b) Decay to the S_0 State, and (c) Remain in the S_1 State until the End of the Simulation.

Temperature (T)	Total	ESIPT	S_0	S_1	Total	ESIPT	S_0	S_1
		7PyIn-H				7PyIn-D		
All	632	626	569	63	735	714	631	104
T < 275 K	219	216	202	17	344	335	300	44
275 K < T < 325 K	251	249	218	33	253	245	217	36
T > 325 K	162	161	149	13	138	134	114	24

2 Dynamics Simulations

In trajectory surface hopping dynamics, there are two main initial-condition sampling schemes. The firs one is Wigner sampling, [37, 38] which generates initial coordinates and velocities based on classical or quantum harmonic vibrational modes. The second one is based on canonical classical molecular dynamics (MD). The canonical distribution is satisfie with the use of thermostat algorithms, such as velocity rescaling [39], the Berendsen thermostat, [40] the Andersen thermostat, [41] the Nose-Hoover thermostat, [42, 43] Nose-Hoover chains, [44] or Langevin dynamics [45]. Here, we adopted the Nose-Hoover chains algorithm (with a chain length of 10) for this purpose. We used the default characteristic time of 0.5 ps for the thermostat and a timestep of 1 fs for nuclear motion.

For both target molecules (7PyIn and the deuterated isotopomer 7PyIn-D), ground-state MD runs were performed at the SCC-DFTB level: [46–48] 7 ps of equilibration dynamics were followed by a 10 ps production run, from which 1000 initial atomic coordinates and velocities were randomly selected. The starting points for the subsequent OM2/MRCI nonadiabatic dynamics runs were chosen from this set on the basis of the computed $S_0 \rightarrow S_1$ transition probabilities. A total of 834 [820] surface-hopping trajectories were run up to 2 ps for 7PyIn [7PyIn-D], with all relevant energies, gradients, and nonadiabatic coupling vectors being computed on-the-fl as needed. For points with an $S_1 - S_0$ energy gap of less than 10 kcal/mol, the fewest-switches criterion was applied to decide whether to hop. [49, 50] The time step was chosen to be 0.1 fs for nuclear motion and 0.0005 fs for electronic propagation. The unitary propagator evaluated at the middle point was used to propagate electronic motion. [51, 52] Translational and rotational motions were removed in each step. The empirical decoherence correction (0.1 au) proposed by Granucci et al. was employed. [53] The fina evaluations were done for the 632 [735] trajectories (see Table 1) that finishe   successfully and satisfie   our energy continuity criterion (no changes greater than 30 kcal/mol between any two consecutive MD steps). To analyze the effect of thermal fluctuation on the photodynamics of 7PyIn and 7PyIn-D, the trajectories were apportioned into three temperature windows according to the initial conditions. Further technical details are given in our previous publications. [8–20, 51, 52] The SCC-DFTB sampling with the Nose-Hoover chains technique was done with ChemShell 3.4 [32] and the nonadiabatic OM2/MRCI dynamics simulations were conducted with MNDO99. [4]
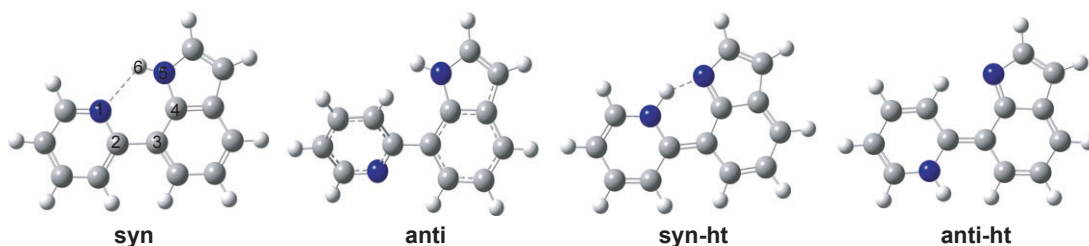
syn   **anti**   **syn-ht**   **anti-ht**

Figure 1: Schematic ground-state geometries optimized in this work. In the S_0 state, the syn conformer is most stable. Also shown for syn is the chosen numbering scheme.

Table 2: Selected Geometric Parameters and Relative Energies of the Optimized Structures Obtained from OM2/MRCI, B3LYP and CASSCF

	N1-H6 (Å)	N5-H6 (Å)	C2-C3 (Å)	N1-C2-C3-C4 (°)	Energies (kcal/mol)
			OM2/MRCI		
S0-syn	2.14	1.01	1.48	0.0	0.0
S0-anti	4.10	1.01	1.49	140.3	3.0
S0-anti-ht	1.02	4.93	1.43	179.9	49.4
S1-syn	1.90	1.04	1.44	0.0	96.3
			B3LYP/6-31G*		
S0-syn	2.09	1.01	1.48	0.0	0.0
S0-syn-ht	1.11	1.53	1.44	0.0	17.8
S0-anti	4.18	1.01	1.48	148.3	5.9
S0-anti-ht	1.01	4.92	1.43	179.8	34.4
		MS-CASPT2/6-31G*//CASSCF(10,8)/6-31G*			
S0-syn	2.18	0.99	1.49	0.0	0.0
S1-syn	1.91	1.01	1.43	0.0	99.9

The results from the static electronic structure calculations are of course identical for 7PyIn and 7PyIn-D since the nuclear masses do not enter the electronic Hamiltonian. In the dynamics simulations, the atomic mass of the H6 (D6) atom in 7PyIn (7PyIn-D) was assigned to be 1.008 (2.014) amu. This small mass difference has a remarkable influenc on the photodynamics.

3 S_0 Minima and Potential Energy Profile

In the ground state there are four possible conformers (see Fig. 1), which are referred to as syn, anti, syn-ht, and anti-ht, respectively. The lowest among them is the syn conformer that is more stable than the anti conformer by 5.9 kcal/mol at the B3LYP/6-31G* level and 3.0 kcal/mol at the OM2/MRCI level (see Table 2 and the right panel of Fig. 2). Hydrogen transfer of H6 in the syn arrangement yields the syn-ht tautomer. At the B3LYP/6-31G* level, it lies 17.8 kcal/mol above the syn conformer; a scan of the S_0 potential energy profil along the hydrogen transfer shows that syn-ht is metastable and occupies a very shallow potential well (with a lowest harmonic frequency of only 78 cm^{-1}). At the OM2/MRCI level, there is no syn-ht minimum: all geometry optimization
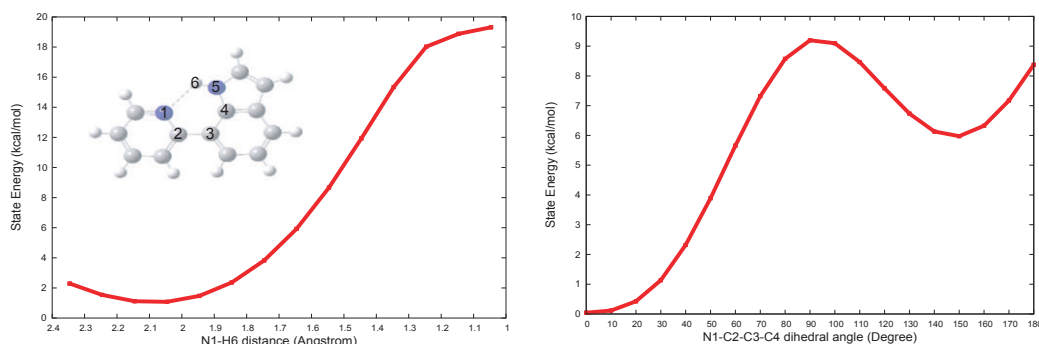
4

Figure 2: B3LYP/6-31G* energy profile for one-dimensional relaxed minimum-energy paths along the N1-H6 bond length (left) and the N1-C2-C3-C4 dihedral angle (right).

attempts starting from a syn-ht-type structure ended up back at the syn conformer. Finally, the anti-ht conformer is dynamically unimportant because of its very high potential energy, 34.4 kcal/mol at the B3LYP/6-31G* level and 49.4 kcal/mol at the OM2/MRCI level.

4   Absorption Spectrum

To investigate the excited states in the Franck-Condon region, the vertical absorption spectrum of the S0-syn conformer was computed at the TD-DFT/6-31++G**//B3LYP/6-31G* level using the B3LYP, CAM-B3LYP, and M06-2X exchange-correlation functionals. The spin-allowed $S_0 \to S_1$ electronic transition is found to give rise to the strongest absorption band (see Fig. 3). This excited singlet state is of partial charge-transfer character so that the conventional global hybrid functional B3LYP underestimates the excitation energy by ca. 0.5 eV, compared with range-separated (CAM-B3LYP) and modern (M06-2X) functionals. The latter give vertical excitation energies (4.06–4.08 eV) that are close to the values from DFT/MRCI (3.95 eV), and CC2 (4.0 eV), but lower than those from OM2/MRCI (4.37 eV) and MS-CASPT2//CASSCF (4.34 eV).

5   Conical Intersections

Conical intersections play a central role in nonadiabatic dynamics simulations. The chosen electronic structure method must therefore be able to describe conical intersections reasonably well.

Table 3 lists selected geometric parameters for conical intersection structures obtained from OM2/MRCI and CASSCF. The SA2-CASSCF/6-31G* optimization yields a twisted structure with an N1-C2-C3-C4 dihedral angle of 68° and an N5-H6 distance of 2.55 Å that indicates a weak hydrogen bonding interaction. The energy of this structure relative to the ground-state minimum is 84.3 kcal/mol at the CASSCF level. Single-point MS-
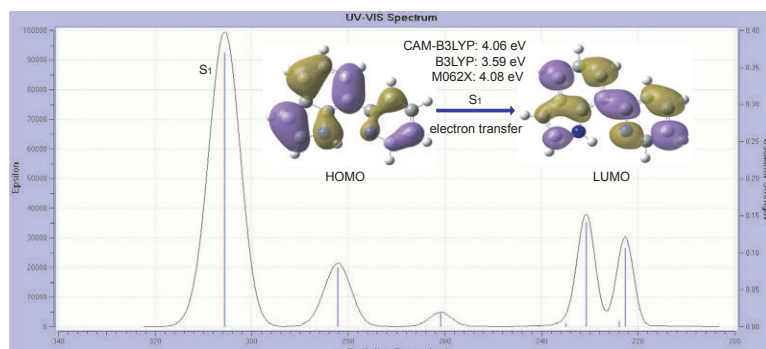
5

Figure 3: Absorption spectrum (half-width at half height: 0.05 eV) from CAM-B3LYP/6-31++G**//B3LYP/6-31G* calculations.

Table 3: Selected Geometric Parameters and Relative Energies of the Optimized Conical Intersections Obtained from OM2/MRCI and CASSCF (see text)

	N1-H6 (Å)	N5-H6 (Å)	C2-C3 (Å)	N1-C2-C3-C4 (°)	Energies (kcal/mol)
OM2/MRCI					
S1S0-MECI-1	1.06	2.03	1.50	50.4	78.8
S1S0-MECI-2	1.05	2.15	1.49	56.6	78.8
S1S0-MECI-3	1.02	2.92	1.48	67.7	82.6
S1S0-MECI-4	1.02	3.50	1.48	90.4	77.3
CASSCF(10,8)/6-31G*					
S1S0-MECI	1.00	2.55	1.49	63.2	84.3

CASPT2/6-31G* calculations lead to a splitting of the two degenerate CASSCF states, with energies of 67.0 and 77.6 kcal/mol.

At the OM2/MRCI level, we fin that the optimizations converge to conical intersection structures with different N1-C2-C3-C4 dihedral angles and N5-H6 distances depending on the N1-C2-C3-C4 value in the starting geometry and on the chosen convergence criteria. Table 3 lists four such structures with varying degrees of hydrogen bonding (see N5-H6 distance). Their energies are rather similar (77.3–82.6 kcal/mol) and lie in the range of the MS-CASPT2/6-31G* and CASSCF/6-31G* values (see above). The lowest-energy species S1S0-MECI-4 has a perpendicular conformation without N5-H6 hydrogen bonding (at 77.3 kcal/mol). In the main paper, we refer to this species as the S1S0-MECI from OM2/MRCI.

To summarize, the OM2/MRCI approach yields a rather extended conical intersection region, with similar energies for N1-C2-C3-C4 dihedral angles between 50° and 90°. The S1S0-MECI obtained from CASSCF is embedded into this region in terms of its structure, and the corresponding CASSCF and MS-CASPT2 single-point energies are of similar magnitude as the OM2/MRCI values.

6

6 S_1 Minimum-Energy Profile

Figs. 4–6 show the minimum-energy profile along the relevant reaction paths at the MS-CASPT2//CASSCF, CASSCF, and OM2/MRCI levels, respectively, obtained at the optimized S_1 geometries (full relaxation of all degrees of freedom except for the reaction coordinate). The left panels depict the potential energy profile for ESIPT using the distance N1-H6 of the forming covalent bond as the reaction coordinate. The shape of these curves is similar at all three levels: the optimized S_1 energies stay roughly at a plateau down to an N1-H6 distance of 1.6 Å and then drop as the covalent N1-H6 bond is formed, while the single-point S_0 energies go through a maximum at ca. 1.2 Å but always remain below their S_1 counterparts. In absolute terms, the S_1 energies are highest for CASSCF, the inclusion of dynamic correlation in CASPT2 causes a downward shift of ca. 10 kcal/mol, and the OM2/MRCI results are still somewhat lower (by ca. 5-10 kcal/mol). The right panels of Figs. 4–6 display the S_1 and S_0 potential energy profile along the N1-C2-C3-C4 dihedral angle, which provide the link to the S_1/S_0 conical intersection. On these pathways, the conical intersection is encountered at a N1-C2-C3-C4 dihedral angle of ca. 70° for CASSCF and ca. 80° for OM2/MRCI; it becomes an avoided crossing at the MS-CASPT2 level. During the approach to the conical intersection region, the S_1 profile remain rather fla in all cases (with barriers not exceeding 2 kcal/mol), while the S_0 profile show a monotonous increase of ca. 15–25 kcal/mol. Overall, the OM2/MRCI curves are similar enough to their CASSCF and MS-CASPT2 counterparts to support the use of the OM2/MRCI method in the nonadiabatic simulations (see Figs. 4–6).

Finally, we note that analogous energy profile have been published previously at the CC2/cc-pVDZ level for geometries optimized at MP2/SV(P) (S_0) and CC2/SV(P) (S_1), see Figure 12 of Ref. [54]. The shapes of these profile are qualitatively similar to those shown here. It should be noted in this context that the S_1 energy profil for ESIPT in Ref. [54] seems to drop off significantl faster than those presented here. This is due to the fact that the S_1 curve in Ref. [54] refers to a different reaction coordinate, i.e. the distance N5-H6 of the covalent bond being broken (rather than the distance N1-H6 chosen here); we have confi med that the OM2/MRCI curve for the S_1 ESIPT process also drops off fast when using N5-H6 as reaction coordinate (like in the CC2 case, data not shown).

7 Nonequilibrium H/D Isotope Effects

Nonequlibrium H/D isotope effects may occur in chemical reactions when thermodynamic equilibrium is not achieved before the reaction is complete, for example in the case of ultrafast excited-state proton transfer.

From the present dynamics simulations, we can determine the time required for the ESIPT process in each trajectory. We have adopted the geometric criterion to measure the ESIPT time at the point when the distance in the breaking N5-H6 bond exceeds 1.5 Å. The corresponding ESIPT time distributions for 7PyIn and 7PyIn-D
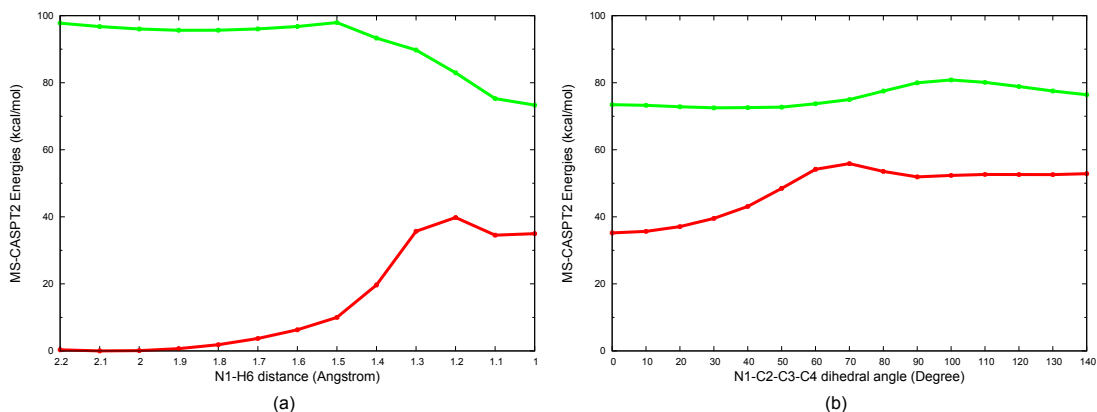
7

Figure 4: MS-CASPT2/6-31G*//SA3-CASSCF(10,8)/6-31G* energy profile for relaxed one-dimensional minimum-energy paths (MEPs) along the N1-H6 bond length (left) and the N1-C2-C3-C4 dihedral angle (right). The S_1 MEP is fully optimized with respect to the other coordinates at the CASSF level, while the S_0 curve is obtained from single-point calculations.
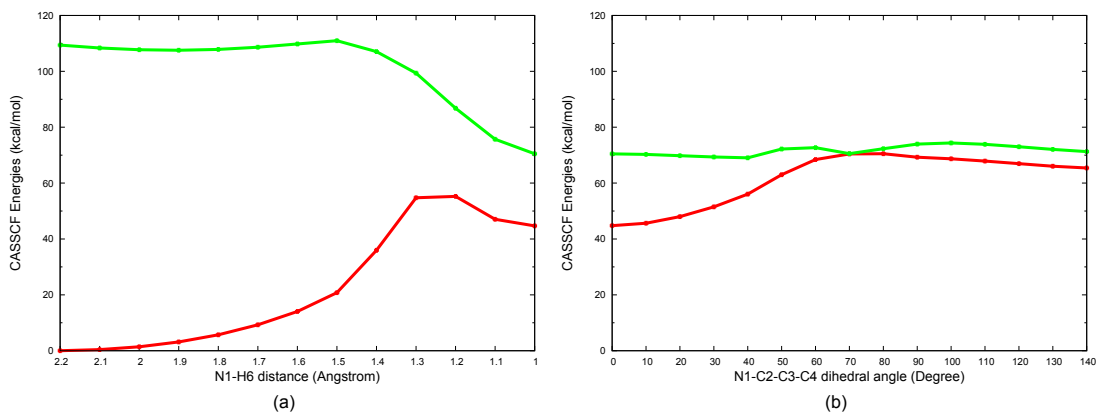

Figure 5: SA3-CASSCF(10,8)/6-31G* energy profile for relaxed one-dimensional minimum-energy paths (MEPs) along the N1-H6 bond length (left) and the N1-C2-C3-C4 dihedral angle (right). The S_1 MEP is fully optimized with respect to the other coordinates, while the S_0 curve is obtained from single-point calculations.
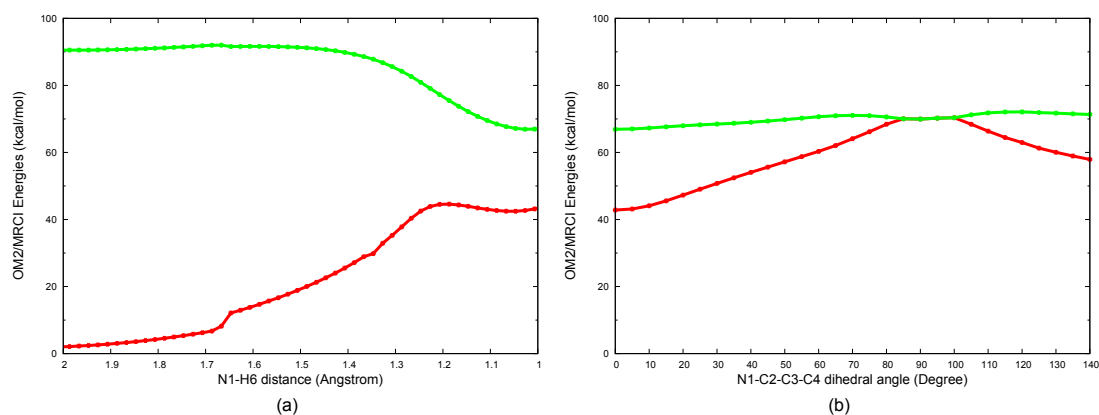
8

Figure 6: OM2/MRCI energy profile for relaxed one-dimensional minimum-energy paths (MEPs) along the N1-H6 bond length (left) and the N1-C2-C3-C4 dihedral angle (right). The S_1 MEP is fully optimized with respect to the other coordinates, while the S_0 curve is obtained from single-point calculations.
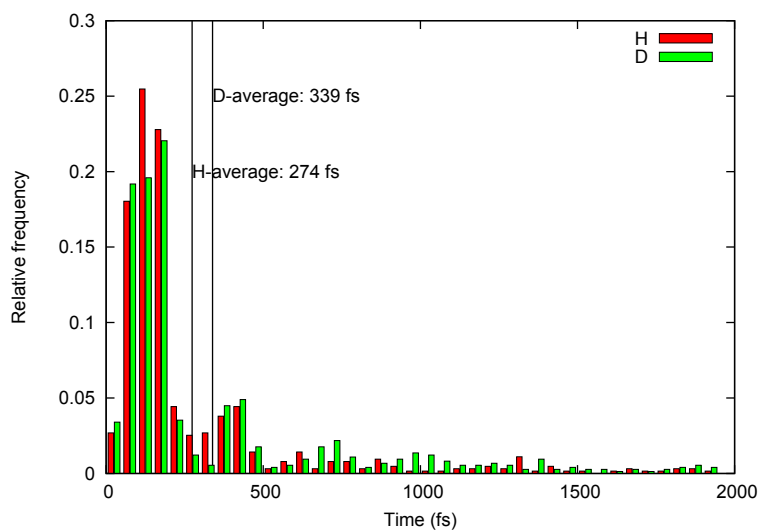

Figure 7: ESIPT time distribution for 7PyIn and 7PyIn-D (see text). The H/D isotope effect shifts this distribution towards longer times.
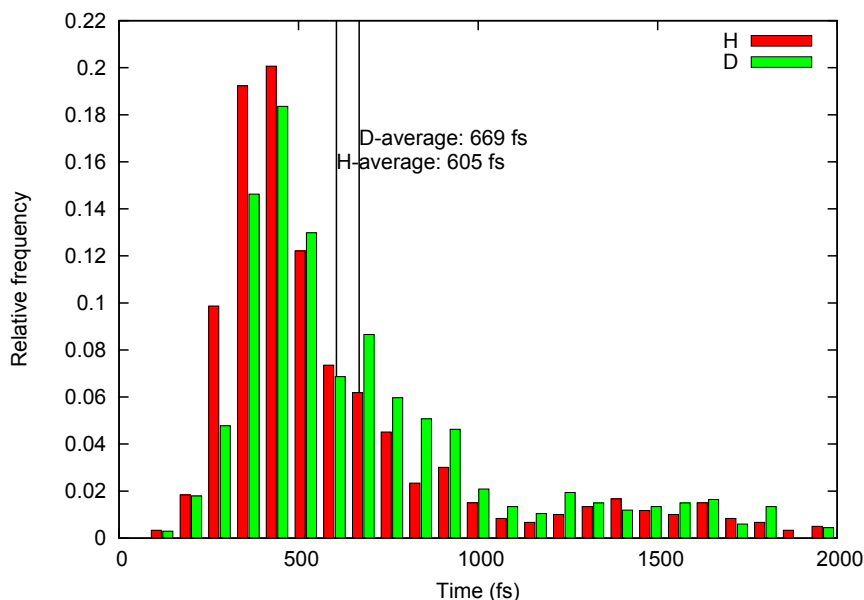
9

Figure 8: Time distributions of the $S_1 \rightarrow S_0$ internal conversion for 7PyIn and 7PyIn (D). The H/D isotope effect shifts this distribution towards longer times.

are shown in Fig. 7 along with their average values. These average ESIPT times change by less than 2 fs when applying the alternative criterion that the length of the forming N1-H6 bond drops below 1.1 Å. They are consistent with the measured spectroscopic data and isotope effects. Nosenko *et al.* attributed the firs ion signal in their pump-probe REMPI spectra to the ESIPT process and determined its time to be 280 fs in 7PyIn and 390 fs in 7PyIn-D.[55] Both are close to our estimates of 274 fs [7PyIn] and 339 fs [7PyIn-D], respectively. In addition, we fin that the peak of the ESIPT time distribution is shifted by ca. 50 fs when H is replaced by D, from ca. 150 fs (H, 26%) to ca. 200 fs (D, 22%).

Isotope effects are also seen in the distribution of the $S_1 \rightarrow S_0$ internal conversion time (see Fig. 8). Here the average hopping time is 64 fs longer for 7PyIn-D than for 7PyIn (669 fs vs. 605 fs). This indicates some correlation between the timing of proton transfer and internal conversion, the latter occurring on average about 330 fs after the former (for both isotomers).

The decomposition into different starting temperatures is shown for proton transfer in Fig. 9 and for internal conversion in Fig. 10. The average ESIPT times tend to increase with increasing temperature of the chosen temperature windows (7PyIn from 265 fs to 283 and 281 fs; 7PyIn-D from 301 fs to 381 and 410 fs), which has been rationalized in the main paper by the increased number of nonplanar starting geometries with out-of-plane distortions that are detrimental to the in-plane ESIPT process. The average hopping times seem to inherit this trend of increasing values (7PyIn from 597 fs to 628 and 582 fs; 7PyIn-D from 653 fs to 662 and 722 fs), but to

10

a lesser extent. The approach to the hopping point in the conical intersection region requires a rotation around the central C2-C3 bond (after ESIPT, see above), which may indeed be facilitated by out-of-plane distortions in the starting geometries that occur at higher temperatures. This may explain the decrease in the average internal conversion time that we fin for 7PyIn in the highest temperature window.

8 Representative Trajectories

Fig. 11 (H) and 12 (D) show the time-dependent evolution of three key geometric parameters, the S_1/S_0 nona-diabatic coupling, and the S_1-S_0 energy gap during two typical trajectories. Both trajectories sample the same photophysical and photochemical events but at different times.

In the 7PyIn trajectory, the H6 atom is bound to the N5 atom for the firs 180 fs, with a stable N1$\cdots$H6-N5 hydrogen bond (see Fig. 11). During this period, the S_1-S_0 energy gap is very large (more than 80 kcal/mol), the S_1/S_0 nonadiabatic coupling is small, and hence the excited-state decay is impossible. The excited-state proton transfer takes place at ca. 180 fs, which immediately yields a planar tautomer (syn-ht) with the N1-H6$\cdots$N5 hydrogen-bond pattern. After roaming in the resulting planar conformation for ca. 200 fs, the N1-C2-C3-C4 dihedral angle starts to twist, and the system then decays to the ground state via an S_1/S_0 conical intersection after ca. 800 fs. At this point, the nonadiabatic coupling is much larger (see top-right panel of Fig. 11). After ca. 100 fs of roaming in the S_0 state, the H6 atom returns to N5, with quick formation of the syn conformer (see N1-H6 and N5-H6) that triggers internal rotation around the central C2-C3 bond (see N1-C2-C3-C4) and a strong increase in the S_1-S_0 energy gap.

Similar dynamical features are observed for the deuterated isotopomer (see Fig. 12), albeit at different times. Here, the proton transfer happens after a much longer roaming period of 800 fs, possibly because of the more "damped" oscillations in the deuterium case (due to the higher mass). The excited-state decay occurs after another 200 fs at around 1000 fs, after some twist around the N1-C2-C3-C4 dihedral angle (see above) that should not be affected much by isotopic substitution. After the conversion to the ground state, the deuterium takes 250 fs for the transfer back to the initial position (syn conformer), which is again much longer than the 100 fs for the parent system. Isotope effects can thus generally be seen at the trajectory level for processes directly involving the H atom being replaced by D.
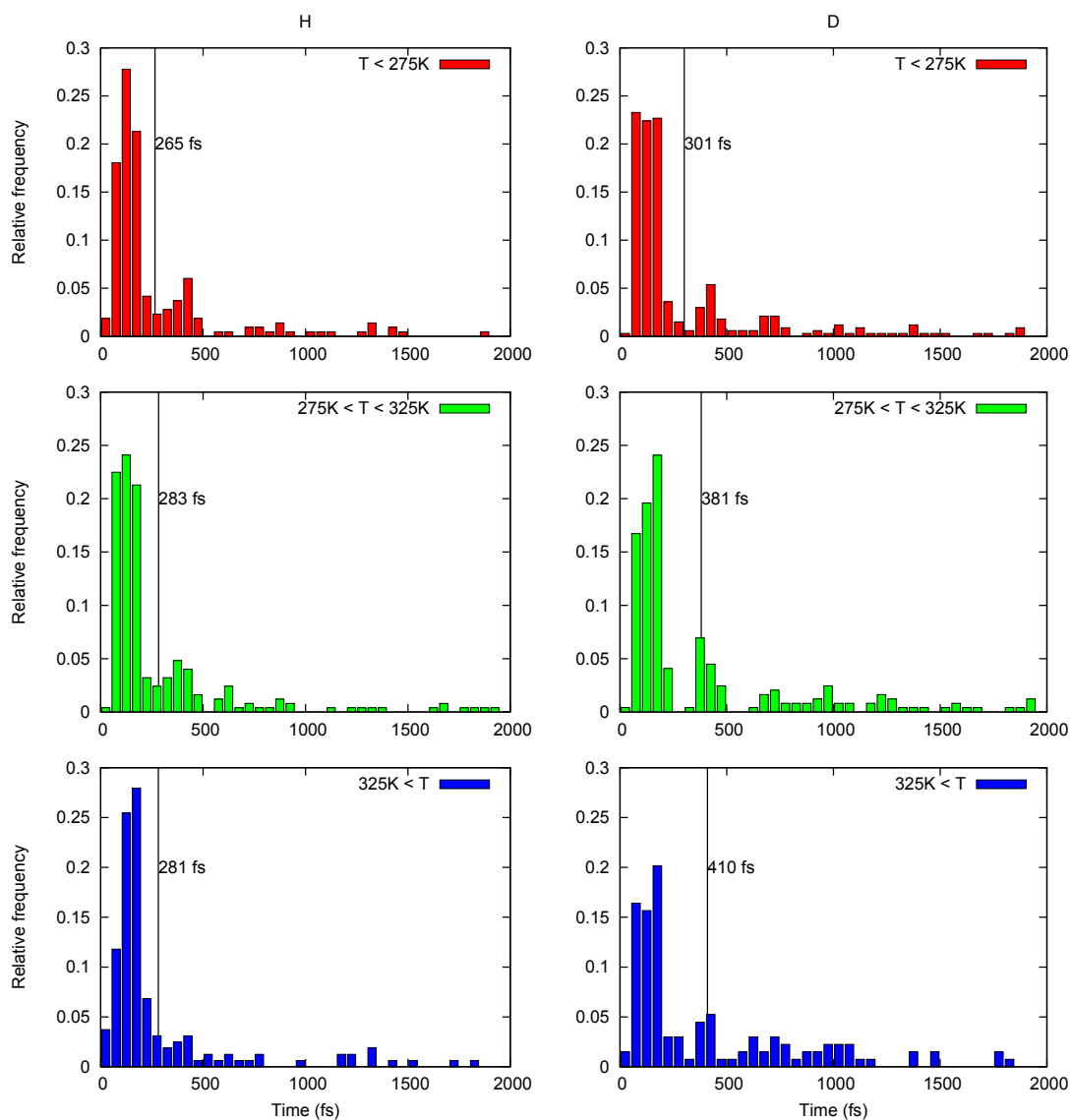
11

Figure 9: ESIPT time distributions in three temperature windows of initial conditions (top: less than 275 K; middle: between 275 and 325 K; bottom: larger than 325 K).
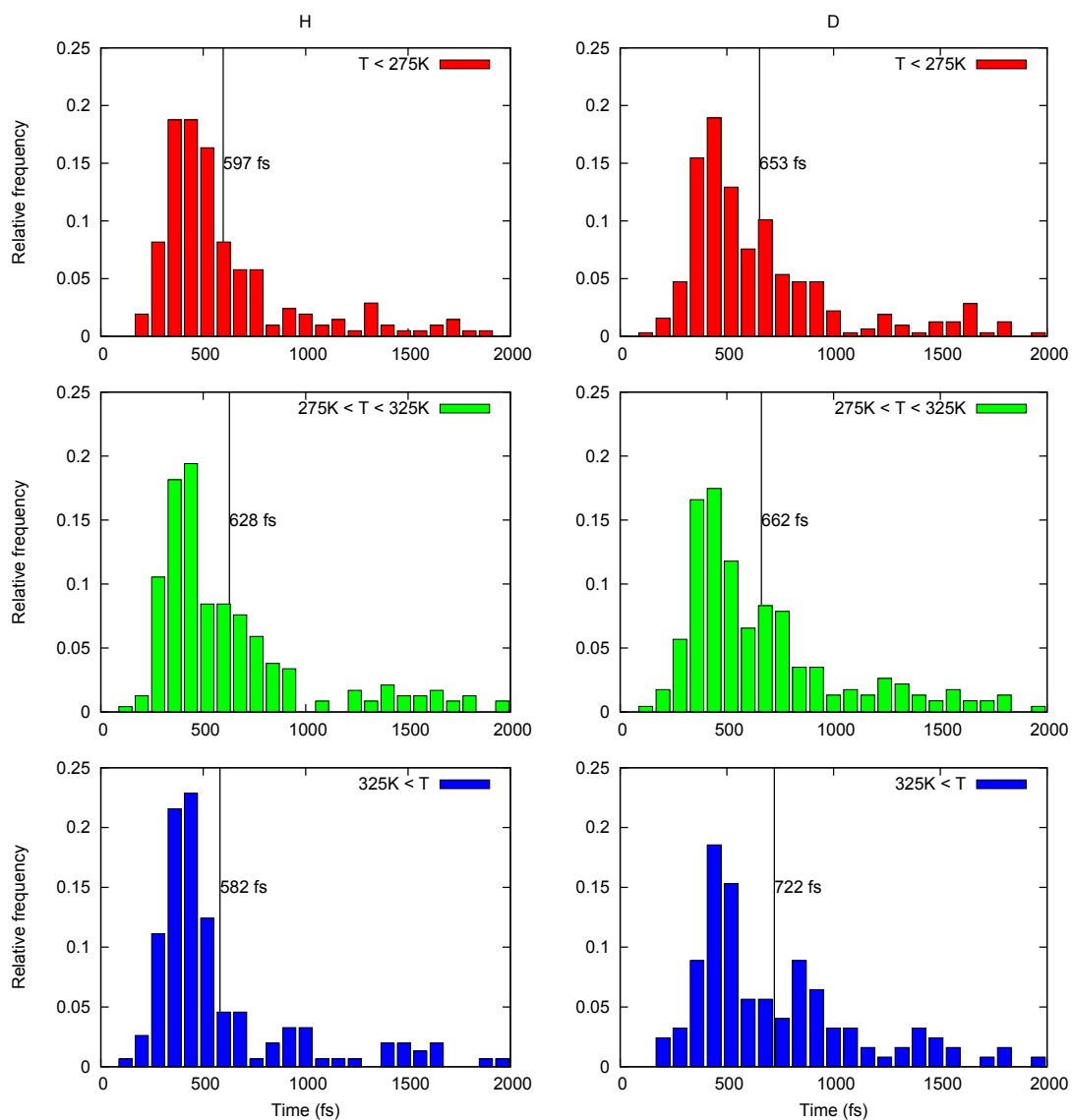
12

Figure 10: Hopping time distributions for the $S_1 \rightarrow S_0$ internal conversion in three temperature windows of initial conditions (top: less than 275 K; middle: between 275 and 325 K; bottom: greater than 325 K).

13

Figure 11: A typical trajectory for 7PyIn. The excited-state proton transfer and the $S_1 \rightarrow S_0$ internal conversion are completed after ca. 180 fs and after ca. 800 fs, respectively. In the S_0 state, the hydrogen atom is transferred back to the original donor atom. See the text for more detail.
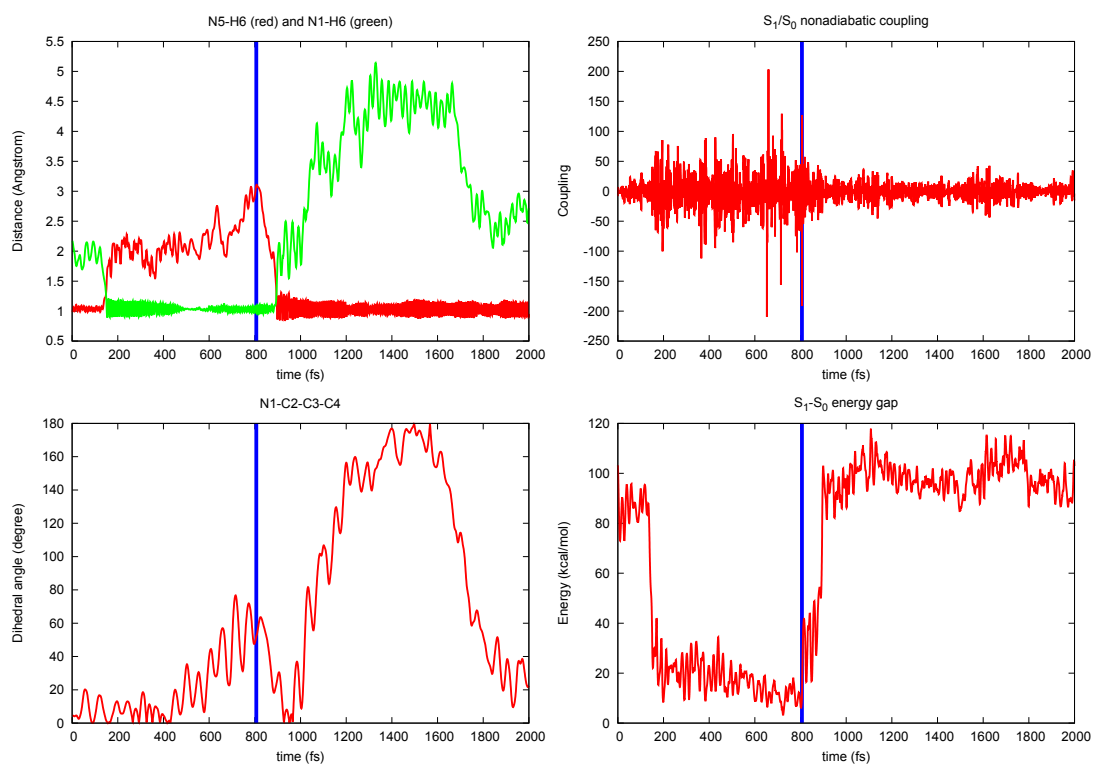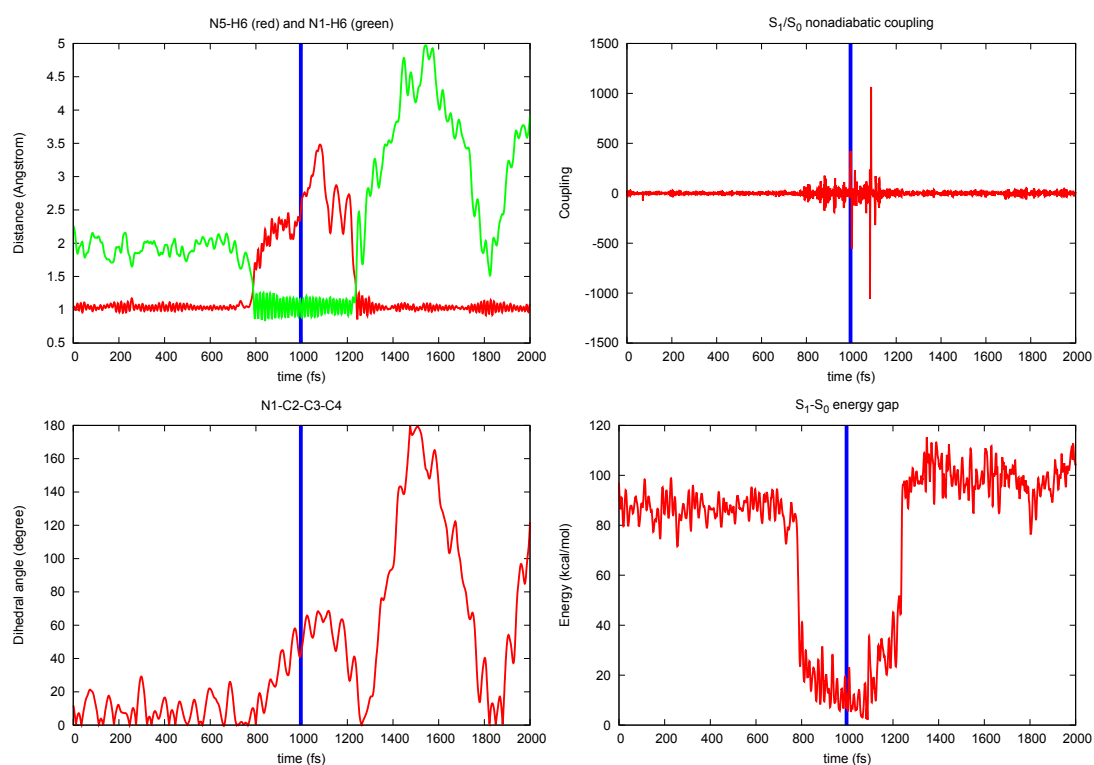
14

Figure 12: A typical trajectory for 7PyIn-D. The excited-state proton transfer and the $S_1 \rightarrow S_0$ internal conversion are completed after ca. 800 fs and after another 200 fs, respectively. In the S_0 state, the hydrogen atom is transferred back to the original donor atom. See the text for more detail.

15

References

[1] W. Weber. PhD thesis, University of Zürich, 1996.

[2] W. Weber and W. Thiel. Orthogonalization corrections for semiempirical methods. *Theor. Chem. Acc.*, 103:495–506, 2000.

[3] A. Koslowski, M.E. Beck, and W. Thiel. Implementation of a general multireference configu ation interaction procedure with analytic gradients in a semiempirical context using the graphical unitary group approach. *J. Comput. Chem.*, 24:714–726, 2003.

[4] W. Thiel. MNDO99 program, version 6.1, 2007. Max-Planck-Institut für Kohlenforschung, Mülheim, Germany, 2007.

[5] T.W. Keal, A. Koslowski, and W. Thiel. Comparison of algorithms for conical intersection optimisation using semiempirical methods. *Theor. Chem. Acc.*, 118:837–844, 2007.

[6] M.J.S. Dewar, J.A. Hashmall, and C.G. Venier. Ground states of conjugated molecules. IX. Hydrocarbon radicals and radical ions. *J. Am. Chem. Soc.*, 90:1953–1957, 1968.

[7] M.R. Silva-Junior and W. Thiel. Benchmark of Electronically Excited States for Semiempirical Methods: MNDO, AM1, PM3, OM1, OM2, OM3, INDO/S, and INDO/S2. *J. Chem. Theory Comput.*, 6:1546–1564, 2010.

[8] E. Fabiano and W. Thiel. Nonradiative deexcitation dynamics of 9H-adenine: An OM2 surface hopping study. *J. Phys. Chem. A*, 112:6859–6863, 2008.

[9] Z.G. Lan, E. Fabiano, and W. Thiel. Photoinduced Nonadiabatic Dynamics of Pyrimidine Nucleobases: On-the-Fly Surface-Hopping Study with Semiempirical Methods. *J. Phys. Chem. B*, 113:3548–3555, 2009.

[10] Z.G. Lan, E. Fabiano, and W. Thiel. Photoinduced Nonadiabatic Dynamics of 9H-Guanine. *ChemPhysChem*, 10:1225–1229, 2009.

[11] Z.G. Lan, Y. Lu, E. Fabiano, and W. Thiel. QM/MM Nonadiabatic Decay Dynamics of 9H-Adenine in Aqueous Solution. *ChemPhysChem*, 12:1989–1998, 2011.

[12] Y. Lu, Z.G. Lan, and W. Thiel. Hydrogen Bonding Regulates the Monomeric Nonradiative Decay of Adenine in DNA Strands. *Angew. Chem. Int. Ed.*, 50:6864–6867, 2011.

[13] O. Weingart, Z.G. Lan, A. Koslowski, and W. Thiel. Chiral Pathways and Periodic Decay in cis-Azobenzene Photodynamics. *J. Phys. Chem. Lett.*, 2:1506–1509, 2011.

[14] A. Kazaryan, Z.G. Lan, L.V. Schäfer, W. Thiel, and M. Filatov. Surface Hopping Excited-State Dynamics Study of the Photoisomerization of a Light-Driven Fluorene Molecular Rotary Motor. *J. Chem. Theory Comput.*, 7:2189–2199, 2011.

[15] Z.G. Lan, Y. Lu, O. Weingart, and W. Thiel. Nonadiabatic Decay Dynamics of a Benzylidene Malononitrile. *J. Phys. Chem. A*, 116:1510–1518, 2012.

[16] Y. Lu, Z.G. Lan, and W. Thiel. Monomeric adenine decay dynamics influence   by the DNA environment. *J. Comput. Chem.*, 33:1225–1235, 2012.

[17] G.L. Cui, Z.G. Lan, and W. Thiel. Intramolecular hydrogen bonding plays a crucial role in the photophysics and photochemistry of the GFP chromophore. *J. Am. Chem. Soc.*, 134:1662–1672, 2012.

[18] G.L. Cui and W. Thiel. Nonadiabatic dynamics of a truncated indigo model. *Phys. Chem. Chem. Phys.*, 14:12378–12384, 2012.

[19] G.L. Cui and W. Thiel. Photoinduced Ultrafast Wolff Rearrangement: A Non-Adiabatic Dynamics Perspective. *Angew. Chem. Int. Ed.*, 52:433–436, 2013.

[20] L. Spörkel, G.L. Cui, and W. Thiel. Photodynamics of Schiff base salicylideneaniline: Trajectory surface-hopping simulations. *J. Phys. Chem. A*, 117:4574–4583, 2013.

[21] A.D. Becke. Density-functional exchange-energy approximation with correct asymptotic behavior. *Phys. Rev. A*, 38:3098–3100, 1988.

[22] C. Lee, W.T. Yang, and R.G. Parr. Development of the Colle-Salvetti correlation-energy formula into a functional of the electron density. *Phys. Rev. B*, 37:785–789, 1988.

[23] A.D. Becke. A new mixing of Hartree-Fock and local density-functional theories. *J. Chem. Phys.*, 98:1372–1377, 1993.

[24] R. Ditchfield W.J. Hehre, and J.A. Pople. Self-Consistent Molecular-Orbital Methods. IX. An Extended Gaussian-Type Basis for Molecular-Orbital Studies of Organic Molecules. *J. Chem. Phys.*, 54:724–728, 1971.

[25] T. Yanai, D.P. Tew, and N.C. Handy. A new hybrid exchange-correlation functional using the Cooulomb-attenuated method CAM-B3LYP. *Chem. Phys. Lett.*, 393:51–57, 2004.

[26] T.H. Dunning Jr. Gaussian basis sets for use in correlated molecular calculations. I. The atoms boron through neon and hydrogen. *J. Chem. Phys.*, 90:1007–1023, 1989.

[27] S. Grimme and M. Waletzke. A combination of Kohn–Sham density functional theory and multi-reference configu ation interaction methods. *J. Chem. Phys.*, 111:5645–5655, 1999.

[28] A. Schäfer, H. Horn, and R. Ahlrichs. Fully optimized contracted Gaussian basis sets for atoms Li to Kr. *J. Chem. Phys.*, 97:2571–2577, 1992.

[29] A. Schäfer, C. Huber, and R. Ahlrichs. Fully optimized contracted Gaussian basis sets of triple zeta valence quality for atoms Li to Kr. *J. Chem. Phys.*, 100:5829–5835, 1994.

[30] K. Andersson, P.Å. Malmqvist, and B.O. Roos. Second-order perturbation theory with a complete active space self-consistent fiel reference function. *J. Chem. Phys.*, 96:1218, 1992.

[31] N. Försberg and P.Å. Malmqvist. Multiconfigu ation perturbation theory with imaginary level shift. *Chem. Phys. Lett.*, 274:196–204, 1997.

[32] ChemShell3.4, a Computational Chemistry Shell, see www.chemshell.org.

[33] M.J. Frisch, G.W. Trucks, H.B. Schlegel, G.E. Scuseria, M.A. Robb, J.R. Cheesem, G. Scalmani, V. Barone, B. Mennucci, G.A. Petersson, H. Nakatsuji, M. Caricato, X. Li, H.P. Hratchian, A.F. Izmaylov, J. Bloino, G. Zheng, J.L. Sonnenberg, M. Hada, M. Ehara, K. Toyota, R. Fukuda, J. Hasegawa, M. Ishida, T. Nakajima, Y. Honda, O. Kitao, H. Nakai, T. Vreven, J.A. Montgomery Jr., J.E. Peralta, F. Ogliaro, M. Bearpark, J.J. Heyd, E. Brothers, K.N. Kudin, V.N. Staroverov, R. Kobayashi, J. Normand, K. Raghavachari, A. Rendell, J.C. Burant, S.S. Iyengar, J. Tomasi, M. Cossi, N. Rega, J.M. Millam, M. Klene, J.E. Knox, J.B. Cross, V. Bakken, C. Adamo, J. Jaramillo, R. Gomperts, R.E. Stratmann, O. Yazyev, A.J. Austin, R. Cammi, C. Pomelli, J.W. Ochterski, R.L. Martin, K. Morokuma, V.G. Zakrzewski, G.A. Voth, P. Salvador, J.J. Dannenberg, S. Dapprich, A.D. Daniels, Ö. Farkas, J.B. Foresman, J.V. Ortiz, J. Cioslowski, and D.J. Fox. Gaussian 09, Revision B.01. Gaussian, Inc., Wallingford CT, 2010.

[34] G. Karlström, R. Lindh, P.Å. Malmqvist, B.O. Roos, U. Ryde, V. Veryazov, P.O. Widmark, M. Cossi, B. Schimmelpfennig, P. Neogrady, and L. Seijo. MOLCAS: a program package for computational chemistry. *Comput. Mater. Sci.*, 28:222–229, 2003.

[35] F. Aquilante, L. De Vico, N. Ferré, G. Ghigo, P. Malmqvist, P. Neogrády, T.B. Pedersen, M. Pitoňák, M. Reiher, B.O. Roos, L. Serrano-Andrès, M. Urban, V. Veryazov, and R. Lindh. MOLCAS 7: the next generation. *J. Comput. Chem.*, 31:224–247, 2010.

[36] TURBOMOLE V5.7.1 2004, a development of University of Karlsruhe and Forschungszentrum Karlsruhe GmbH, 1989-2007, TURBOMOLE GmbH, since 2007; available from http://www.turbomole.com.

[37] E. Wigner. On the quantum correction for thermodynamic equilibrium. *Phys. Rev.*, 40:749–759, 1932.

21

[38] M. Barbatti, G. Granucci, M. Persico, M. Ruckenbauer, M. Vazdar, M. Eckert-Maksić, and H. Lischka. The on-the-fl surface-hopping program system Newton-X: Application to ab initio simulation of the nonadiabatic photodynamics of benchmark systems. *J. Photochem. Photobiol. A*, 190:228–240, 2007.

[39] G. Bussi, D. Donadio, and M. Parrinello. Canonical sampling through velocity rescaling. *J. Chem. Phys.*, 126:14101–14107, 2007.

[40] H.J.C. Berendsen, J.P.M. Postma, W.F. van Gunsteren, A. DiNola, and J.R. Haak. Molecular dynamics with coupling to an external bath. *J. Chem. Phys.*, 81:3684–3690, 1984.

[41] H.C. Andersen. Molecular dynamics simulations at constant pressure and/or temperature. *J. Chem. Phys.*, 72:2384–2393, 1980.

[42] S. Nose. A unifie formulation of the constant temperature molecular dynamics methods. *J. Chem. Phys.*, 81:511–519, 1984.

[43] W.G. Hoover. Canonical dynamics: Equilibrium phase-space distributions. *Phys. Rev. A*, 31:1695–1697, 1985.

[44] G.J. Martyna, M.L. Klein, and M. Tuckerman. Nose-Hoover chains: The canonical ensemble via continuous dynamics. *J. Chem. Phys.*, 97:2635–2643, 1992.

[45] T. Schneider and E. Stoll. Molecular-dynamics study of a three-dimensional one-component model for distortive phase transitions. *Phys. Rev. B*, 17:1302–1322, 1978.

[46] N. Otte, M. Scholten, and W. Thiel. Looking at Self-Consistent-Charge Density Functional Tight Binding from a Semiempirical Perspective. *J. Phys. Chem. A*, 111:5751–5755, 2007.

[47] M. Elstner, D. Porezag, G. Jungnickel, J. Elsner, M. Haugk, Th. Frauenheim, S. Suhai, and G. Seifert. Self-consistent-charge density-functional tight-binding method for simulations of complex materials properties. *Phys. Rev. B*, 58:7260–7268, 1998.

[48] Q. Cui, M. Elstner, E. Kaxiras, T. Frauenheim, and M. Karplus. A QM/MM Implementation of the Self-Consistent Charge Density Functional Tight Binding (SCC-DFTB) Method. *J. Phys. Chem. B*, 105:569–585, 2001.

[49] J.C. Tully. Molecular dynamics with electronic transitions. *J. Chem. Phys.*, 93:1061–1071, 1990.

[50] S. Hammes-Schiffer and J.C. Tully. Proton transfer in solution: Molecular dynamics with quantum transitions. *J. Chem. Phys.*, 101:4657–4667, 1994.

[51] E. Fabiano, T.W. Keal, and W. Thiel. Implementation of surface hopping molecular dynamics using semiempirical methods. *Chem. Phys.*, 349:334–347, 2008.

[52] T.W. Keal, M. Wanko, and W. Thiel. Assessment of semiempirical methods for the photoisomerisation of a protonated Schiff base. *Theor. Chem. Acc.*, 123:145–156, 2009.

[53] G. Granucci, M. Persico, and A. Zoccante. Including quantum decoherence in surface hopping. *J. Chem. Phys.*, 133:134111, 2010.

[54] A.L. Sobolewski and W. Domcke. Computational studies of the photophysics of hydrogen-bonded molecular systems. *J. Phys. Chem. A*, 111:11725–11735, 2007.

[55] Y. Nosenko, G. Wiosna-Sałyga, M. Kunitski, I. Petkova, A. Singh, W.J. Buma, R.P. Thummel, B. Brutschy, and J. Waluk. Proton transfer with a twist? Femtosecond Dynamics of 7-(2-pyridyl) indole in Condensed Phase and in Supersonic Jets. *Angew. Chem. Int. Ed.*, 47:6037–6040, 2008.

22

C. Photoswitching of Salicylidene Methylamine: A Theoretical Photodynamics Study

Lasse Spörkel, Joanna Jankowska and Walter Thiel

I carried out all calculations and performed the subsequent analysis. I wrote most parts of the manuscript. I created all included figures.

Photoswitching of Salicylidene Methylamine: A Theoretical Photodynamics Study

Lasse Spörkel,[†] Joanna Jankowska,[‡,§] and Walter Thiel*,[†]

[†]Max-Planck-Institut für Kohlenforschung, Kaiser-Wilhelm-Platz 1, 45470 Mülheim an der Ruhr, Germany

[‡]College of Inter-Faculty Individual Studies in Mathematics and Natural Sciences, University of Warsaw, 93 Zwirki i Wigury St., 02-089 Warsaw, Poland

[§]Faculty of Chemistry, University of Warsaw, 1 Pasteura St., 02-093 Warsaw, Poland

S *Supporting Information*

ABSTRACT: Photoswitching of simple photochromic molecules attracts substantial attention because of its possible role in future photon-driven molecular electronics. Here we model the full photoswitching cycle of a minimal photochromic Schiff base—salicylidene methylamine (SMA). We perform semiempirical nonadiabatic on-the-fly photodynamics simulations at the OM2/MRCI level and thoroughly analyze the structural time evolution and switching efficiency of the system. We also identify and examine in detail the crucial steps in the SMA photochemistry ruled by excited-state intramolecular proton transfer. The results place the investigated model aromatic Schiff base among the promising candidates for novel photoswitching molecular materials. Our study also shows the potential of the semiempirical multireference photodynamics simulations as a tool for early stage molecular photodevice design.
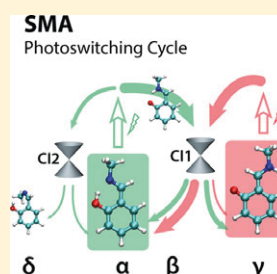
INTRODUCTION

Molecular photochromism and high photostability are among the crucial requirements for optically driven molecular memories, photoswitches, and data processing materials.[1−10] In this context special attention is paid to aromatic Schiff bases whose photochemistry is governed by an ultrafast excited-state intramolecular proton transfer (ESIPT).[11−18] In these molecules, the decay of the initially formed excited-state tautomer to the ground state can either lead back to the original species by proton transfer or trap a portion of the excited molecules in a ground-state metastable photochromic form. This opens prospects for applications in optically driven molecular devices.

Basic prerequisites for an efficient molecular photoswitch are the presence of at least two stable photochromic forms in the ground electronic state, lack of overlap between their absorption bands in the relevant excitation region, and radiationless decay routes from the Franck−Condon regions of both isomers leading to the other switching form. In the literature there are two main groups of chemical compounds investigated in the context of molecular photoswitching, which differ in their internal conversion mechanism: ring opening—ring closure versus cis−trans photoisomerization.[2,4,19] ESIPT-exhibiting aromatic Schiff bases introduce a novel way to optically driven switching control: here, the cis−trans photo-isomerization is enabled (at least from one side) by the initial excitation of an enol-form allowing for a chemical bond rearrangement through proton transfer (PT).

In recent years the photophysics of aromatic Schiff bases has been intensively studied both experimentally and theoretically, and much progress has been made toward an understanding of the underlying mechanisms. However, in the context of molecular photoswitching, there are still important questions to be answered. In this paper we investigate the photochemistry and photoswitching properties of an isolated molecule containing the minimal Schiff base chromophore—salicylidene methylamine (SMA).

Despite its simple structure, SMA has been studied less than other model aromatic Schiff bases, such as salicylidene aniline (SA) or larger systems of similar type.[17,20−25] From the experimental side, the enol-form of SMA has been identified as the most populated ground-state isomer, and the photochromic behavior observed in solution has been attributed to the formation of the keto-form. The available experimental data (absorption and transient absorption spectra recorded in some nonprotic solvents[26,27]) indicate that no fluorescence signal is found upon UV−vis excitation in the absorption band of the enol-form of SMA. Moreover, only a very weak emission is observed for lower-energy excitation in the absorption band of the keto-form. This suggests that SMA undergoes a barrierless ESIPT process followed by efficient nonradiative internal conversion to the electronic ground state. Theoretical investigations of SMA photophysics performed so far include static energy landscape calculations and wave packet photo-dynamics simulations of the ESIPT process.[16,28,29] These studies confirm barrierless PT in the first singlet excited state
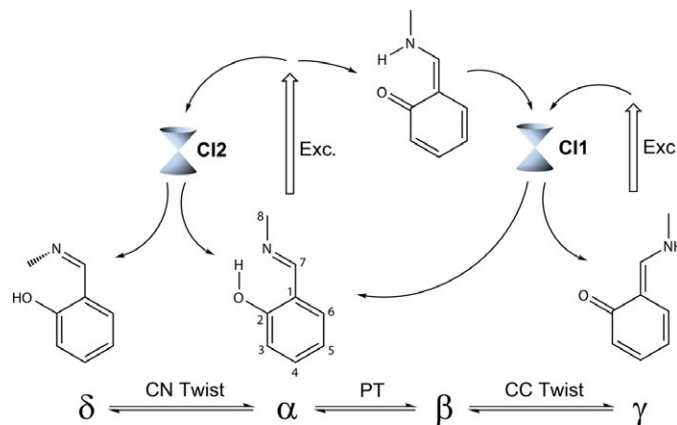
Figure 1. Chemical structures relevant for the photoswitching process and general scheme of the photochemistry of salicylidene methylamine.

Table 1. Relative Energies, Vertical Excitation Energies, and Important Geometrical Parameters for the Relevant Isomers and Conical Intersections of SMA Calculated with OM2/MRCI

	S_0 (kcal/mol)	S_1 (kcal/mol)	Vert. Exc. (eV)	OH (Å)	NH (Å)	$C_2C_1C_7N$ (deg)	$C_1C_7NC_8$ (deg)
α (S_0)	0.0	99.8	4.33	1.001	1.828	0.0	180.0
β (S_0)	5.6	75.3	3.02	1.649	1.047	0.0	180.0
γ (S_0)	11.4	87.1	3.28	4.674	1.013	180.0	180.0
δ (S_0)	6.8	112.6	4.59	0.995	2.693	60.3	0.4
α (S_1)	Relaxation to β (S_1)						
β (S_1)	13.3	68.0	2.37	1.696	1.039	0.0	180.0
γ (S_1)	22.0	76.4	2.36	4.604	1.018	180.0	180.0
δ (S_1)	Relaxation to CI2						
CI1	58.1	58.1	0.0	3.466	1.020	85.8	−153.7
CI2	60.2	60.2	0.0	0.997	1.961	5.4	90.9

of SMA and point to the presence of a conical intersection arising from CC double bond rotation as the main route for radiationless decay to the ground state.

In this work we present results of semiempirical on-the-fly photodynamics simulations for the two SMA tautomers relevant to photoswitching: the global minimum enol-form and the photochromic keto-form (denoted later as α and γ; for chemical structures see Figure 1). Our main goal is to investigate the full switching cycle and to determine the characteristic time scales and photoproduct distributions of both the forward and back switching transformations.

COMPUTATIONAL METHODS

The semiempirical calculations were performed using the OM2/MRCI method,[30−32] as implemented in the MNDO99 code.[33] During dynamics simulations, all required energies, gradients and nonadiabatic coupling elements were computed analytically.

The half-electron restricted open-shell Hartree−Fock (HF) formalism[34] was applied in the self-consistent field (SCF) treatment (i.e., the orbitals were optimized for the leading configuration of the S_1 state with two singly occupied orbitals). The active space in the multireference configuration interaction (MRCI) calculations included 10 electrons in 10 orbitals (see the Supporting Information for plots of these orbitals). In terms of the SCF configuration, it comprised the four highest doubly occupied orbitals, the two singly occupied orbitals, and the four lowest unoccupied orbitals. Three configuration state functions

were chosen as references for the MRCI treatment, namely the SCF configuration and the two closed-shell configurations derived therefrom (i.e., all singlet configurations that can be generated from the HOMO and LUMO of the closed-shell ground state). The MRCI wave function was built by allowing all single and double excitations from these three references. This semiempirical OM2/MRCI approach has been recently shown to perform well in a comprehensive general evaluation of excited-state properties[35] and in a number of recent excited-state studies.[25,36−48]

In trajectory surface-hopping dynamics the initial conditions are usually generated by Wigner sampling,[49,50] which defines initial coordinates and velocities based on classical or quantum harmonic vibrational modes, or by employing canonical classical molecular dynamics (MD) simulations, in which the canonical distribution is satisfied with the use of a thermostat. Here, we adopted the second approach applying the Nose-Hoover chains algorithm[51] (with a chain length of 10) for thermostatting. We used the default characteristic time of 0.01 ps for the thermostat and a time step of 1 fs for nuclear motion.

For both target molecules (α and γ isomers), ground-state MD runs were performed at the SCC-DFTB level.[52−54] 4 ps of equilibration dynamics were followed by a 100 ps production run, from which 600 initial atomic coordinates and velocities were randomly selected for each molecule. The starting points for the subsequent OM2/MRCI nonadiabatic dynamics were chosen from this set on the basis of the computed S_0 to S_1 transition probabilities and the vertical excitation energies. The
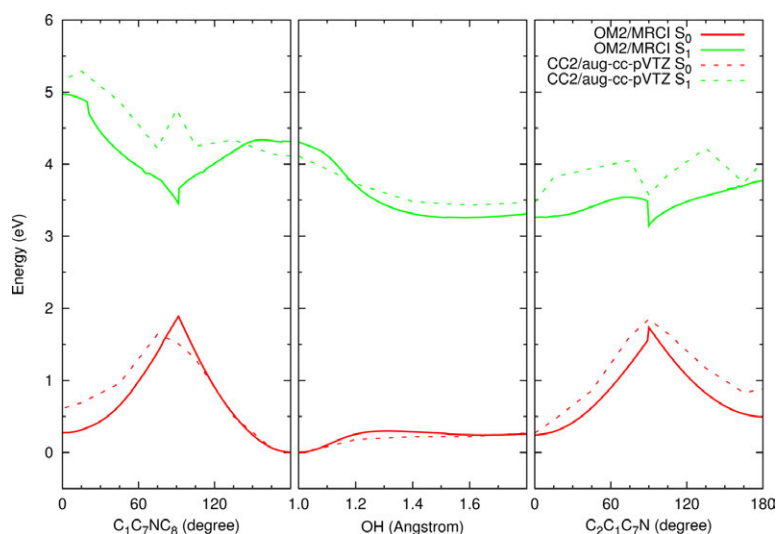
93

Figure 2. Vertical energy profiles for SMA calculated at the OM2/MRCI and CC2/aug-cc-pVTZ[29] levels (see text).

thermostat was switched off during the excited-state dynamics. A total of 321 surface-hopping trajectories for the α isomer and 333 for the γ isomer were run up to 1 ps with all relevant energies, gradients, and nonadiabatic coupling vectors being computed on-the-fly as needed.

For points with an $S_1 - S_0$ energy gap of less than 10 kcal/mol, the fewest-switches criterion was applied to decide whether to hop.[55,56] The time step was chosen to be 0.2 fs for nuclear motion and 0.0005 fs for electronic propagation. The unitary propagator evaluated at the middle point was used to propagate electronic motion.[57,58] Translational and rotational motions were removed in each step. The empirical decoherence correction (0.1 au) proposed by Granucci et al. was employed.[59] The final evaluations were done for the 259 α and 306 γ trajectories that finished successfully and satisfied our energy continuity criterion (no changes greater than 30 kcal/mol between any two consecutive MD steps). The SCC-DFTB sampling with the Nose-Hoover chains technique was done with ChemShell 3.4[60,61] and the nonadiabatic OM2/MRCI dynamics simulations were conducted with MNDO99.[33]

VALIDATION: STATIC CALCULATIONS

For specific validation of the OM2/MRCI method for SMA, the relevant isomers (see Figure 1) were optimized in the ground and first excited states. The two previously found S_1/S_0 conical intersections[29] were also located at the OM2/MRCI level. Table 1 lists the computed energies and selected geometrical parameters. The first excited state is always of $\pi\pi^*$ character in the OM2/MRCI calculations. For full geometrical structures and corresponding ab initio results see the Supporting Information (SI).

The OM2/MRCI results are consistent with the previously calculated energy landscape.[16,29] In the ground state the α conformer is confirmed to be the most stable form and all other isomers, except for δ, are found to be planar — as indicated by the given dihedral angles. In the first singlet excited state the α isomer does not correspond to a minimum but transfers the OH proton to the N atom upon geometry optimization,

forming the β isomer in a barrierless ESIPT process. In the course of the excited-state optimization the δ conformer relaxes to the CI2 conical intersection. The calculated vertical excitation energies to the S_1 state are reasonably close to the published values obtained from high-quality ab initio methods (CC2/aug-cc-pVTZ on MP2/cc-pVDZ geometries),[29] which are documented in the Supporting Information for easy reference.

For further validation, vertical potential energy profiles were calculated at the OM2/MRCI level and compared with corresponding ab initio data.[29] The profiles were computed for the variation of three geometrical parameters most relevant to SMA photochemistry: the $C_1C_7NC_8$ dihedral angle relating isomers α and δ (denoted as CN from now on), the OH distance relating isomers α and β, and the $C_2C_1C_7N$ dihedral angle relating isomers β and γ (denoted as CC from now on). For each point on the profile, the corresponding parameter was constrained to a fixed value and a full ground-state optimization was carried out for all other degrees of freedom. The energy of the first excited state was then obtained from a single-point calculation. The computed profiles are presented in Figure 2. The profiles obtained from the semiempirical OM2/MRCI calculations and from single-point ab initio CC2/aug-cc-pVTZ calculations on MP2/cc-pVDZ geometries are very similar to each other and agree with regard to all important features pertinent to SMA photochemistry. In particular, they show a barrierless proton transfer path in the first excited state and exhibit only very small barriers for the excited-state deactivation via CI1 and for the ground-state proton back transfer. The small bumps in the regions near the conical intersections are due to minor sudden changes in the optimized geometries.

DYNAMICS SIMULATIONS

Excited-state decay. After vertical excitation to the first singlet excited state, both the α enol-form and the γ keto-form of SMA undergo an ultrafast deactivation to the ground state. In both cases this process is usually finished after less than 300 fs. The average state populations during the α and γ
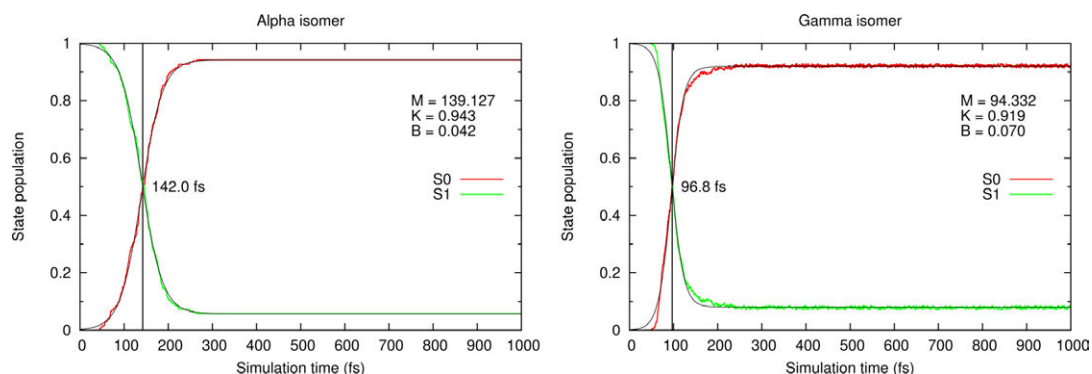
Figure 3. Average state populations for the two sets of trajectories (left: α isomer; right: γ isomer). The parameters of the sigmoidal fitting function are specified in the plots.
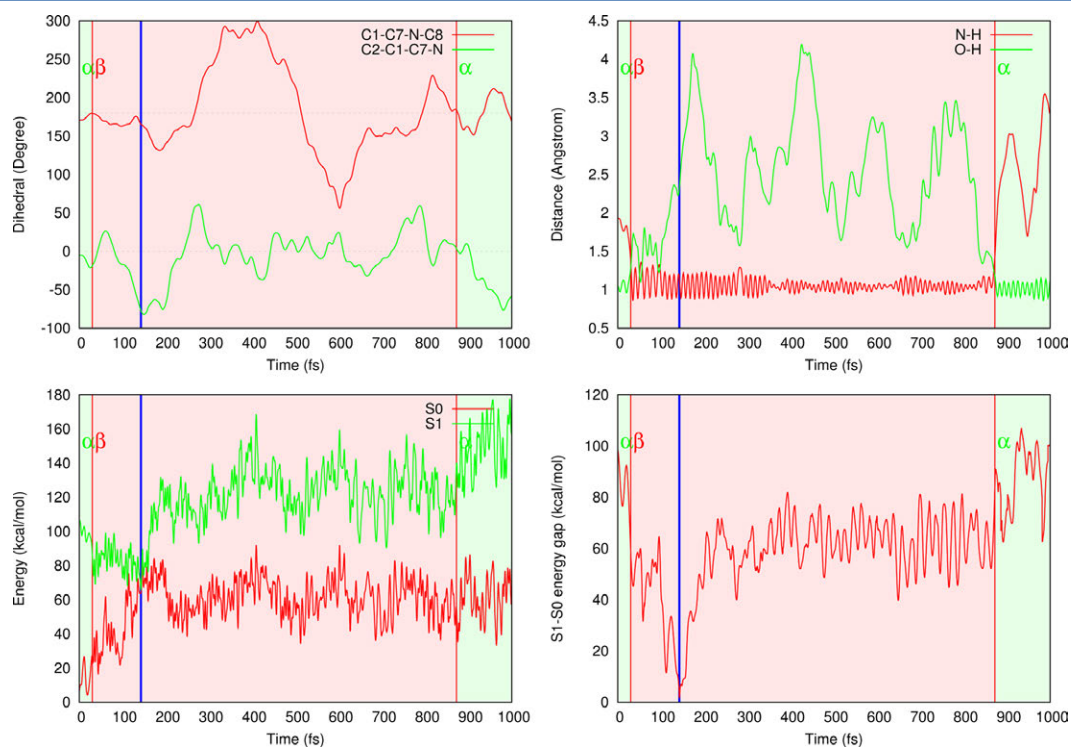

Figure 4. Different properties vs simulation time of a typical trajectory for the α isomer. Top left: dihedrals, horizontal dashed lines mark multiples of 180°; top right: distances; bottom left: state energies; bottom right: energy difference.

photodynamics are plotted in Figure 3 against the simulation time. The data are fitted by a sigmoid function (see eq 1) which provides an approximate decay time. The lifetime of the excited state is defined as the point at which half of the trajectories have decayed to the ground state. It is marked in the plots with a vertical line. The parameter K denotes the fraction of trajectories that decay until the end of the simulation.

$$f(x) = \frac{K}{1 + e^{-B(x-M)}} \tag{1}$$

The deactivation of the α isomer may be realized through two different phototransformations − (i) the ESIPT process followed by CC bond twist or (ii) the photoisomerization around the CN bond (direct cis−trans transformation). This deactivation proceeds at an average time scale of ca. 150 fs which makes it slower by around 50 fs in comparison with the excited-state decay of the γ form (see Figure 3). Within the total simulation time of 1 ps, the internal conversion to the ground state is very efficient for both SMA forms—less than 6% (9%) of the trajectories are left in the excited state for the α (γ)
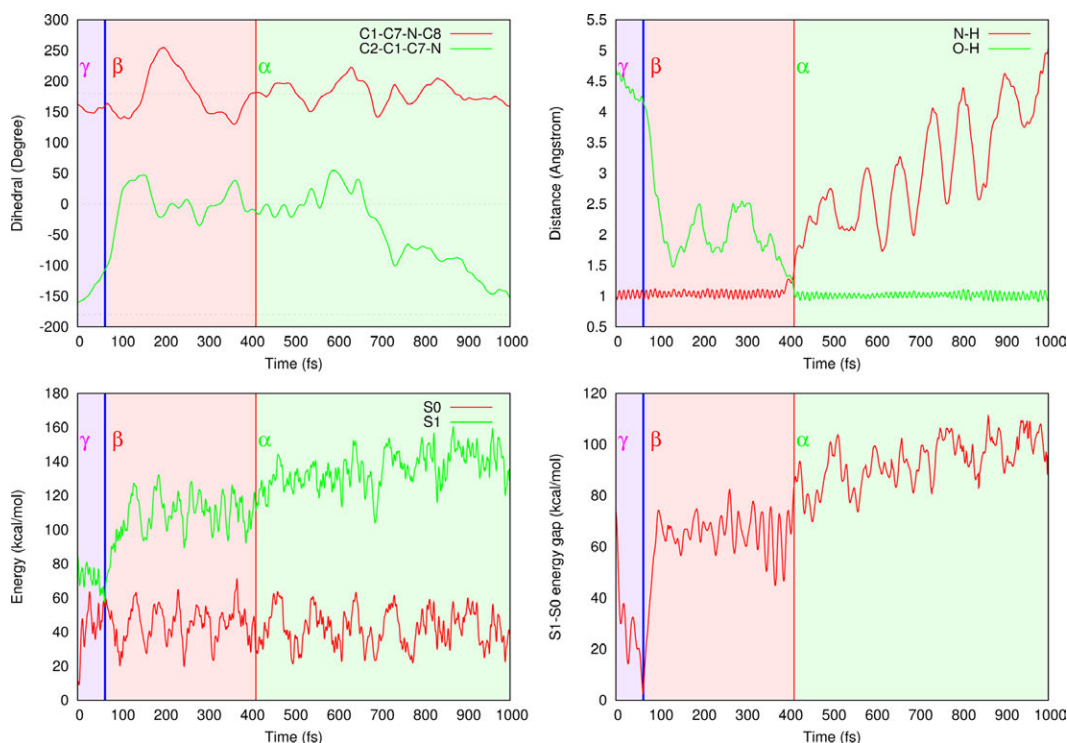
95

Article

Figure 5. Different properties vs simulation time of a typical trajectory for the γ isomer. Top left: dihedrals, horizontal dashed lines mark multiples of 180°; top right: distances; bottom left: state energies; bottom right: energy difference.

photodynamics, respectively. The slightly higher number of such trajectories in the γ case may be attributed to the very flat shape of the S_1 potential energy surface (PES) in the Franck–Condon region and the lack of excess kinetic energy from ESIPT (compared with the α case).

Typical trajectories. Figure 4 and Figure 5 show the time evolution of key parameters characterizing the photodynamical trajectories of the α and γ isomers, respectively. The plots for the two sample runs include: the dihedral angle of CC and CN rotations, the OH and NH distances, the S_0 and S_1 energies relative to the global ground-state minimum of the α isomer, and the energy gap between these two states. Blue vertical lines mark the hopping events between the two energy surfaces, while the red lines indicate an intramolecular proton transfer. To facilitate the analysis of the graphs, the geometrical structures present at each stage of the dynamics are indicated by a corresponding label (i.e., α, β, γ, or δ).

Figure 4 shows a trajectory starting from the α isomer. After photoexcitation occurs an ultrafast proton transfer to the N atom (finished within 30 fs) accompanied by a clear reduction of the S_1/S_0 energy gap. A subsequent rotational motion takes the system toward the CI1 conical intersection, where it hops to the ground state at a simulation time of ca. 150 fs. This is followed by torsional oscillations around the CN bond (for ca. 700 fs); CC rotation is not feasible in the ground state, because during $S_1 \rightarrow S_0$ deactivation the π^* orbital localized at the CC bond becomes unoccupied and thus the energy barrier for CC rotation rises significantly. The ground-state proton transfer

from the nitrogen back to the oxygen atom then occurs at ca. 850 fs, regenerating the α isomer and restoring the interstate energy gap to its initial value. At this point, further CN rotation is also suppressed.

The trajectory starting from the γ isomer in Figure 5 shows a faster, single-step deactivation involving only CC bond rotation (there is no need for ESIPT to open the route toward the CI). The system hops to the ground state at ca. 70 fs and thereafter exhibits a similar behavior as on the previously discussed α trajectory. A difference between the two α and γ simulations can be seen in the OH and NH stretching amplitudes, which should be associated with the ease of proton back transfer in the ground state. After roaming on the S_0 PES in the vicinity of the β isomer for ca. 350 fs, the proton is transferred from the N back to the O atom, and the system ends up in the α form. These transformations are again accompanied by characteristic energy gap changes.

Structure population analysis. In line with a previously proposed scheme,[29] we have analyzed the SMA isomers observed during the dynamics simulations in terms of photochemical classes. Depending on the values of the three key internal degrees of freedom (CN dihedral, CC dihedral, and OH distance) we assign the starting, hopping, and final structures from each trajectory to the α, β, γ, or δ sets (for precise class definitions see the Supporting Information). Within one particular photochemical class all SMA conformers are interconvertible by rotations around single bonds that usually require only little energy. All class members have similar
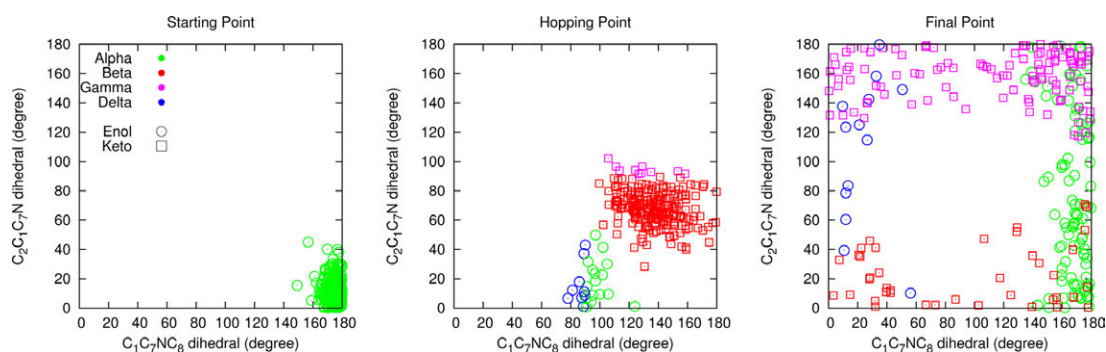
Figure 6. Dihedral angle distribution of key structures in the trajectories starting from the α isomer. Color code for assignment to isomers: green — α; red — β; violet — γ; blue — δ.
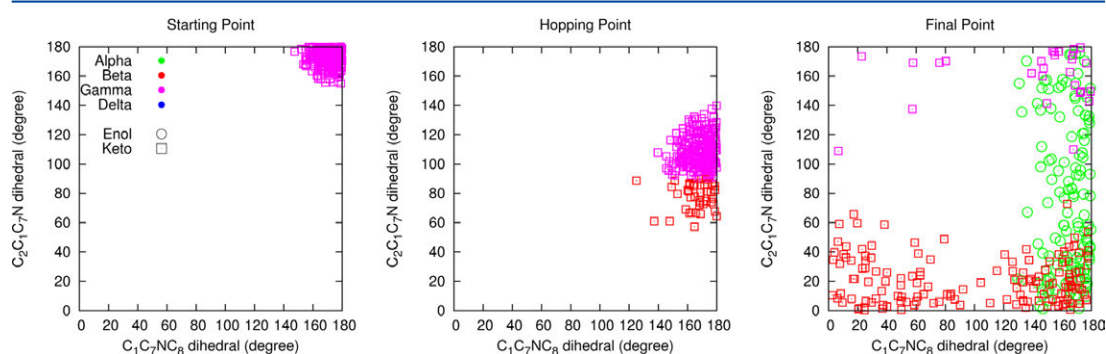

Figure 7. Dihedral angle distribution of key structures in the trajectories starting from the γ isomer. Color code for assignment to isomers: green — α; red — β; violet — γ; blue — δ.

UV absorption spectra which are, however, distinct from those of different-class representatives.

Figure 6 shows results of such a structure population analysis for the α photodynamics. At the starting point, the two key dihedral angles do not differ much from the optimum values of 0 and 180 of the initial α isomer (left panel). By contrast, the hopping points (middle panel) have twisted structures, with at least one of the two key dihedral angles differing strongly from 0 and 180°. These hopping points are concentrated in two areas: CC ≈ 90° and CN ∈ [120° −160°] and CN ≈ 90° and CC ∈ [0° − 30°]. This reflects the competition between two internal conversion pathways proceeding through the CI1 and CI2 conical intersections. The first one, involving ESIPT followed by CC bond rotation, happens much more frequently than the second one, involving CN bond photoisomerization (ca. 9:1 probability ratio). This is plausible because the path from the Franck−Condon point to CI1 is essentially barrierless and initiated by the ultrafast ESIPT process, while at the same time there is a small barrier on the route to the alternative CI2 conical intersection. In the right panel with the final structures (final points of the simulation) one finds all possible isomers in an α:β:γ:δ photoproduct distribution of ca. 7:3:9:1. Evidently, the switching forms — α and γ — are strongly preferred over the other two structures. The small amount of the δ form represents the photoproducts of the alternative deactivation mechanism via CI2. On a somewhat longer time scale, the initially produced β isomers are expected to undergo a nearly

barrierless ground-state proton back transfer transforming them into the α photochemical class. The collected data also allow an estimate of the splitting ratio at both conical intersections. Comparing the overall number of final structures classified as α and β that arise from hopping around CI1 with the number of final γ isomers, one gets a 1:1 ratio. An analogous analysis for the CI2 conical intersection (involving the δ and α structures coming from the deactivation at CI2) also gives a 1:1 ratio.

The corresponding results for the γ isomer are shown in Figure 7. Again, the trajectories start in the vicinity of the initial minimum (left panel). All the hopping points lie close to the CI1 conical intersection (middle panel). They are reached from the Franck−Condon region of the γ isomer by CC bond rotation (note that CI2 cannot be accessed from the γ structure). At the end of the simulation (right panel) most of the trajectories end up as α or β isomers, with a photoproduct distribution α:β:γ:δ of ca. 4:5:1:0. Thus, the overall splitting ratio estimated for CI1 equals 9:1 for the γ photodynamics.

The product distribution in the two photodynamics simulations gives valuable information about the expected photoswitching efficiency — the extent of the initial-to-final transformation at the end of the simulation may be considered as one of its possible measures. Comparison of the α:β:γ:δ ratio for the onward (α photodynamics) and backward (γ photo-dynamics) switching shows better performance of the latter. The initial-to-final conversion (counting the β population as future α class) amounts to 50% for the $\alpha \rightarrow \gamma$ and to 90% for
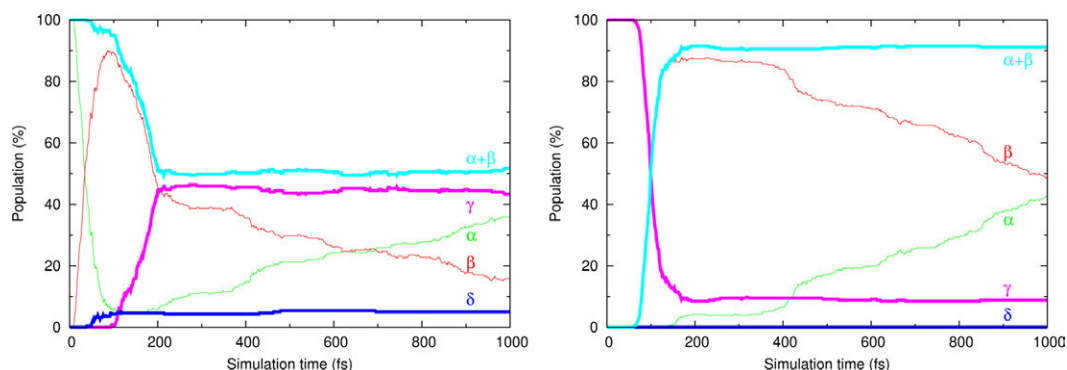
Figure 8. Abundance of the different product isomers plotted against simulation time. Color code for the isomers: green $-\alpha$; red $-\beta$; cyan $-\alpha+\beta$; violet $-\gamma$; blue $-\delta$.

the $\gamma \rightarrow \alpha$ phototransformation. These percentages almost perfectly reflect the splitting ratio at CI1 — the conical intersection responsible for the dominant internal conversion mechanism in SMA. Therefore, it is worthwhile to focus attention on the structural bifurcation at CI1. The splitting ratio may be explained in terms of the interplay between the effects of *momentum conservation* and *coupling to the local density of states*. The first factor, understood as favorable continuation of the rotational motion driving the system to a conical intersection, always supports direct passing through the CI and, thus, the photoswitching. The second one, a purely quantum effect, enters the dynamics through vibrational mode relaxation that occurs after the hop to the ground state. This vibrational cooling is more efficient for the more pronounced (deeper and/or wider) of the minima adjacent to the splitting CI point, which in our case is the α isomer. One should notice that in the α photodynamics these two effects act against each other leading to a rather even splitting distribution, while in the γ case they act in the same direction and thus favor formation of the α isomer.

Figure 8 shows the time evolution of the photochemical class populations for both photodynamics: α — left panel and γ — right panel. After excitation of the α form, one observes an ultrafast α to β transformation (ESIPT) occurring mainly in the first 30 fs of the simulation; this is in very good agreement with previous theoretical results[16] and with experimental findings for similar systems.[62] Slightly later, ca. 50 fs after the excitation, the population of the δ form starts to grow which, after rising to a 5% value, stays constant until the simulation ends. This confirms, as expected, that in the S_1 state an intramolecular ballistic transfer of a light proton occurs faster than a rotation around the CN bond. Consequently, the internal conversion through CI1 plays a predominant role in SMA photodynamics. Further analysis of the left panel of Figure 8 (100 fs $< t <$ 200 fs) shows that the β population, after reaching its maximum arising from the ESIPT process, decreases rapidly. At the same time (starting ca. 70 fs after the PT) the amount of γ isomer starts to grow with a similar rate. This reflects the internal conversion process with a bifurcation between the β and γ forms and is consistent with the previously estimated S_1 excited-state lifetime. After 200 fs the γ population stabilizes at its final value, and one observes an almost linear decrease (increase) in the population of the β (α) isomer, which continues until the end of the 1 ps simulation. Assuming this

trend to continue, the full switching process would be finished around 1.6 ps after the initial photoexcitation of the α isomer, which is again in agreement with experimental observations for analogous Schiff base systems.[62]

From the right panel of Figure 8 one may learn about the time characteristics of the back-switching process starting with an excitation of the γ form. At the very beginning the system stays close to the initial structure and then, again after ca. 70 fs, the γ to β transformation starts. This happens through internal conversion at CI1 with bifurcation between these two forms, similarly as in the previously discussed α photodynamics. Population of the β isomer initializes the subsequent β to α transformation, which again proceeds almost linearly with time. Concomitantly, the γ population reached after the S_1 to S_0 deactivation remains constant, and no traces of the δ form are observed. In analogy to the analysis for the α case, the overall γ switching time scale may be estimated as ca. 2.0 ps.

CONCLUSION

In this paper we investigated the full photoswitching cycle of an isolated SMA molecule by means of the semiempirical on-the-fly photodynamics simulations. For the two isomers that play a crucial role in the switching (α and γ), we find a very efficient internal conversion ($\sim$90% nonradiative decay of the excited state) that indicates excellent photostability and promising switching efficiency of SMA. The computed time scales characterizing the crucial phototransformations of this model Schiff base system are all in the ultrafast regime ($\sim$1 ps and subpicosecond). The simulations predict that the switching process is reversible in SMA and that the competing photoisomerization around the CN bond plays only a minor role in the photochemistry of this system. The detailed analysis of structural time evolution provides direct insight into the internal conversion and switching mechanisms. The strong dependence of the splitting ratio at the CI1 conical intersection on the photoswitching direction probably originates from the ground-state PES topology of the α and γ switching forms.

The ESIPT-based photoswitching mechanism in SMA involves pronounced reorganization of the electron density accompanied by only minor changes in its geometrical structure. This should allow for switching selectivity due to the strong photochromism and should also ensure structural stability, which are both important factors in the design of molecular electronics devices. In summary, we believe that

aromatic Schiff bases may have advantages over many previously proposed molecular photoswitching systems because of their ultrafast photochemistry, high photostability, and good excitation selectivity, and that they may thus be considered as promising candidates for future photodriven molecular electronics materials.

■ ASSOCIATED CONTENT

ⓢ Supporting Information

Active space for OM2/MRCI calculations, ab initio relative energies, definition of SMA photochemical classes, and optimized Cartesian coordinates. This material is available free of charge via the Internet at http://pubs.acs.org.

■ AUTHOR INFORMATION

Corresponding Author

*E-mail: thiel@kofo.mpg.de.

Notes

The authors declare no competing financial interest.

■ ACKNOWLEDGMENTS

■ REFERENCES

(1) Yokoyama, Y. Fulgides for Memories and Switches. *Chem. Rev.* **2000**, *100*, 1717−1739.

(2) Irie, M. Diarylethenes for Memories and Switches. *Chem. Rev.* **2000**, *100*, 1685−1716.

(3) Berkovic, G.; Krongauz, V.; Weiss, V. Spiropyrans and Spirooxazines for Memories and Switches. *Chem. Rev.* **2000**, *100*, 1741−1754.

(4) Tian, H.; Yang, S. Recent progresses on diarylethene based photochromic switches. *Chem. Soc. Rev.* **2004**, *33*, 85−97.

(5) Beharry, A. A.; Woolley, G. A. Azobenzene photoswitches for biomolecules. *Chem. Soc. Rev.* **2011**, *40*, 4422−4437.

(6) Feringa, B. L.; van Delden, R. A.; Koumura, N.; Geertsema, E. M. Chiroptical Molecular Switches. *Chem. Rev.* **2000**, *100*, 1789−1816.

(7) Feringa, B. L.; Browne, W. R. *Molecular Switches*; Wiley-VCH Verlag GmbH & Co. KGaA: Weinheim, 2011.

(8) Kawata, S.; Kawata, Y. Three-Dimensional Optical Data Storage Using Photochromic Materials. *Chem. Rev.* **2000**, *100*, 1777−1788.

(9) Wuttig, M.; Yamada, N. Phase-change materials for rewriteable data storage. *Nat. Mater.* **2007**, *6*, 824−832.

(10) Raymo, F. M.; Giordani, S. All-optical processing with molecular switches. *Proc. Natl. Acad. Sci. U. S. A.* **2002**, *99*, 4941−4944.

(11) Sobolewski, A. L. Reversible molecular switch driven by excited-state hydrogen transfer. *Phys. Chem. Chem. Phys.* **2008**, *10*, 1243−1247.

(12) Łapiński, L.; Nowak, M. J.; Nowacki, J.; Rode, M. F.; Sobolewski, A. L. A Bistable Molecular Switch Driven by Photo-induced Hydrogen-Atom Transfer. *ChemPhysChem* **2009**, *10*, 2290−2295.

(13) Hadjoudis, E.; Mavridis, I. M. Photochromism and thermochromism of Schiff bases in the solid state: structural aspects. *Chem. Soc. Rev.* **2004**, *33*, 579−588.

(14) Sobolewski, A. L.; Domcke, W.; Hättig, C. Photophysics of Organic Photostabilizers. Ab Initio Study of the Excited-State

(15) Sobolewski, A.; Domcke, W. Computational studies of the photophysics of hydrogen-bonded molecular systems. *J. Phys. Chem. A* **2007**, *111*, 11725−11735.

(16) Ortiz-Sánchez, J. M.; Gelabert, R.; Moreno, M.; Lluch, J. M. Theoretical Study on the Excited-State Intramolecular Proton Transfer in the Aromatic Schiff Base Salicylidene Methylamine: an Electronic Structure and Quantum Dynamical Approach. *J. Phys. Chem. A* **2006**, *110*, 4649−4656.

(17) Ortiz-Sánchez, J. M.; Gelabert, R.; Moreno, M.; Lluch, J. M. Electronic-structure and quantum dynamical study of the photochromism of the aromatic Schiff base salicylideneaniline. *J. Chem. Phys.* **2008**, *129*, 214308.

(18) Migani, A.; Blancafort, L.; Robb, M. A.; DeBellis, A. D. An Extended Conical Intersection Seam Associated with a Manifold of Decay Paths: Excited-State Intramolecular Proton Transfer in o-Hydroxybenzaldehyde. *J. Am. Chem. Soc.* **2008**, *130*, 6932−6933.

(19) Szymański, W.; Beierle, J. M.; Kistemaker, H. A. V.; Velema, W. A.; Feringa, B. L. Reversible Photocontrol of Biological Systems by the Incorporation of Molecular Photoswitches. *Chem. Rev.* **2013**, *113*, 6114−6178.

(20) Otsubo, N.; Okabe, C.; Mori, H.; Sakota, K.; Amimoto, K.; Kawato, T.; Sekiya, H. Excited-state intramolecular proton transfer in photochromic jet-cooled salicylideneaniline. *J. Photochem. Photobiol., A* **2002**, *154*, 33−39.

(21) Mitra, S.; Tamai, N. Dynamics of photochromism in salicylideneaniline: A femtosecond spectroscopic study. *Phys. Chem. Chem. Phys.* **2003**, *5*, 4647−4652.

(22) Ziółek, M.; Kubicki, J.; Maciejewski, A.; Naskręcki, R.; Grabowska, A. An ultrafast excited state intramolecular proton transfer (ESPIT) and photochromism of salicylideneaniline (SA) and its "double" analogue salicylaldehyde azine (SAA). A controversial case. *Phys. Chem. Chem. Phys.* **2004**, *6*, 4682−4689.

(23) Okabe, C.; Nakabayashi, T.; Inokuchi, Y.; Nishi, N.; Sekiya, H. Ultrafast excited-state dynamics in photochromic N-salicylideneaniline studied by femtosecond time-resolved REMPI spectroscopy. *J. Chem. Phys.* **2004**, *121*, 9436−9442.

(24) Sliwa, M.; Mouton, N.; Ruckebusch, C.; Poisson, L.; Idrissi, A.; Alose, S.; Potier, L.; Dubois, J.; Poizat, O.; Buntinx, G. Investigation of ultrafast photoinduced processes for salicylidene aniline in solution and gas phase: toward a general photo-dynamical scheme. *Photochem. Photobiol. Sci.* **2010**, *9*, 661−669.

(25) Spörkel, L.; Cui, G.; Thiel, W. Photodynamics of Schiff Base Salicylideneaniline: Trajectory Surface-Hopping Simulations. *J. Phys. Chem. A* **2013**, *117*, 4574−4583.

(26) Zgierski, M. Z.; Grabowska, A. Theoretical approach to photochromism of aromatic Schiff bases: A minimal chromophore salicylidene methylamine. *J. Chem. Phys.* **2000**, *113*, 7845−7852.

(27) Knyazhansky, M.; Metelitsa, A.; Kletskii, M.; Millov, A.; Besugliy, S. The structural transformations and photo-induced processes in salicylidene alkylimines. *J. Mol. Struct.* **2000**, *526*, 65−79.

(28) Grabowska, A.; Kownacki, K. Structural aspects of photochromism of the internally H-bonded Schiff bases. "A minimal chromophore". *Acta Phys. Polym., A* **1995**, *88*, 1081−1088.

(29) Jankowska, J.; Rode, M. F.; Sadlej, J.; Sobolewski, A. L. Photophysics of Schiff Bases: Theoretical Study of Salicylidene Methylamine. *ChemPhysChem* **2012**, *13*, 4287−4294.

(30) Weber, W. Ph.D. Thesis, University of Zürich, 1996.

(31) Weber, W.; Thiel, W. Orthogonalization corrections for semiempirical methods. *Theor. Chem. Acc.* **2000**, *103*, 495−506.

(32) Koslowski, A.; Beck, M.; Thiel, W. Implementation of a general multireference configuration interaction procedure with analytic gradients in a semiempirical context using the graphical unitary group approach. *J. Comput. Chem.* **2003**, *24*, 714−726.

(33) Thiel, W. *MNDO99 program*, version 6.1. 2007; Max-Planck-Institut für Kohlenforschung: Mülheim, Germany, 2007.

2709

dx.doi.org/10.1021/jp5095678 | *J. Phys. Chem. B* 2015, 119, 2702−2710

99

(34) Dewar, M. J. S.; Hashmall, J. A.; Venier, C. G. Ground states of conjugated molecules. IX. Hydrocarbon radicals and radical ions. *J. Am. Chem. Soc.* **1968**, *90*, 1953−1957.

(35) Silva-Junior, M.; Thiel, W. Benchmark of Electronically Excited States for Semiempirical Methods: MNDO, AM1, PM3, OM1, OM2, OM3, INDO/S, and INDO/S2. *J. Chem. Theory Comput.* **2010**, *6*, 1546−1564.

(36) Fabiano, E.; Thiel, W. Nonradiative deexcitation dynamics of 9H-adenine: An OM2 surface hopping study. *J. Phys. Chem. A* **2008**, *112*, 6859−6863.

(37) Lan, Z.; Fabiano, E.; Thiel, W. Photoinduced Nonadiabatic Dynamics of Pyrimidine Nucleobases: On-the-Fly Surface-Hopping Study with Semiempirical Methods. *J. Phys. Chem. B* **2009**, *113*, 3548−3555.

(38) Lan, Z.; Fabiano, E.; Thiel, W. Photoinduced Nonadiabatic Dynamics of 9H-Guanine. *ChemPhysChem* **2009**, *10*, 1225−1229.

(39) Lan, Z.; Lu, Y.; Fabiano, E.; Thiel, W. QM/MM Nonadiabatic Decay Dynamics of 9H-Adenine in Aqueous Solution. *ChemPhysChem* **2011**, *12*, 1989−1998.

(40) Lu, Y.; Lan, Z.; Thiel, W. Hydrogen Bonding Regulates the Monomeric Nonradiative Decay of Adenine in DNA Strands. *Angew. Chem., Int. Ed.* **2011**, *50*, 6864−6867.

(41) Weingart, O.; Lan, Z.; Koslowski, A.; Thiel, W. Chiral Pathways and Periodic Decay in cis-Azobenzene Photodynamics. *J. Phys. Chem. Lett.* **2011**, *2*, 1506−1509.

(42) Kazaryan, A.; Lan, Z.; Schäfer, L.; Thiel, W.; Filatov, M. Surface Hopping Excited-State Dynamics Study of the Photoisomerization of a Light-Driven Fluorene Molecular Rotary Motor. *J. Chem. Theory Comput.* **2011**, *7*, 2189−2199.

(43) Lan, Z.; Lu, Y.; Weingart, O.; Thiel, W. Nonadiabatic Decay Dynamics of a Benzylidene Malononitrile. *J. Phys. Chem. A* **2012**, *116*, 1510−1518.

(44) Lu, Y.; Lan, Z.; Thiel, W. Monomeric adenine decay dynamics influenced by the DNA environment. *J. Comput. Chem.* **2012**, *33*, 1225−1235.

(45) Cui, G.; Lan, Z.; Thiel, W. Intramolecular hydrogen bonding plays a crucial role in the photophysics and photochemistry of the GFP chromophore. *J. Am. Chem. Soc.* **2012**, *134*, 1662−1672.

(46) Cui, G.; Thiel, W. Nonadiabatic dynamics of a truncated indigo model. *Phys. Chem. Chem. Phys.* **2012**, *14*, 12378−12384.

(47) Cui, G.; Thiel, W. Photoinduced Ultrafast Wolff Rearrangement: A Non-Adiabatic Dynamics Perspective. *Angew. Chem., Int. Ed.* **2013**, *52*, 433−436.

(48) Spörkel, L.; Cui, G.; Koslowski, A.; Thiel, W. Nonequilibrium H/D Isotope Effects from Trajectory-Based Nonadiabatic Dynamics. *J. Phys. Chem. A* **2014**, *118*, 152−157.

(49) Wigner, E. On the quantum correction for thermodynamic equilibrium. *Phys. Rev.* **1932**, *40*, 749−759.

(50) Barbatti, M.; Granucci, G.; Persico, M.; Ruckenbauer, M.; Vazdar, M.; Eckert-Maksić, M.; Lischka, H. The on-the-fly surface-hopping program system Newton-X: Application to ab initio simulation of the nonadiabatic photodynamics of benchmark systems. *J. Photochem. Photobiol., A* **2007**, *190*, 228−240.

(51) Martyna, G.; Klein, M.; Tuckerman, M. Nose-Hoover chains: The canonical ensemble via continuous dynamics. *J. Chem. Phys.* **1992**, *97*, 2635−2643.

(52) Otte, N.; Scholten, M.; Thiel, W. Looking at Self-Consistent-Charge Density Functional Tight Binding from a Semiempirical Perspective. *J. Phys. Chem. A* **2007**, *111*, 5751−5755.

(53) Elstner, M.; Porezag, D.; Jungnickel, G.; Elsner, J.; Haugk, M.; Frauenheim, T.; Suhai, S.; Seifert, G. Self-consistent-charge density-functional tight-binding method for simulations of complex materials properties. *Phys. Rev. B* **1998**, *58*, 7260−7268.

(54) Cui, Q.; Elstner, M.; Kaxiras, E.; Frauenheim, T.; Karplus, M. A QM/MM Implementation of the Self-Consistent Charge Density Functional Tight Binding (SCC-DFTB) Method. *J. Phys. Chem. B* **2001**, *105*, 569−585.

(55) Tully, J. Molecular dynamics with electronic transitions. *J. Chem. Phys.* **1990**, *93*, 1061−1071.

(56) Hammes-Schiffer, S.; Tully, J. Proton transfer in solution: Molecular dynamics with quantum transitions. *J. Chem. Phys.* **1994**, *101*, 4657−4667.

(57) Fabiano, E.; Keal, T.; Thiel, W. Implementation of surface hopping molecular dynamics using semiempirical methods. *Chem. Phys.* **2008**, *349*, 334−347.

(58) Keal, T.; Wanko, M.; Thiel, W. Assessment of semiempirical methods for the photoisomerisation of a protonated Schiff base. *Theor. Chem. Acc.* **2009**, *123*, 145−156.

(59) Granucci, G.; Persico, M.; Zoccante, A. Including quantum decoherence in surface hopping. *J. Chem. Phys.* **2010**, *133*, 134111.

(60) ChemShell3.4, a Computational Chemistry Shell; see www.chemshell.org.

(61) Metz, S.; Kästner, J.; Sokol, A.; Keal, T.; Sherwood, P. ChemShell—a modular software package for QM/MM simulations. *WIREs Comput. Mol. Sci.* **2014**, *4*, 101−110.

(62) Ziółek, M.; Kubicki, J.; Maciejewski, A.; Naskręcki, R.; Grabowska, A. Excited state proton transfer and photochromism of an aromatic Schiff base. Pico-and femtosecond kinetics of the salicylidene phenylenediamine. *Chem. Phys. Lett.* **2003**, *369*, 80−89.

Supporting Information: Photoswitching of Salicylidene Methylamine: a Theoretical Photodynamics Study

Lasse Spörkel,[†] Joanna Jankowska,[‡] and Walter Thiel[*,†]

Max-Planck-Institut für Kohlenforschung, Kaiser-Wilhelm-Platz 1, 45470 Mülheim an der Ruhr, Germany, and College of Inter-Faculty Individual Studies in Mathematics and Natural Sciences, University of Warsaw, Zwirki i Wigury 93, 02-089 Warsaw, Poland, Faculty of Chemistry, University of Warsaw, 1 Pasteura St., 02-093 Warsaw, Poland

E-mail: thiel@kofo.mpg.de

---

[*]To whom correspondence should be addressed

[†]Max-Planck-Institut für Kohlenforschung, Kaiser-Wilhelm-Platz 1, 45470 Mülheim an der Ruhr, Germany

[‡]College of Inter-Faculty Individual Studies in Mathematics and Natural Sciences, University of Warsaw, Zwirki i Wigury 93, 02-089 Warsaw, Poland, Faculty of Chemistry, University of Warsaw, 1 Pasteura St., 02-093 Warsaw, Poland

1

Table of Contents

- OM2/MRCI Active Space

- Ab Initio Relative Energies

- SMA Photochemical Classes Definition

- Cartesian Coordinates of OM2/MRCI Structures

- Cartesian Coordinates of Ab Initio Structures

2

OM2/MRCI Active Space

The active space in the MRCI calculations included 10 electrons in 10 orbitals. Figure 1 shows the active orbitals for the most stable ground-state conformer of salicylidene methylamine (α isomer).

In the closed-shell wavefunction of the planar ground state, the set of active orbitals consists of the 5 highest occupied orbitals and the 5 lowest unoccupied orbitals. This includes orbitals of π and σ type, so that different types of excitations can be taken into account.

Ab Initio Relative Energies

Ab initio results from previous work are shown here for comparison.[1] Structures were optimized with MP2/cc-pVDZ for ground states and CC2/cc-pVDZ for excited states. Conical intersections were optimized with the CASSCF(6,6)/cc-pVDZ method. Vertical excitations were computed using CC2/aug-cc-pVTZ.

Table 1: Ab Initio Values for Relative Energies, Vertical Excitation Energies, and Important Geometrical Parameters for the Relevant Isomers and Conical Intersections of SMA

	S_0 (kcal/mol)	S_1 (kcal/mol)	Vert. Exc. (eV)	OH (Å)	NH (Å)	CC (°)	CN (°)
α (S_0)	0.0	94.8	4.1	0.997	1.719	0.0	180.0
β (S_0)	Relaxation to α (S_0)						
γ (S_0)	22.1	68.5	2.9	4.743	1.016	179.6	177.9
δ (S_0)	13.8	105.5	4.6	0.971	2.474	-57.0	-4.7
α (S_1)	Relaxation to β (S_1)						
β (S_1)	34.7	65.1	1.7	1.870	1.028	0.0	-150.7
γ (S_1)	50.5	64.6	1.1	4.669	1.021	180.0	168.2
δ (S_1)	Relaxation to CI2						
CI1	–	–	0.0	3.127	1.025	87.7	-168.5
CI2	–	–	0.0	0.948	2.091	-3.5	-90.3

3

HOMO - 4   HOMO - 3

HOMO - 2   HOMO - 1

HOMO   LUMO

LUMO + 1   LUMO + 2
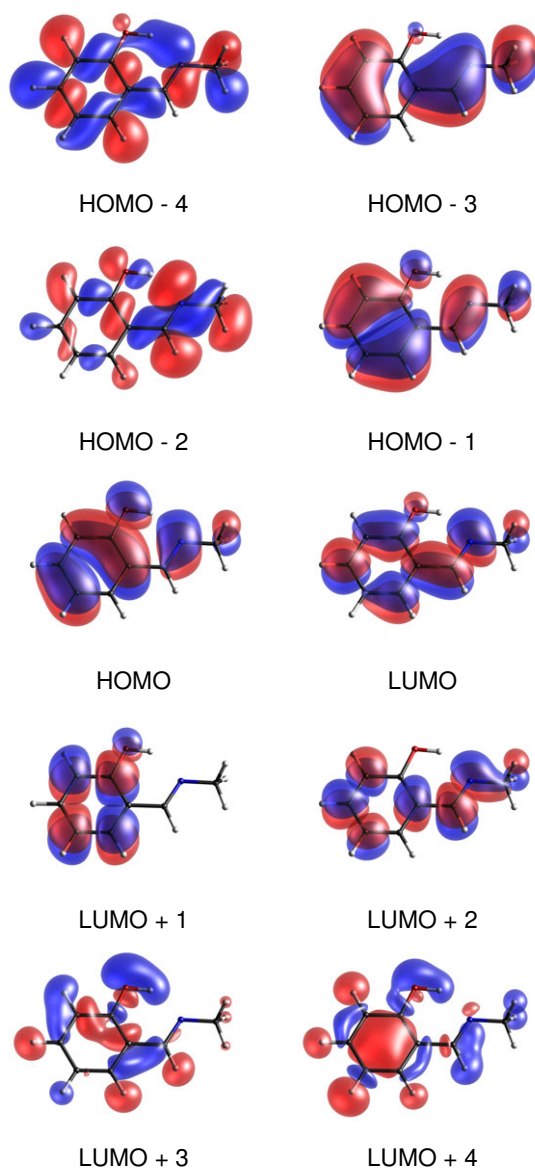
LUMO + 3   LUMO + 4

Figure 1: The active space (10e,10o) of salicylidene methylamine (cis-enol form) used in the OM2/MRCI calculations. Orbitals HOMO-3, HOMO-1, HOMO, LUMO, LUMO+1, LUMO+2 are of π type. See text for simulation details.

4

SMA Photochemical Classes Definition

	OH (Å)	|CC| dihedral angle (°)	|CN| dihedral angle (°)
α	< NH	any value	> 90
β	> NH	< 90	any value
γ	> NH	> 90	any value
δ	< NH	any value	< 90

5

References

(1) Jankowska, J.; Rode, M. F.; Sadlej, J.; Sobolewski, A. L. *ChemPhysChem* **2012**, *13*, 4287–4294.

10

D. Adaptive Time Steps in Trajectory Surface Hopping Simulations

Lasse Spörkel and Walter Thiel

I planned and implemented the adaptive time step. I carried out all example calculations and wrote most parts of the manuscript. I created all included figures.

Adaptive time steps in trajectory surface hopping simulations

Lasse Spörkel[a)] and Walter Thiel[b)]
Max-Planck-Institut für Kohlenforschung, Kaiser-Wilhelm-Platz 1, 45470 Mülheim an der Ruhr, Germany

Trajectory surface hopping (TSH) simulations are often performed in combination with active-space multi-reference configuration interaction (MRCI) treatments. Technical problems may arise in such simulations if active and inactive orbitals strongly mix and switch in some particular regions. We propose to use adaptive time steps when such regions are encountered in TSH simulations. For this purpose, we present a computational protocol that is easy to implement and increases the computational effort only in the critical regions. We test this procedure through TSH simulations of a GFP chromophore model (OHBI) and a light-driven rotary molecular motor (F-NAIBP) on semiempirical MRCI potential energy surfaces, by comparing the results from simulations with adaptive time steps to analogous ones with constant time steps. For both test molecules, the number of successful trajectories without technical failures rises significantly, from 53% to 95% for OHBI and from 25% to 96% for F-NAIBP. The computed excited-state lifetime remains essentially the same for OHBI and increases somewhat for F-NAIBP, and there is almost no change in the computed quantum efficiency for internal rotation in F-NAIBP. We recommend the general use of adaptive time steps in TSH simulations with active-space CI methods because this will help to avoid technical problems, increase the overall efficiency and robustness of the simulations, and allow for a more complete sampling. © 2016 Author(s). All article content, except where otherwise noted, is licensed under a Creative Commons Attribution (CC BY) license (*http://creativecommons.org/licenses/by/4.0/*). [http://dx.doi.org/10.1063/1.4948956]

I. INTRODUCTION

Excited-state molecular dynamics (MD) simulations generally involve more than one potential energy surface (PES), since they need to describe both the relaxation and rearrangement processes in the initially populated state as well as the subsequent decay to the electronic ground state, possibly via other excited states. Of crucial importance for such internal conversions are conical intersections where different electronic states become degenerate (enabling radiationless transitions). To treat the dynamics around conical intersections properly, it is essential to apply an electronic structure method that offers a balanced description of all states involved. Configuration interaction (CI) methods and their multi-reference (MR) variants satisfy this condition, and they are thus in principle suitable for excited-state dynamics.

A number of methods are available to perform the actual excited-state dynamics simulations; one of the most popular is trajectory surface hopping (TSH).[1–4] In this approach, the molecule is always in one particular state, but stochastic hops between states are possible (for example, according to the fewest switches criterion).[5,6] The nuclear motion is propagated classically on the current PES, while the electronic properties are computed quantum-mechanically on-the-fly at every nuclear configuration. For the latter purpose, we use the semiempirical OM2/MRCI method[7–9] to determine the required electronic energies, gradients, and nonadiabatic couplings.[10] This method is fast and has been applied a

number of medium-sized organic chromophores[11] (for some recent examples, see Refs. 12–17).

In TSH simulations at the CI level, full CI calculations are normally not feasible for any but the very smallest systems, because the inclusion of all possible excitations will generally create a huge number of configurations that cannot be handled in practice. Therefore one usually defines an active space of orbitals and allows only certain types of excitations from pre-selected reference configurations. Only the configurations that can be created within these restrictions are included in the actual multi-reference CI expansion. For OM2/MRCI, we usually choose an active space of around 10 orbitals, with a few chemically relevant reference configurations, and include single and double (MRCISD) excitations.

In this article, we address technical problems that can arise in TSH simulations with OM2/MRCI and offer a simple solution, namely, the use of adaptive time steps. The key idea is to replace the current time step recursively by smaller steps until the problem disappears. The standard time step is recovered as soon as the problematic region is left. This correction procedure is local and easy to implement, and it increases the computational effort only when necessary.

II. METHODOLOGY

A. Conventional surface hopping

During TSH simulations with active-space CI treatments, the orbitals may change their character and order as a result of the movement of the atoms. This can cause problems in the

a)Electronic mail: spoerkel@kofo.mpg.de
b)Electronic mail: thiel@kofo.mpg.de

definition of the active space. For example, if the active space is comprised of the m highest occupied and n lowest unoccupied orbitals ($m + n$ frontier orbitals selected by energy), its composition will change when the order of orbitals is switched such that a previously inactive orbital becomes active (i.e., one of the $m + n$ frontier orbitals). In this case, there will be a sudden discontinuous change in the OM2/MRCISD energy and also in the gradient, which will corrupt the dynamics. It is thus essential to keep track of the orbitals along the trajectory, by computing their overlap between successive steps, and to retain the qualitative composition of the active space (by keeping the "tracked" orbitals even if they move out of the frontier range, while disregarding "intruder" orbitals). Evidently, this tracking procedure will become less effective and more error prone with increasing step size.

Similar remarks apply to another commonly employed definition of the active space, in terms of orbital character. For example, in TSH simulations of essentially planar molecules, it may be advantageous to use an active space comprised of all occupied and unoccupied π orbitals. This will generally be a "sparse" active space, with inactive σ orbitals lying energetically between the active π orbitals. In this case, a change in the order of σ and π orbitals during TSH dynamics is more likely than in the case of an active space composed of frontier orbitals only, simply because there are more opportunities for orbital switches. In this situation, tracking the orbitals along the TSH trajectory is obviously even more essential to ensure that the composition of the active space is retained during the simulation.

A related problem concerns the calculation of the gradient during TSH simulations using active-space CI methods. For example, if an active orbital and an inactive occupied orbital become close in energy, they will start mixing so that the character of the corresponding active orbital starts to change. This will affect the interactions with the correlating single and double excitations in the CISD treatment and lead to inconsistent energies and gradients, basically because the orbital and CI coefficients are optimized separately rather than simultaneously. In OM2/MRCISD TSH simulations, the occurrence of such unphysical energies and gradients can indeed be observed and traced back to strong orbital rotations of the kind described. One obvious remedy would seem to be an extension of the active space locally at and around such problematic points. We have experimented with this option, which however only alleviates the problems without solving them.[18] Again, issues with detrimental orbital rotations will generally become more severe with increasing step size in the TSH simulations.

Unphysical local gradients caused by orbital rotations are usually much too high. The integration of the Newton equations (over large time steps) will then lead to high velocities, unrealistic geometries, and an unphysical increase of the kinetic energy. As a consequence, TSH simulations with such faulty gradients will tend to violate the conservation of total energy in the case of NVE ensembles.

In our previous work, we took several precautions against the problems outlined above and adopted the following standard procedure. The default time step for the propagation of the nuclei was chosen to be rather small (0.1 fs). Orbital

tracking was always activated with the default requirement that active orbitals had to retain their character to 70% in two consecutive steps, i.e., the scalar product of the orbital coefficients had to exceed 0.7 in absolute value. At the post-processing stage, every finished trajectory was checked for sudden energy jumps; it was disregarded if the energy difference between any two steps was higher than a threshold (default 10 kcal/mol). Overall energy conservation was not checked in our default procedure.

B. Surface hopping with adaptive time steps

As described in Subsection II A, the TSH simulations may sometimes arrive at particularly problematic geometries where the mixing and switching between active and inactive orbitals causes abrupt changes in the computed electronic properties from one step to the next one. These problems are local in the sense that they normally appear only in certain small parts of configuration space. We propose a simple yet effective solution that is based on the key idea to reduce the integration time step in these areas (i.e., only when necessary). This is done by adopting the procedure specified in Figure 1.

This procedure ensures that the simulation always reaches time t_{k+1} irrespective of the number of substeps needed between t_k and t_{k+1}. The simulation results are saved to output files at the uniformly distributed sequence of times t_i for later analysis. Figure 2 illustrates how the chosen algorithm may overcome problems between steps t_1 and t_3.

In our procedure, the adaptive time step can be reduced iteratively up to a user-defined maximum number of iterations (l_{max}). In the lth iteration, it equals $\left(\frac{1}{2}\right)^l$ of the default time
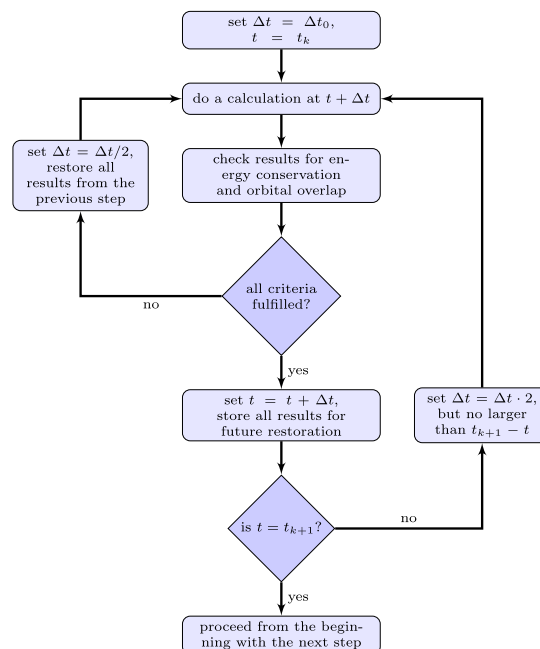

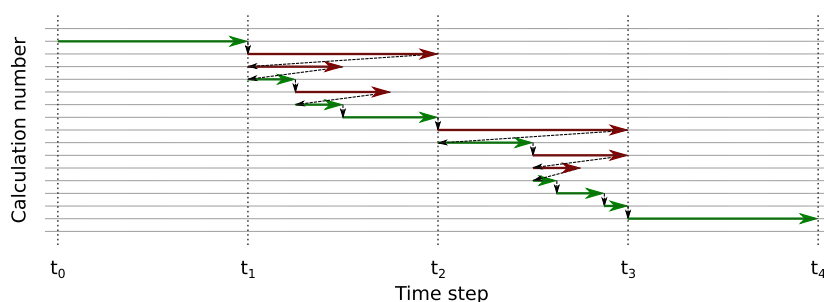FIG. 1. Flowchart of the adaptive time step algorithm.

109

FIG. 2. Symbolic example of a simulation with adaptive time steps. Green arrows symbolize successful calculations; red arrows indicate that one of the criteria is not fulfilled.

step Δt_0,

$$\Delta t_l = \Delta t_0 \cdot \left(\frac{1}{2}\right)^l. \tag{1}$$

The acceptance criteria and the maximum number of iterations are chosen by the user. For our test examples, we adopted rather stringent criteria requiring a relative total energy change of less than 0.01% and all orbital overlaps to be greater than 0.97 in absolute value. For the two selected test cases (see below), the first criterion requires the energy change to be smaller than 0.01 and 0.03 kcal/mol, respectively, in consecutive steps; we note that our code also supports direct input of the acceptable energy change (recommended option). Furthermore, we chose $l_{max} = 10$ so that the step can be reduced at most by a factor of 1024 (please note that SCF convergence and other thresholds may need to be tightened accordingly). If problems persist even after l_{max} tries, the whole simulation is stopped and discarded.

III. RESULTS

A. GFP chromophore model

As a representative first test case, we selected a GFP chromophore model, 4-(2-hydroxybenzylidene)-1H-imidazol-5(4H)-one (OHBI), which had previously been investigated in our group by OM2/MRCI nonadiabatics dynamics.[12] The orbital active space consisted of 12 electrons in 12 π orbitals and was thus of "sparse" character. One may therefore expect to encounter in this example many of the problems discussed above.

We exactly followed the previous computational protocol[12] but ran more trajectories for better statistical analysis. We started 1000 trajectories both for the old procedure and the new adaptive procedure. Some of the trajectories terminated during the simulation for technical reasons, for example, failure to achieve SCF convergence or unsuccessful orbital tracking. Others were rejected at the post-processing stage, because of unphysically high energy jumps in two consecutive steps (more than 10 kcal/mol, see above).

In Table I, we present for both procedures the numbers of started, successful (correct), and unsuccessful trajectories. In the latter case, we distinguish between post-processing rejection, SCF convergence failure, and other numerical

reasons (mainly orbital tracking). Obviously, the number of successful correct trajectories greatly increases from ca. 53% when using constant default time steps of 0.1 fs to ca. 95% with adaptive time steps. This is mainly because we ensure energy conservation between any two consecutive steps in the adaptive framework, which leads to much fewer rejections in the post-processing and also to a more stable simulation with less convergence and numerical problems (avoiding unphysically high gradients that generate unrealistic geometries in the next step). In our old procedure with constant time steps, the total energy may be much too high at the end of the simulation because errors between successive steps may accumulate; this may not be caught by our previous post-processing scripts that only check for an overly large energy difference between two steps (and not for overall energy conservation).

Figures 3 and 4 show the time evolution of the total energy for all trajectories and for the successful ones, with both procedures. Evidently, the total energy is not at all constant when using the constant default time step: even after the post-processing, the total energy increases significantly along most successful trajectories, on an average from 101.4 to 140.4 kcal/mol. When using the adaptive time step, only very few trajectories show a change in the total energy at all, and the average total energy remains essentially constant in the successful trajectories, with a small increase from 101.4 to 101.6 kcal/mol. In the old procedure, the observed increase in the total energy may cause artifacts in longer simulations, because the system may overcome barriers that are otherwise unsurmountable (leading to unrealistic photochemistry).

Figure 5 documents the actual number of steps taken along one particular (randomly chosen) trajectory in the adaptive scheme. For most of the time, the plot increases linearly

TABLE I. Number of different kinds of trajectories of the GFP chromophore for constant and adaptive time steps.

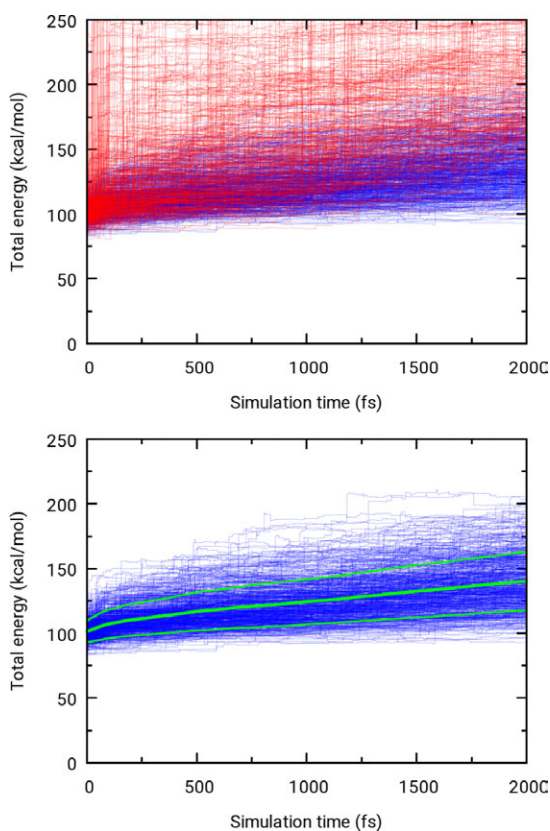|	Constant	Adaptive
Total	1000	1000
Successful	534	955
Rejected	350	5
No convergence	62	6
Numerical issues	54	34

FIG. 3. Time evolution of the total energy of the GFP chromophore with constant time step, for all trajectories (top) and for the successful trajectories (bottom). Shown in red: trajectories rejected in the post-processing. Green lines: average total energy and the associated standard deviation.
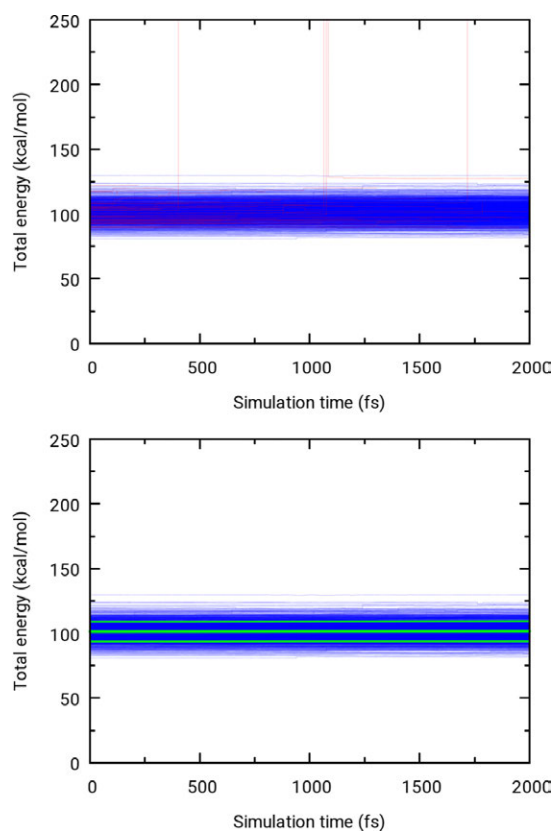

FIG. 4. Time evolution of the total energy of the GFP chromophore with adaptive time step, for all trajectories (top) and for the successful trajectories (bottom). Shown in red: trajectories rejected in the post-processing. Green lines: average total energy and the associated standard deviation.

indicating that the default time step of 0.1 fs is adequate. There are a few regions where the time step needs to be adapted because the acceptance criteria are not satisfied (see above). In these cases, the algorithm reduces the time step iteratively, additional substeps are taken, and the curve thus gets steeper. After leaving the problematic region, the time step adopts its default value again, and the curve becomes linear again. Obviously, in the chosen example, adaptive corrections are only needed on rare occasions, and the overall computation time increases only by about 10%.

Next we chose different time steps in the range of 0.05 fs up to 0.95 fs and ran simulations for 50 fs. The dependence of the number of adaptive corrections on the chosen time step is visualized in Figure 6. Shown are plots of the number of attempted steps (red and green arrows in Figure 2) and of accepted steps (green arrows in Figure 2) in the adaptive scheme; for comparison, we include a plot with the number of constant steps needed in the old procedure.

As expected, the adaptive algorithm does not need to intervene often for very small time steps (e.g., 0.05 fs) since the acceptance criteria are normally fulfilled. When the chosen time step becomes larger, the number of steps needed to reach 50 fs simulation time will generally tend to decrease.

However, for larger time steps, the acceptance criteria will be fulfilled less often, so that the curves for the numbers of attempted and constant steps start to diverge. The plot for the number of attempted steps shows a minimum in the region of $\Delta t = 0.2$ fs, where the time step is neither unnecessarily
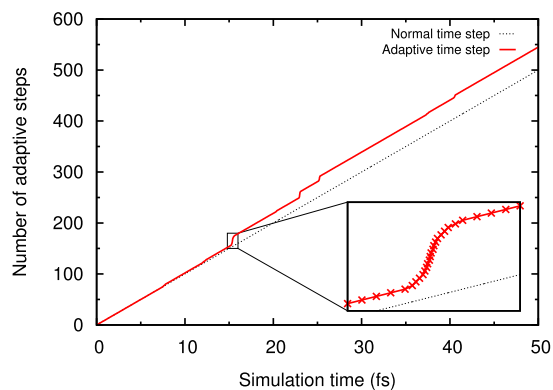

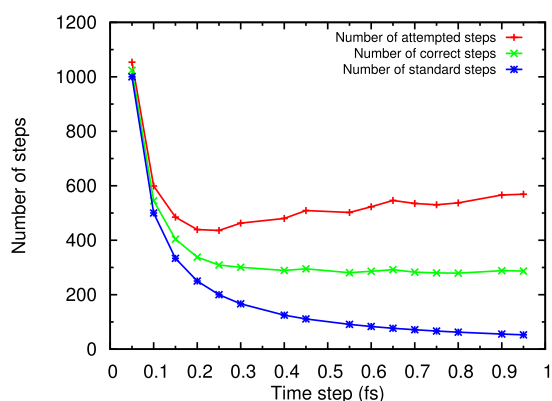FIG. 5. Number of steps in the adaptive scheme for one particular trajectory.

FIG. 6. Number of steps needed to reach 50 fs simulation time when using constant and adaptive steps.
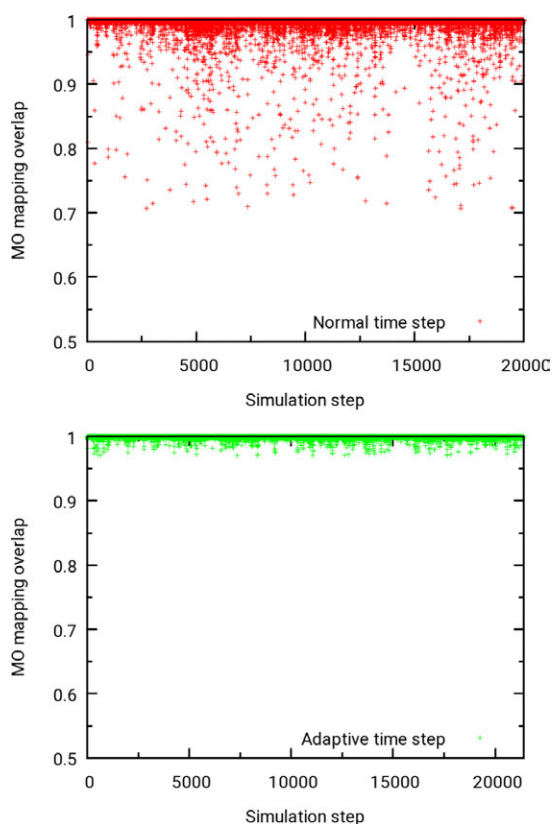

FIG. 7. Overlaps in the mapping of the active orbitals during the tracking procedure for one particular trajectory of the GFP chromophore, for the old (top) and the new (bottom) procedure.

small nor large enough to require many adaptive corrections. When the chosen time step gets very large (e.g., beyond $\Delta t = 0.3$ fs), the adaptive algorithm must reduce it very often so that the total number of attempted steps rises again. The data in Figure 6 indicate that the adaptive scheme is rather robust and that its computational demands do not depend much on the chosen step size. The adaptive procedure will always generate the steps that are required for getting stable results. The number of these steps seems to be minimal around $\Delta t = 0.2$ fs but increases only slightly for larger default steps. In this sense, the adaptive scheme resembles a black-box method since the choice of time step does not have much impact.

Another distinction between the old procedure and the new adaptive procedure concerns the orbital tracking.[18,19] The acceptance criterion for the mapping of the active orbitals has been tightened significantly: the absolute value of the scalar product of the orbital coefficients in two consecutive steps must exceed 0.70 in the old procedure compared with 0.97 in the new one. This is visualized for one particular (randomly chosen) trajectory in Figure 7, which contains these values for all accepted pairs of active orbitals. In the old procedure, there are quite a few smaller overlaps (in the range 0.7–0.9) which may lead to problematic behavior, whereas all overlaps are enforced to be close to 1 (above 0.97) in the new procedure. The use of a less stringent overlap criterion in the old procedure was a compromise between ensuring some degree of overlap and avoiding to have a huge percentage of failed trajectories. In the new procedure, a tight criterion can be imposed because the time step can be adapted sufficiently to satisfy the criterion also in problematic cases.

Finally, we address an obvious question: how much are our previous published results on the GFP chromophore[12] affected when using the new adaptive procedure? In our previous work, the decay from the S_1 to the S_0 state of the chromophore was studied by non-adiabatic dynamics simulations at the OM2/MRCI level, which yield the time evolution of the average state populations (and hence the lifetime of the excited state). The time evolutions are plotted

in Figure 8 as obtained from the old procedure and the new adaptive procedure.

It is reassuring that these plots are very similar and that the deactivation times are essentially identical (311 and 319 fs,
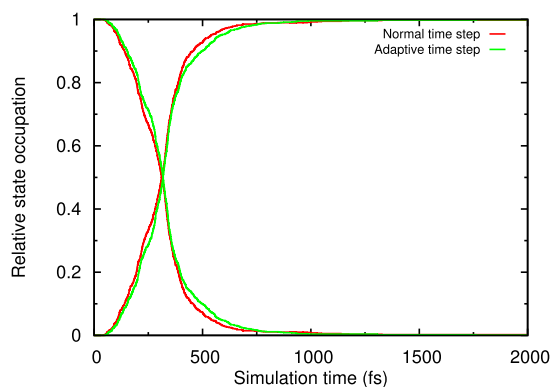

FIG. 8. Time evolution of the average state occupations of the GFP chromophore obtained from all successful trajectories using constant and adaptive time steps.

respectively, at the crossing points). While being technically superior, the new adaptive procedure thus gives essentially the same results as the old one in this particular test case. This may be related to the fact that the S_1/S_0 deactivation of the GFP chromophore is an ultrafast process that is finished very early, before technical errors may accumulate.

B. Light-driven molecular motor

As second example, we consider a molecular motor studied recently in our group,[17] namely, a fluorinated N-alkylated indanylidene benzopyrrole (NAIBP), 3-[(2S)-2-fluoro-2-methyl-1-indanylidene]-1-methyl-2-methylindole (F-NAIBP), which was the technically most demanding system investigated by us so far, with the highest percentage of unsuccessful trajectories. The purpose of our previous work was the computational design of light-driven rotary molecular motors with improved quantum efficiency.[17] OM2/MRCI TSH simulations gave quantum efficiencies of up to 47% for the four F-NAIBP conformers, roughly twice as high as those measured experimentally for the analogous all-hydrocarbon motors.[17] These results were based on more than 300 successful trajectories for each F-NAIBP conformer.[17]

In our previous report, we did not elaborate on the technical difficulties encountered in these OM2/MRCI TSH simulations. F-NAIBP has 41 atoms and is thus a rather large molecule, almost twice the size of the GFP model chromophore OHBI (22 atoms). The spectrum of valence orbital energies is therefore quite dense for F-NAIBP, significantly more so than in the case of OHBI, and the problems associated with the mixing and switching between active and inactive orbitals are more severe. In an attempt to cope with this problem, we chose a small time step of 0.05 fs (half the default value) in our previous work,[17] but still only a small fraction of trajectories finished successfully and fulfilled the continuity criteria. Hence we had to rerun most of the trajectories several times (with different random starting velocities) until they finished properly. TSH simulations with a constant time step are obviously very inefficient for F-NAIBP, which thus offers a stringent test for the proposed procedure with an adaptive time step. We chose the EP conformer[17] of F-NAIBP as the starting point for the present simulations.

For direct comparisons between the procedures with constant and adaptive time steps, we ran two sets of excited-state dynamics with 600 trajectories each. In contrast to our previous work, we included all orbitals with π character in the active space of the MRCI treatment (8 electrons in 9 orbitals); previously we had left out one virtual orbital with π character that caused particularly severe problems in the TSH simulations.[17] The default time step was presently chosen to be 0.1 fs. In the runs with constant time steps, trajectories were discarded if the overlap in the orbital mapping was below 0.70 or if there was an energy change of more than 10 kcal/mol between successive steps. When using adaptive time steps, the overlap in the orbital mapping was required to exceed 0.97 and the maximum relative change of total energy had to remain below 0.01% between successive steps.

The numbers of started and finished trajectories are listed in Table II. In the simulations with constant time steps, only

TABLE II. Number of different kinds of trajectories for F-NAIBP when using constant and adaptive time steps.

	Constant	Adaptive
Total	600	600
Successful	152	574
Rejected	49	0
No convergence	3	19
Numerical issues	396	7

ca. 25% of the trajectories finish successfully and survive all checks. The number of successful trajectories is greatly increased to ca. 96% by the use of adaptive time steps; in this case, not a single trajectory is rejected in the post-processing checks on energy conservation.

Figures 9 and 10 show the total energies along all trajectories for F-NAIBP. The plots are similar to those for OHBI (Figures 3 and 4), although after post-processing the results for constant and adaptive time steps differ less than those in the case of OHBI. The average total energy increases from 277.9 to 283.1 kcal/mol with constant time steps and
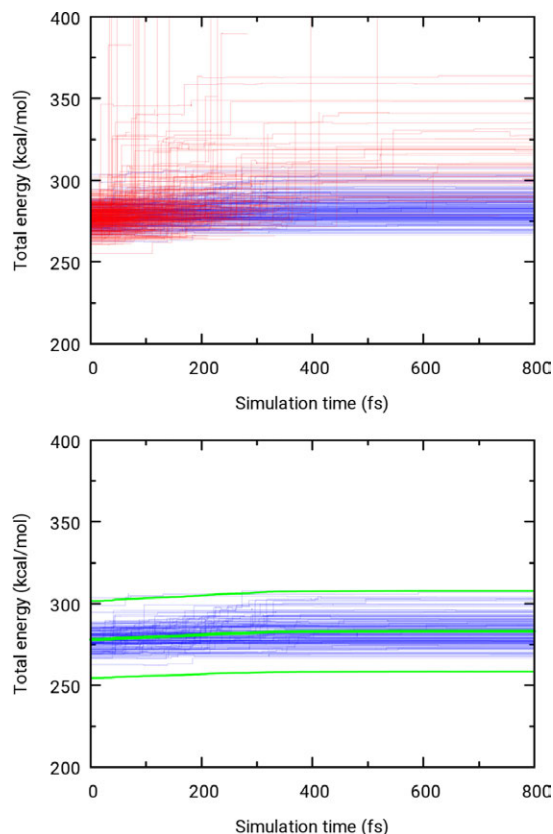

FIG. 9. Time evolution of the total energy of F-NAIBP with constant time step, for all trajectories (top) and for the successful trajectories (bottom). Shown in red: trajectories rejected in the post-processing. Green lines: average total energy and the associated standard deviation.

113

FIG. 11. Time evolution of the average state occupations of F-NAIBP obtained from all successful trajectories using constant and adaptive time steps.
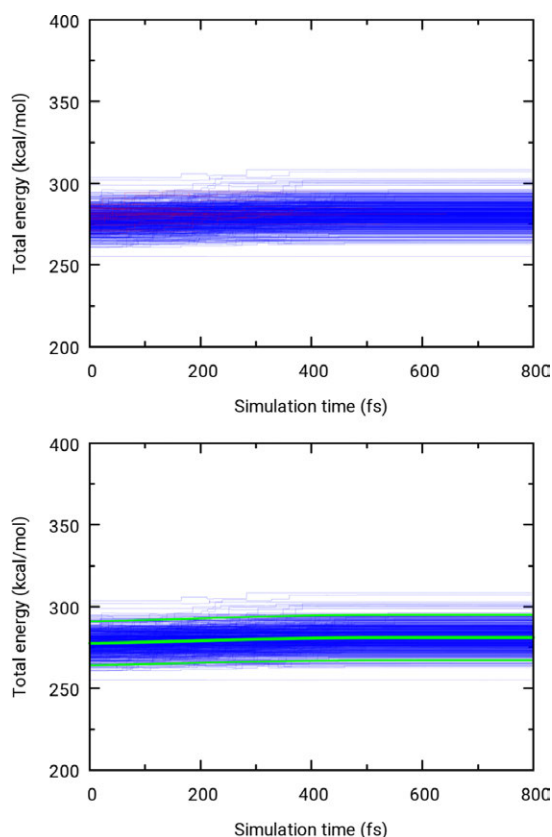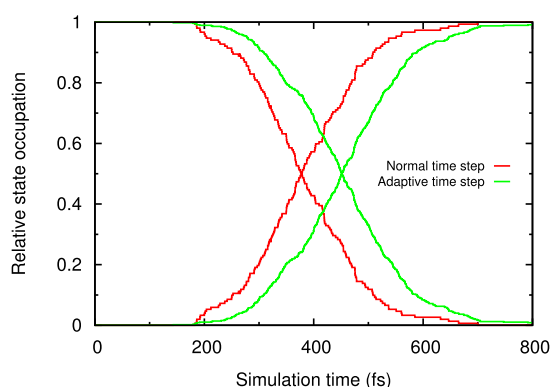
FIG. 10. Time evolution of the total energy of F-NAIBP with adaptive time step, for all trajectories (top) and for the successful trajectories (bottom). Shown in red: trajectories rejected in the post-processing. Green lines: average total energy and the associated standard deviation.

time steps, respectively. These are close to each other and to the value published previously for the EP conformer of F-NAIBP (0.47).[17] The technical improvements through the use of adaptive time steps thus lead to a notable increase in the lifetime of the excited state (by 19%) but have only a minor effect on the predicted quantum efficiency, thus corroborating the main qualitative conclusions from our previous study.[17]

from 277.6 to 281.1 kcal/mol with adaptive time steps. Unlike OHBI, the total energy of F-NAIBP is thus not fully conserved even when using adaptive time steps, indicating the limitations of this procedure in difficult cases.

The average state occupations of F-NAIBP are shown in Figure 11. In contrast to the case of OHBI, there is a distinct difference in the computed lifetimes of the excited state: half of the trajectories have decayed to the ground state after 379 (452) fs for constant (adaptive) time steps. Apparently the use of adaptive time steps may allow trajectories to stay longer in the excited state by surviving visits to problematic regions, where trajectories are discarded in runs with constant time steps.

The central target property of our previous study[17] was the quantum efficiency of the photoinduced rotation of molecular motors, which is defined in terms of the dihedral angle of the central C=C bond at the end of each trajectory (180° at the outset). A final dihedral angle of less than 90° is taken to indicate a successful rotation. The number of such "rotated" trajectories divided by the total number of trajectories gives the quantum efficiency. The present simulations yield values of 0.45 and 0.43 for trajectories with constant and adaptive

IV. DISCUSSION

In the proposed approach, adaptive time steps are introduced to overcome technical problems during the required on-the-fly electronic structure calculations, which are caused by the use of an active-space MRCI treatment that is, in principle, well suited for describing excited states and conical intersections. Of course, there are other quantum-chemical methods that do not suffer from such technical problems but face other limitations. One such example is linear-response density functional theory, which is widely used for excited-state dynamics[1–4] but does not give the correct topology for conical intersections between the electronic ground state and the first singlet excited state.[20] Because of their general applicability and solid theoretical foundation, MRCI methods are expected to remain a preferred choice in excited-state dynamics simulations, and technical advances such as the proposed adaptive time step protocol should therefore be of considerable practical value.

We are not aware of any other work in the TSH field that utilizes adaptive time steps for the purposes addressed in this article. Of course, adaptive protocols have proven to be valuable for other purposes and tasks in TSH simulations. For example, adaptive integration schemes have been developed for more accurate calculations of hopping probabilities,[21] and the fewest-switches algorithm has been modified by incorporating quantum uncertainty into the hopping times of classically forbidden hops.[22] Recently, the occurrence of trivial crossings between noninteracting or weakly interacting states (e.g., in extended systems) has been recognized as a particular challenge for standard TSH simulations.[23,24] In such cases, the nonadiabatic couplings peak sharply (being strongly

localized near the exact crossing points) so that conventional fewest-switches TSH simulations require very small time steps and thus become very costly; in the noninteracting limit, the couplings become a delta function, and numerical simulations with a finite time step are no longer feasible.[25] Hence, these problems cannot be resolved by straightforward adaptation of the time steps, but need to be tackled by different strategies, including self-consistent fewest-switches surface hopping,[24] flexible surface hopping,[26] global flux surface hopping,[27] and local diabatization.[28,29] While these novel schemes aim at improvements of the basic TSH formalism, our proposed adaptive time step protocol retains the standard TSH framework and aims at making TSH simulations with active-space MRCI treatments more robust and reliable.

V. CONCLUSIONS

The use of an adaptive time step can greatly improve the stability and accuracy of TSH simulations on potential surfaces computed with active-space CI methods. Problems arising from the mixing and switching between active and inactive orbitals can be controlled by sufficient reduction of the time step in such regions. The proposed algorithm supports energy conservation and successful orbital tracking also in problematic regions. It does not change the underlying methodology and increases the computational effort only slightly since smaller time steps are only applied locally when necessary. It is easily implemented and does not cause any changes in the post-processing analysis. The adaptive algorithm greatly lowers the number of trajectories that have to be rejected during post-processing.

Test calculations on a GFP chromophore model show that the adaptive scheme produces TSH trajectories with a much higher success rate (95%) than the previously used scheme (53%). Moreover, it ensures that the trajectories are technically sound in terms of energy conservation and orbital tracking. In the case of this GFP chromophore, these technical advances have no impact on the results of the TSH simulations: the previous protocol with constant time steps and the adaptive scheme yields essentially the same results for the time evolution of the average state occupations and for the deactivation times.

TSH simulations of the molecular motor F-NAIBP show an even bigger improvement in the success rate, which could be increased from 25% to 96%. In this case, trajectories that are kept alive through the use of adaptive time steps may apparently sample the excited-state PES for a longer time, which results in an average deactivation time that is about

70 fs larger than that obtained with constant time steps. On the other hand, the quantum efficiency of the photoinduced internal rotation of the molecular motor is hardly affected.

In summary, the use of adaptive time steps in TSH simulations with active-space CI methods is strongly recommended, because it helps to resolve technical problems, increases the efficiency and robustness of the simulations, and allows a more complete and realistic sampling of the PES.

[1]M. Barbatti, Wiley Interdiscip. Rev.: Comput. Mol. Sci. **1**, 620 (2011).
[2]B. Curchod, U. Rothlisberger, and I. Tavernelli, ChemPhysChem **14**, 1314 (2013).
[3]E. Tapavicza, G. L. Bellchambers, J. Vincent, and F. Furche, Phys. Chem. Chem. Phys. **15**, 18336 (2013).
[4]M. Barbatti and R. Crespo-Otero, Top. Curr. Chem. **368**, 415 (2016).
[5]J. Tully, J. Chem. Phys. **93**, 1061 (1990).
[6]S. Hammes-Schiffer and J. Tully, J. Chem. Phys. **101**, 4657 (1994).
[7]P. Dral, X. Wu, L. Spörkel, A. Koslowski, W. Weber, R. Steiger, M. Scholten, and W. Thiel, J. Chem. Theory Comput. **12**, 1082 (2016).
[8]P. Dral, X. Wu, L. Spörkel, A. Koslowski, and W. Thiel, J. Chem. Theory Comput. **12**, 1097 (2016).
[9]A. Koslowski, M. Beck, and W. Thiel, J. Comput. Chem. **24**, 714 (2003).
[10]S. Patchkovskii, A. Koslowski, and W. Thiel, Theor. Chem. Acc. **114**, 84 (2005).
[11]W. Thiel, Wiley Interdiscip. Rev.: Comput. Mol. Sci. **4**, 145 (2014).
[12]G. Cui, Z. Lan, and W. Thiel, J. Am. Chem. Soc. **134**, 1662 (2012).
[13]G. Cui and W. Thiel, Angew. Chem., Int. Ed. **52**, 433 (2013).
[14]L. Spörkel, G. Cui, and W. Thiel, J. Phys. Chem. A **117**, 4574 (2013).
[15]L. Spörkel, G. Cui, A. Koslowski, and W. Thiel, J. Phys. Chem. A **118**, 152 (2014).
[16]L. Spörkel, J. Jankowska, and W. Thiel, J. Phys. Chem. B **119**, 2702 (2014).
[17]A. Nikiforov, J. A. Gamez, W. Thiel, and M. Filatov, J. Phys. Chem. Lett. **7**, 105 (2016).
[18]T. Keal, M. Wanko, and W. Thiel, Theor. Chem. Acc. **123**, 145 (2009).
[19]E. Fabiano, T. Keal, and W. Thiel, Chem. Phys. **349**, 334 (2008).
[20]B. G. Levine, C. Ko, J. Quenneville, and T. J. Martinez, Mol. Phys. **104**, 1039 (2006).
[21]M. D. Hack, A. W. Jasper, Y. L. Volobuev, D. W. Schwenke, and D. G. Truhlar, J. Phys. Chem. A **103**, 6309 (1999).
[22]A. W. Jasper, S. N. Stechmann, and D. G. Truhlar, J. Chem. Phys. **116**, 5424 (2002).
[23]S. Fernandez-Alberti, A. E. Roitberg, T. Nelson, and S. Tretiak, J. Chem. Phys. **137**, 014512 (2012).
[24]L. Wang and O. V. Prezhdo, J. Phys. Chem. Lett. **5**, 713 (2014).
[25]L. Wang, R. Long, and O. V. Prezhdo, Annu. Rev. Phys. Chem. **66**, 549 (2015).
[26]L. Wang and D. Beljonne, J. Phys. Chem. Lett. **4**, 1888 (2013).
[27]L. Wang, D. Trivedi, and O. V. Prezhdo, J. Chem. Theory Comput. **10**, 3598 (2014).
[28]G. Granucci, M. Persico, and A. Toniolo, J. Chem. Phys. **114**, 10608 (2001).
[29]F. Plasser, G. Granucci, J. Pittner, M. Barbatti, M. Persico, and H. Lischka, J. Chem. Phys. **137**, 22A514 (2012).